Development and Biomechanical Analysis toward a Mechanically Passive Wearable Shoulder Exoskeleton

A Dissertation Presented for the

Doctor of Philosophy

Degree

The University of Tennessee, Knoxville

Seyyed Morteza Asgari

December 2023

This dissertation is dedicated to my wife, parents, family, friends, and research team.

ABSTRACT

Shoulder disability is a prevalent health issue associated with various orthopedic and neurological conditions, like rotator cuff tear and peripheral nerve injury. Many individuals with shoulder disability experience mild to moderate impairment and struggle with elevating the shoulder or holding the arm against gravity. To address this clinical need, I have focused my research on developing wearable passive exoskeletons that provide continuous at-home movement assistance. Through a combination of experiments and computational tools, I aim to optimize the design of these exoskeletons.

In pursuit of this goal, I have designed, fabricated, and preliminarily evaluated a wearable, passive, cam-driven shoulder exoskeleton prototype. Notably, the exoskeleton features a modular spring-cam-wheel module, allowing customizable assistive force to compensate for different proportions of the shoulder elevation moment due to gravity. The results of my research demonstrated that this exoskeleton, providing modest one-fourth gravity moment compensation at the shoulder, can effectively reduce muscle activity, including deltoid and rotator cuff muscles.

One crucial aspect of passive shoulder exoskeleton design is determining the optimal anti-gravity assistance level. I have addressed this challenge using computational tools and found that an assistance level within the range of 20-30% of the maximum gravity torque at the shoulder joint yields superior performance for specific shoulder functional tasks.

When facing a new task dynamic, such as wearing a passive shoulder exoskeleton, the human neuro-musculoskeletal system adapts and modulates limb impedance at the end-limb (i.e., hand) to enhance task stability. I have presented development and validation of a realistic neuromusculoskeletal model of the upper limb that can predict stiffness modulation and motor adaptation in response to newly introduced environments and force fields. Future studies will explore the model's applicability in predicting stiffness modulation for 3D movements in novel environments, such as passive assistive devices' force fields.

TABLE OF CONTENTS

LIST OF TABLES

LIST OF FIGURES

CHAPTER 1 : INTRODUCTION

Background

The human shoulder is the most intricate and flexible joint featuring four bony joints: the sternoclavicular, glenohumeral (GH), scapulothoracic, and acromioclavicular joints. The normal kinematic interactions between these joints provide the shoulder with a wide range of mobility. Among these joints, the GH joint has the largest range of motion functioning as a synovial "ball and socket" joint that connects the glenoid socket to the humeral head. Although the glenoid socket only partially encapsulates the humeral head, rendering the GH joint structurally unstable, its stability is bolstered by the active tissues of the rotator cuff and surrounding muscles [1].

Shoulder disability is a common health problem associated with upper extremity impairment and socioeconomic cost for the individuals [2-4], private industries, and governments [5]. The majority of the shoulder impairments are linked to rotator cuff tears [6], aging [7], occupational injuries [8], stroke [9], and other medical conditions [10, 11]. Around one-third of visits to primary care offices related to shoulder issues (approximately 33.2%) in the United States are connected to shoulder injuries [12]. These cases often require the use of diagnostic imaging methods and physiotherapy sessions [12]. Among the new episodes of shoulder disability in primary care, about 50% shows chronicity after a 12-month follow-up [14]. Shoulder injures also leads the highest days of work absence, 23 days, for labors in occupational settings [5].

Shoulder impairments are associated with shoulder weakness [13], limited range of motion [14], and inability to perform activities of daily living [15]. Patients often present with large deficits in strength and range of motion in the direction of shoulder elevation, which involves moving or holding the arm against gravity [16]. These gravity-related functional deficits occur for two reasons. First, gravity is the dominant contributor to shoulder loading during many activities of daily living [17]; this is not surprising since the shoulder is the most proximal joint of the upper extremity and, thus, must support the upper extremity's entire weight and any object held in the hand. Second, shoulder disabilities mostly involve tears and strain for those muscles who have major contributors to the shoulder elevation [18]. Such functional deficit diminishes people's quality of life by depriving them of their ability to perform their activities of daily living (ADL).

Motivation

Given that gravity is a major contributor to functional deficits and shoulder loads, there is a need for new interventions that can provide patients with portable, continuous, at-home gravity compensation at the shoulder. Pursuant to the need for such interventions, engineers have developed assistive wearable devices such as exoskeletons to augment the strength and enhance the motor function of the shoulder [19-24]. Exoskeletons are mainly external mechanical structures that generate forces either actively (e.g., using electric motors) [20, 25] or passively (e.g., using elastic springs) [26-28]. Passive shoulder exoskeletons are attractive because they are potentially more cost effective, lightweight, comfortable, and reliable than active, motorized exoskeletons. Continuous, portable gravity compensation would beneficially reduce the forces that muscles crossing the shoulder need to exert during movement, which could (1) improve movement efficiency and reduce fatigue, (2) enhance effective strength and range of motion, and (3) reduce musculotendon tissue loads and the associated risk of tissue injury or re-injury. Portable exoskeletons have strong potential to reduce healthcare costs when used for home-based rehabilitation, which is more convenient and cost-effective than in-clinic rehabilitation [29]. Portable exoskeletons could potentially provide more effective rehabilitation since the exoskeleton “therapy” can be applied more frequently and for longer duration. When used long-term for people with chronic disability, portable exoskeletons can help people maintain a higher level of independence for a longer period of time, reducing costs associated with a loss of independence. By enhancing functional ability, portable exoskeletons could help people achieve a more active lifestyle and overcome lifestyle-related disorders such as obesity, diabetes, and heart disease.

Commercially available passive exoskeletons and devices fall short in providing continuous, at-home assistance for people with shoulder disability. Passive clinical devices, like SaeboMAS [30, 31], Wilmington Robotic Exoskeleton (WREX) [32], and T-WREX [27, 33], employ counterweights or spring mechanisms to counteract gravity and support arm movement for individuals with severe neurological shoulder disability. However, limitations such as fixed gravity compensation levels and the need for rigid mounting make them unsuitable for patients with greater mobility and mild to moderate shoulder disability. Furthermore, additional wearable passive shoulder exoskeletons in the market, such as (Ekso Bionics Holdings, Inc., Richmond, CA) and SuitX (US Bionics, Inc., Emeryville, CA), have been primarily designed for industrial use and heavy tasks. Thus, their applicability to daily living assistance for individuals with shoulder disabilities is limited as they are mainly specialized for static, quasi-static overhead tasks [34, 35].

For successful benchmarking and clinical translation of wearable passive shoulder exoskeletons, it is critical to perform comprehensive, detailed biomechanical evaluation that is specific to the abilities and typical tasks of the intended users. Exoskeletons that are not design-optimized or evaluated specifically for clinical populations could exacerbate musculoskeletal impairment and further degrade functional ability. Previous studies have primarily investigated biomechanics of gravity-compensating portable passive shoulder exoskeletons in the context of occupational settings for which they were designed [36-40]. While these studies have transformative implications for clinical contexts, it is crucial to further examine the impact of exoskeletons on neuromuscular biomechanics. This entails more comprehensive understanding of muscular responses, joint kinematics, as well as upper limb stability and stiffness.

Research objectives and approach

Our long-term goal is to develop wearable passive exoskeletons for continuous at-home movement assistance to improve the motor function of people with shoulder impairment. To inform the design of wearable passive shoulder exoskeletons, **<u>the overall objectives of this project</u>** are to <u>1) propose a novel wearable passive (i.e., spring powered) cam-based shoulder exoskeleton that can provide continuous at-home movement assistance and rehabilitation for people with shoulder disability; 2) analyze the effects of exoskeleton-applied forces on upper extremity biomechanics.</u> Our approach will involve designing and fabricating prototypes of the proposed shoulder exoskeleton and performing human subject testing. Additionally, we will use computational tools and approaches to simulate movements for different exoskeleton assistance conditions. We will pursue the following specific aims:

<u>Research Aim 1.1:</u> Design and fabricate a wearable passive (i.e., spring powered) cam-based shoulder exoskeleton (WPCSE) that is low-profile, lightweight, portable, and, thus, ideal for providing continuous, at-home assistance to patients with mild-to-moderate shoulder disability. The WPCSE is equipped with a soft, cable-driven mechanism wrapping around a cam-wheel gearing component to generate a bionic torque at the shoulder joint to counteract gravity.

Research Aim 1.2: Perform a pilot biomechanics study to preliminarily test the concept that the WPCSE could reduce the activity of muscles crossing the shoulder during select shoulder movements; secondarily, we will evaluate the effect of WPCSE on shoulder kinematics. The results will indicate the potential of the proposed WPCSE to assist shoulder movements.

Research Aim 2: Perform a simulation-based study to identify the optimal gravity compensation level for select functional shoulder movements based on shoulder muscle activity and joint stability. We expect that the findings of this aim will help us to find an optimal level of assistance for upper limb exoskeletons that best reduces the muscular effort across a wide range of shoulder movements without degrading shoulder joint and end-limb stability.

Research Aim 3: Develop a realistic neuromusculoskeletal model of force-impedance modulation for upper extremity movements that can help predict the end-limb stiffness modulation and motor adaptation to newly introduced force fields, such as a passive force from a wearable device. The proposed model will be used for investigating upper extremity movements in 3-dimensional space but will be validated in 2-dimensional space against previously published experimental results.

Chapter Summary

Chapter 2 of my work focuses on the creation of a novel wearable, passive, cam-based shoulder exoskeleton (WPCSE) designed to provide continuous assistance to patients with mild to moderate shoulder disability. The chapter comprises two sections, each discussing a different design iteration of the WPCSE. Section 2-1 covers the development process and qualitative assessment of the initial prototype. In section 2-2, I discuss the creation of a theoretical model and the design of a second prototype, along with the results of a benchtop experiment that validates the mechanical output of the WPCSE against the theoretical model. Additionally, I present the findings of a pilot biomechanics study, involving eight able-bodied subjects, which quantifies the exoskeleton's impact on muscle activity and shoulder kinematics during three shoulder movements.

In chapter 3, I focus on a simulation-based investigation to determine the optimal range of anti-gravity assistance for passive shoulder exoskeletons. The study utilized a task space framework for biomechanical simulations of various arm movements in OpenSim (Stanford, CA, USA), which mimicked functional tasks. These movements included shoulder elevation and lowering in frontal and scapular planes, as well as forward and lateral reaching. The chapter concludes by examining how different levels of anti-gravity assistance influence muscular response efficiency and joint and end-limb stability during the simulated upper extremity movements.

Chapter 4 presents the development of a realistic neuromusculoskeletal model for force-impedance modulation during upper limb movements. The chapter consists of two sections. In section 4-1, a computational approach is introduced, utilizing an upper limb neuromusculoskeletal-manipulandum model with realistic musculoskeletal geometry to estimate upper limb impedance parameters during posture maintenance. The computational impedance results are validated against published experimental data. In section 4-2, a model is proposed to predict dynamic stiffness modulation and motor adaptation to newly introduced environments and force fields, such as a passive shoulder wearable device. The theory of the model involves using the task space framework with a multi-priority control scheme to plan and execute muscle-driven, goal-oriented hand movements. The model is validated by comparing estimates of end-limb stiffness and modulation with experimental data for horizontal reaching movements under various force fields, including velocity-dependent and divergent force fields.

Finally, in chapter 8 I discuss the significance and contribution of this research as well as the future works.

CHAPTER 2 : DESIGN AND PROTOTYPING OF A WEARABLE PASSIVE CAM-BASED SHOULDER EXOSKELETON

This work was published in the 42nd Annual International Conference of the IEEE Engineering in Medicine & Biology Society and the Journal of Biomechanical Engineering.

1. M. Asgari, P. T. Hall, B. S. Moore and D. L. Crouch, "Wearable Shoulder Exoskeleton with Spring-Cam Mechanism for Customizable, Nonlinear Gravity Compensation," 2020 42nd Annual International Conference of the IEEE Engineering in Medicine & Biology Society (EMBC), 2020, pp. 4926-4929, doi: 10.1109/EMBC44109.2020.9175633.

2. Asgari, M., Phillips, E. A., Dalton, B. M., Rudl, J. L., and Crouch, D. L. (June 16, 2022). "Design and Preliminary Evaluation of a Wearable Passive Cam-Based Shoulder Exoskeleton." ASME. J Biomech. Eng. November 2022; 144(11): 111002. https://doi.org/10.1115/1.4054639

Section 2-1: Wearable Shoulder Exoskeleton with Spring-Cam Mechanism for Customizable, Nonlinear Gravity Compensation

Abstract

Wearable, mechanically passive (i.e., spring-powered) exoskeletons may be more practical and affordable than active, motorized exoskeletons for providing continuous, home-based, antigravity movement assistance for people with shoulder disability. However, the biomechanical moment due to gravity is a nonlinear function of shoulder elevation angle and, thus, challenging to counteract proportionally across the shoulder elevation range of motion with a spring alone. We designed, fabricated, and tested an integrated spring-cam-wheel system that can generate a nonlinear moment to proportionally compensate for the expected antigravity moment at the shoulder. We then incorporated the proposed system in a benchtop model and a novel wearable passive cable-driven exoskeleton that was intended to counteract half of the gravitational moment during shoulder elevation movements. The rotational moment measured from the benchtop model closely matched the theoretical moment during simulated positive shoulder elevation. However, a larger moment (up to 12.5% larger) was required during

simulated negative shoulder elevation to stretch the spring to its initial length due to spring hysteresis and friction losses. The wearable exoskeleton prototype was qualitatively tested for assisting shoulder elevation movements; we identified several aspects of the prototype design that need to be improved before further testing on human participants. In future studies, we will quantitatively evaluate human kinematics and neuromuscular coordination with the exoskeleton to determine its suitability for assisting patients with shoulder disability.

Introduction

Movement disability involving the shoulder is associated with several chronic health conditions, such as rotator cuff tears [41], peripheral nerve injury [10], and stroke [42]. Though patients may retain some shoulder strength and function, they are substantially diminished from that of the healthy shoulder [10]. Shoulder impairment may make it more difficult for patients to perform activities of daily living. For some conditions involving soft tissue injury, such as rotator cuff tear, biomechanical loads during tasks may lead to high re-injury rates. Devices that can provide continuous mechanical assistance to the shoulder are needed to help augment movement ability and decrease biomechanical loads in soft tissues in patients with shoulder disability.

Exoskeletons could meet the need for movement assistance to replace, assist, or rehabilitate function [25]. Exoskeletons are devices worn on and apply forces to the body using either active or passive systems. Active exoskeletons incorporate motorized actuators and are often intended for cases of severe impairment that require substantial movement assistance or neuro-rehabilitation [43]. However, due to their size, weight, cost, need for maintenance, and operation requirements, such active exoskeletons are usually constrained to clinics and labs, preventing continuous at-home assistance.

Compared to active exoskeletons, mechanically passive exoskeletons may be more suitable for home-based movement assistance. Passive exoskeletons incorporate elastic springs that store and return energy to supplement the users' muscles. Since passive exoskeletons do not have electromechanical hardware, they are potentially more affordable, lightweight, reliable, and compact. Current passive exoskeletons for the upper extremity mainly compensate for the weight of the upper extremity but do not generate movement on their own, making them potentially suitable for patients with mild to moderate disability. With weight compensation, patients could perform activities of daily living with less effort. Current passive assistive devices for the upper extremity and clinical applications include Armon [44], WREX [32], and Freebal [45].

The main drawback of passive exoskeletons is in generating complex force profiles. The shoulder elevation rotational moment due to gravity is a nonlinear function of the shoulder elevation angle (i.e., the angle between the arm and trunk). Thus, exoskeletons need to generate a similar nonlinear shoulder elevation moment to compensate for a constant proportion of the moment due to gravity. Furthermore, to support activities of daily living, exoskeletons should compensate for gravity over a wide range of shoulder elevation angles. Current gravity-compensating passive exoskeletons use mechanisms such as counterweights, springs [44], cam linkages, and rubber bands [32]. These mechanisms may balance the arm weight only for a relatively small range of shoulder elevation angles. Thus, to generate more complex, non-linear force profiles, engineers have used zero-free-length springs [46], compliant mechanisms [47], or a series of wrapping cams [48]. Among these methods, zero-free-length springs are expensive to fabricate, and the latter two require auxiliary rigid linkages to attach to the body, making them less wearable and portable.

The goal of this study was to design, fabricate, and experimentally evaluate a prototype of a wearable passive shoulder exoskeleton that could provide continuous, anti-gravity assistance to patients with shoulder disability. We first introduced an integrated spring-cam wheel mechanism that can provide gradually increasing, nonlinear mechanical assistance to compensate for the nonlinear shoulder elevation moment due to gravity. We validated the mathematical model of the spring-cam wheel mechanism using a benchtop prototype. Finally, we fabricated an exoskeleton prototype that incorporated the spring-cam wheel mechanism and qualitatively tested it on a human participant.

Mechanical Design

Design Concept

The proposed mechanically passive exoskeleton incorporates a preloaded elastic spring (Figure 2-1). The spring force is transmitted by a cable that crosses the superior aspect of the shoulder, generating a positive shoulder elevation moment to counteract

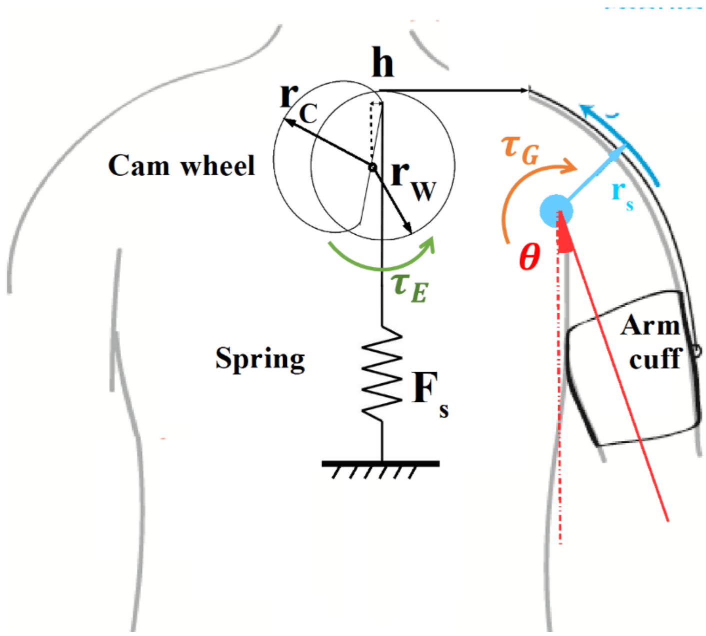

Figure 2-1. Diagram of shoulder exoskeleton concept (posterior view on right shoulder)

the negative shoulder elevation moment due to gravity. As the arm is elevated, the spring shortens, *decreasing* the spring tension force. However, the shoulder elevation moment due to gravity nonlinearly *increases* as the shoulder is elevated away from the body. To provide increasing assistance despite decreasing spring tension, we incorporated a cam wheel with a cable wrapped around the profile. The cam wheel acts as a variable gearing mechanism that outputs the desired increasing positive shoulder elevation moment with increasing shoulder elevation angle. The spring cable is attached to the variable radius cam, while the cable that outputs the force on the shoulder is attached to a constant-radius wheel that is concentric with and fixed to the cam. Since they are fixed to one another, the wheels share the same rotation angle (α) which is proportional to the shoulder elevation angle (θ) based on the ratio between the moment arms of the single radius wheel (r_w) and shoulder (r_s) as defined by:

$$\alpha = \frac{r_s}{r_w}\theta \tag{1}$$

The shoulder elevation moment due to gravity (M_G) was calculated at static shoulder elevation angles ranging from 0 to 90^{o} in the frontal plane with the elbow and hand extended:

$$M_G = (m_a d_a g + m_f d_f g + m_h d_h g)\sin(\theta) \tag{2}$$

where subscripts $a, f,$ and h represent the upper arm, forearm, and hand, respectively, m, d, and g represent mass, distance between the shoulder joint and the mass center, and acceleration due to gravity, respectively. We used limb anthropomorphic values of a 50th percentile adult male [49], though these could be changed to match the exoskeleton assistance to the subject's anthropometry. We computed the moment with the elbow extended M_G as:

$$M_G(\theta\ ) = 10.378\ \sin(\theta)\quad (\mathrm{Nm}) \tag{3}$$

Exoskeleton Mathematical Modeling and Optimization

We performed a constrained global numerical optimization to compute exoskeleton design parameters such that the exoskeleton's shoulder elevation moment (T_E) would compensate for half of M_G calculated in (3). This assistance level was chosen to avoid over-assisting when elbow and hand are not fully extended, though the exoskeleton could be tuned to compensate for any proportion of M_G. The first step in optimizing the design parameters was to identify the parameters on which T_E depends, assuming that the human-exoskeleton system is in static equilibrium:

$$T_E = \frac{r_s}{r_w} h(\alpha) F_s(\alpha) \tag{4}$$

In (4), $h(\alpha)$ is the moment arm of the variable-radius cam and $F_s(\alpha)$ is the force profile of the spring. Here we set $F_s(\alpha) = 45N$, which is the force generated by a commercially available constant-force spring that we estimated was sufficient for the physical exoskeleton prototype (SR48, KERN-LIEBERS Ltd. -Spiroflex). The moment arm of the shoulder r_s was estimated to be 6*cm* from a musculoskeletal model [50]. To optimize the parameters, we wrote a MATLAB script to execute a global optimization function (GlobalSearch) that minimized the residual sum of the squared error as the cost function (5):

$$\text{Cost Function } = ||T_E - 0.5M_G||^{\,2} \tag{5}$$

To determine the form of function $h(\alpha)$ (which affects the shape of the cam wheel) that minimized the optimization cost function, we ran the optimization routine for each of five standard functions: linear, quadratic, third order polynomial, power, and sinusoidal. All five of these were tested in the optimization script with parameters based on the functional coefficients, like A, B, and C in (6). The global optimization showed that a sinusoidal function permitted the best fit between T_E and M_G (Table 2-1). The sinusoid function used in the final optimization was defined as:

$$h(\alpha) = A\sin(B\alpha) + C \tag{6}$$

The output parameters used to calculate T_E are displayed in Table 2-2. Optimized Design parameters. Using the T_E output parameters, $h(\alpha)$ and r_w, the cam profile (Figure 2-2) was determined by performing a numerical integration based on the relationship between $h(\alpha)$, α, and the cable deflection $dx = h(\alpha)d\alpha$.

Table 2-1. Cost function values for $h(\alpha)$

Function Type	**Linear**	**Quad**	**Poly**	**Power**	**Sine**	**Linear**
Cost Function	19.646	0.394	0.566	5.367	0.000	19.646

Benchtop Setup

Based on the design parameters defined in the previous section, we developed a benchtop (aluminum board 45*cm*×60*cm*) prototype using off-the-shelf components to perform mechanical validation of our theoretical model (Figure 2-2). The benchtop prototype included the selected constant-force spring with an output force of 45 N. Three hundred points representing the cam profile (Figure 2-2, right panel) were imported into the Solidworks software to develop a computer-aided design model of the cam wheel (Figure 2-2, left panel), which was 3D printed ABS plastic. The constant-radius wheel was connected by a cable to a v-belt pulley (representing the shoulder) with a customized handhold that allowed us to manually rotate the pulley to simulate shoulder elevation movements. The radius of the pulley was 8*cm*, which is larger than the estimated moment arm of the shoulder in our model (Table 2-2) but sufficient for mechanical validation. The cam wheel was connected to the constant-force spring with a non-stretching nylon rope. Both the cam wheel and pulley were installed on the benchtop board with flange bearings. A micro S-type load cell (ATO-LC-S04, 50kg capacity, ATO, Diamond Bar, CA, USA) and an optical rotary encoder (LPD-3806-600bm-G5-24c, GTEACH, China) were used to measure the cable tension force and rotation angle of the pulley, respectively (Figure 2-3). A custom C++ script was written in Arduino software (version 1.8.5) to compute the shoulder elevation moment from the measured force and pulley angle.

Benchtop Experiment

The benchtop prototype was used to quantify the moment generated by the spring-cam-wheel mechanism about the v-belt pulley axis (representing the glenohumeral joint) as a function of the shoulder elevation angle. Since the pulley radius (8*cm*) was larger than the estimated cable moment arm about the shoulder (r_s=6cm,Table 2-2), a pulley rotation of 67.5° corresponded to a shoulder elevation angle of 90°. Therefore, during the test, we manually rotated the pulley from 0° to 67.5°, then back to 0°. The pulley was rotated slowly while pausing briefly at 18 equidistant points (67.5°/18 = 3.75°) that were marked on the benchtop board. The movement between angle increments points was regulated using a metronome.

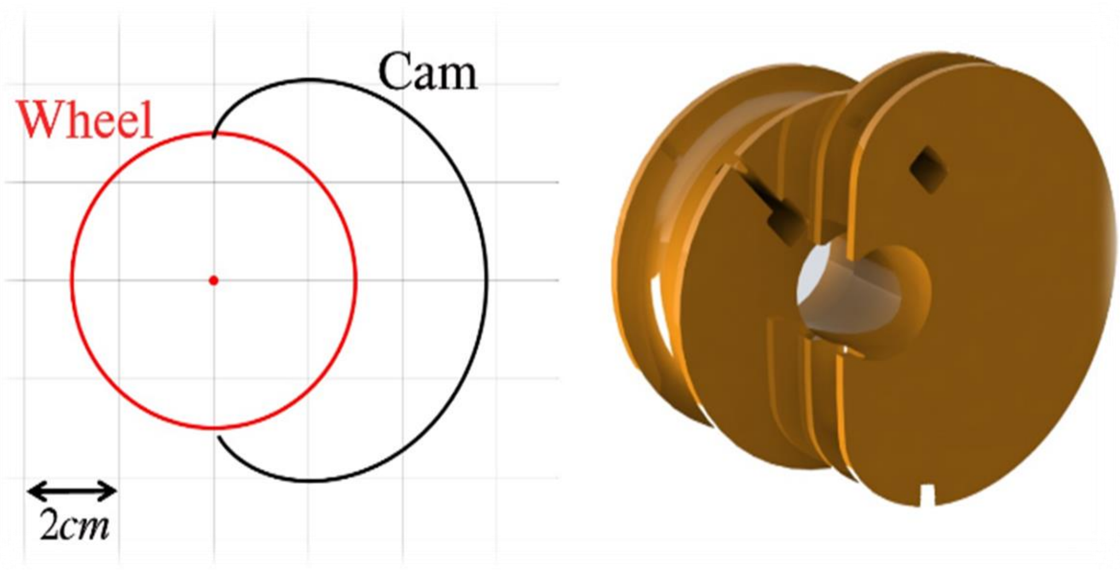

Figure 2-2. Developed profile (left) and CAD model (right) of the cam wheel optimized to compensate for half of the gravity moment.

Table 2-2. Optimized Design parameters

r_s **(cm)**	r_w **(cm)**	**A**	**B**	**C**
6.000	0.030	0.058	0.499	0.0000

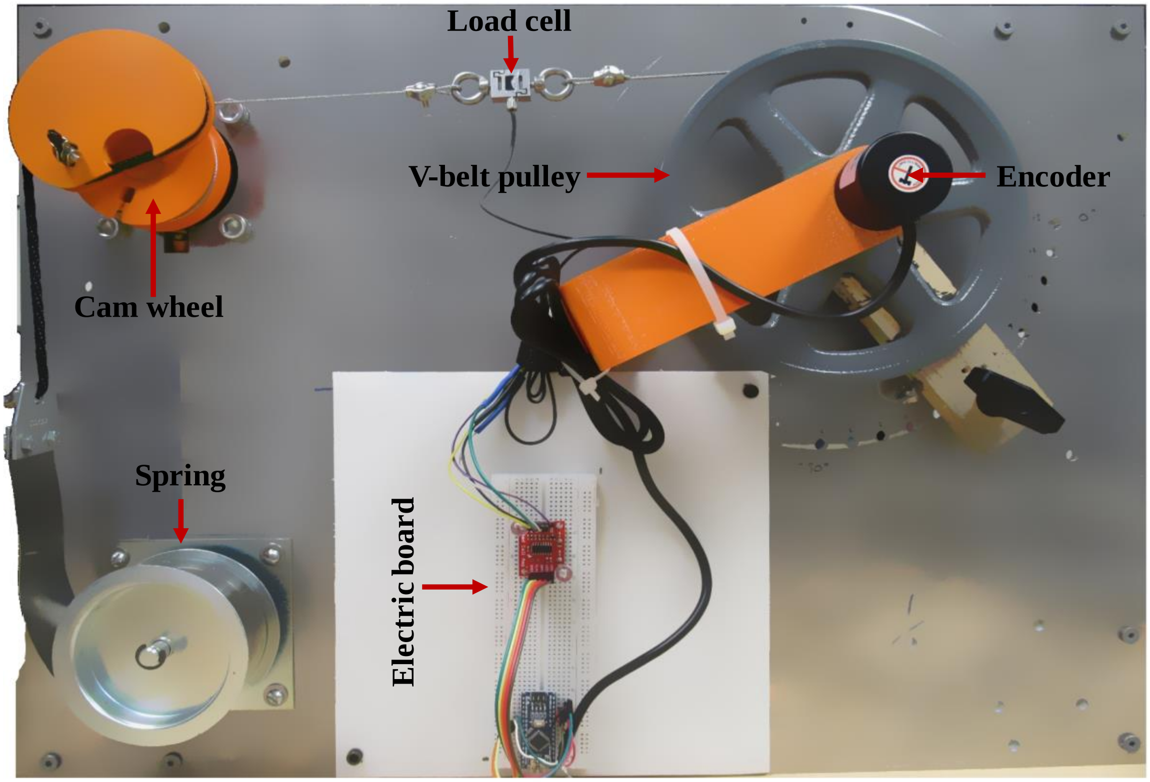

Figure 2-3. Benchtop prototype for mechanical evaluation of the spring-cam-wheel mechanism.

Exoskeleton Prototype

An initial prototype of the wearable passive shoulder exoskeleton was developed using similar components from the benchtop. The spring and cam wheel were installed on a thermoplastic back brace (Figure 2-4). The cam wheel was bolted on top of the back brace through a pressed-in ball bearing at its center. The wheel was attached to an arm cuff via a Bowden cable to facilitate the force transmission from the cam wheel to the arm. Two plastic pillow block spherical bearings were used to guide the Bowden cable across the shoulder to attach the upper arm cuff. Strap bands were used to wrap the arm cuff, back brace, and shoulder brace around the torso and arm. The exoskeleton prototype weighs 1.75 *kg* and the cost of materials was less than $100.

Qualitative Assessment of Exoskeleton Prototype

The exoskeleton was adjusted for testing on an able-bodied male (Figure 2-4, age=31, height=176*cm*, weight=79*kg*) whose anthropometry approximated that of a 50th percentile male. The participant performed repetitive shoulder elevation movements in the sagittal, scapular, and frontal anatomical planes. The user was instructed to perform the movements at his preferred speed and to provide verbal subjective feedback of the effectiveness, ease of use, discomfort, and compatibility of the device.

Results and Discussion

Figure 2-5 shows the experimental moment measured from the benchtop prototype and the theoretical moment. The experimental and theoretical moments match reasonably well, especially during simulated positive shoulder elevation from 0° to 90°. However, a larger moment (7.1% to 12.5% larger than theoretical) was generated during simulated negative shoulder elevation from 90° to 0° to stretch the spring back to its initial pre-loaded length. We suspect that the difference in measured moment between spring stretching and shortening is partly due to hysteresis, inherent to elastic springs, when energy is lost (as heat) during cyclic loading and unloading. The difference may also be due to friction at bearings and between the cables and components they wrap around. The leftward shift in the peak of the moment curve during simulated negative shoulder elevation was possible due to elasticity in the spring-cam-wheel mechanism and the higher load needed to overcome friction and stretch the spring.

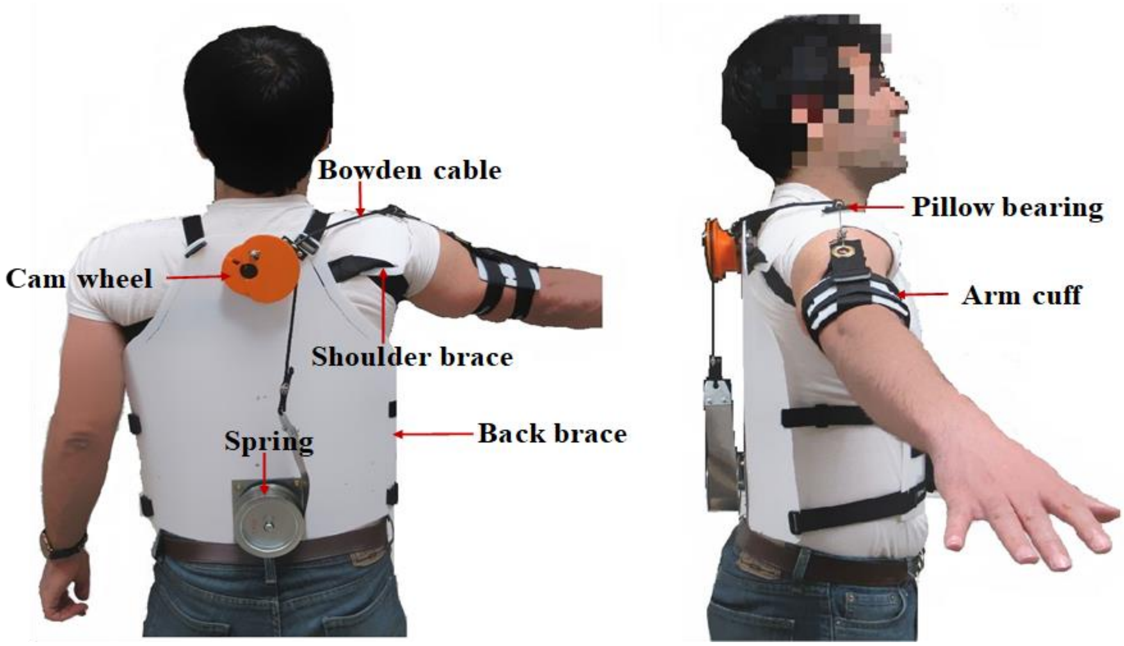

Figure 2-4. Exoskeleton prototype with the constant-force spring and optimized cam wheel to compensate for half of the shoulder elevation moment due to gravity.

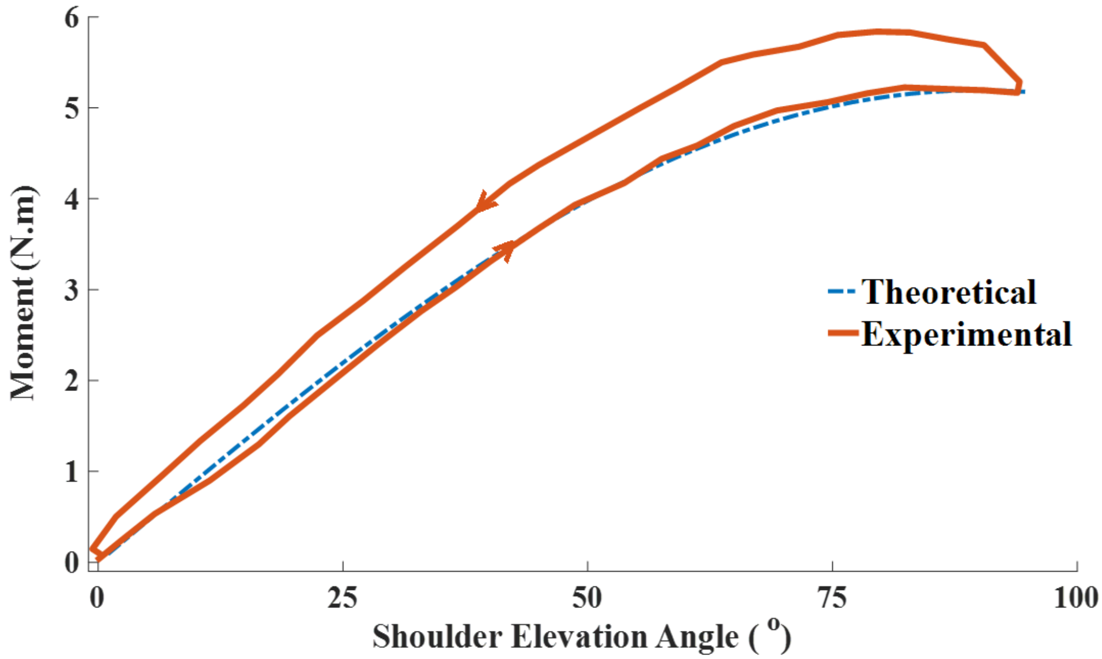

Figure 2-5. The benchtop moment generated by the spring-cam-wheel and the theoretical elevation moment vs. shoulder elevation angle. The arrows show the positive (spring shortening) and negative shoulder elevation.

During qualitative assessment of the exoskeleton, the user noted that the exoskeleton helped during positive shoulder elevation in different planes. One problem was that there was not enough padding between the user and exoskeleton, which caused discomfort. Another was that, even with the elbow extended, the weight of the upper extremity was not sufficient to return the arm to the side; the user needed to make extra effort to lower the arm. There were several factors that likely contributed to the need for extra effort. First, when lowering the arm, the shoulder brace and arm cuff were displaced relative to the body, resulting in inefficient force transfer from the arm to the spring-cam-wheel. The displacement also interfered with the relationship between the rotations of the cam wheel and shoulder, which effectively shifts the moment curve leftward and increases the exoskeleton moment across shoulder elevation angles. As observed with our benchtop model, the exoskeleton moment was higher when stretching the spring (i.e. hysteresis loop) during negative shoulder elevation movements. Finally, though the participant approximated a 50th percentile male, we may have overestimated the shoulder moment due to gravity and, thus, the exoskeleton moment needed to compensate for half of it.

Future Work & Conclusion

Understanding how wearable passive exoskeletons interact with their users is extremely important, especially if the devices will be worn by patients with shoulder disability or injury. As a first step toward understanding the human-exoskeleton interaction, in this study, we qualitatively evaluated the effectiveness and comfort of our wearable exoskeleton prototype. A quantitative evaluation was useful for quickly identifying some major design issues. However, in our future work, we will also quantify users' biomechanics (e.g., muscles activations, limb kinematics, and joint loads) with the exoskeleton to determine the extent to which it can provide clinically useful and safe movement assistance.

The problems we identified with our current exoskeleton prototype need to be addressed in future prototype iterations before it can be tested on more human participants. To prevent displacement of the shoulder brace, we will rigidly attach it to the back brace. Likewise, we will use larger elastic straps to attach the arm cuff to prevent displacement. We will add padding on all components that attach to the user to improve comfort.

In conclusion, our preliminary results demonstrated the promise of the spring-cam-wheel mechanism to provide nonlinear, customizable mechanical assistance to the shoulder. The exoskeleton is compact, lightweight, inexpensive, and easy to manufacture, which makes it appropriate for applications where portable and/or continuous shoulder movement assistance is needed. However, the current prototype design is user specific; ultimately, exoskeleton should be designed for a range of user anthropometry. Design refinements and future studies of exoskeleton performance and user biomechanics are needed to advance wearable passive shoulder exoskeletons toward clinical and other real-world applications.

Section 2-2: Design and Preliminary Evaluation of a Wearable Passive Cam-Based Shoulder Exoskeleton

Abstract

Mechanically passive exoskeletons may be a practical and affordable solution to meet a growing clinical need for continuous, home-based movement assistance. We designed, fabricated, and preliminarily evaluated the performance of a wearable, passive, cam-driven shoulder exoskeleton (WPCSE) prototype. The novel feature of the WPCSE is a modular spring-cam-wheel module, which generates an assistive force that can be customized to compensate for any proportion of the shoulder elevation moment due to gravity. We performed a benchtop experiment to validate the mechanical output of the WPCSE against our theoretical model. We also conducted a pilot biomechanics study (eight able-bodied subjects) to quantify the effect of a WPCSE prototype on muscle activity and shoulder kinematics during three shoulder movements. The shoulder elevation moment produced by the spring-cam-wheel module alone closely matched the desired, theoretical moment. However, when measured from the full WPCSE prototype, the moment was lower (up to 30%) during positive shoulder elevation and higher (up to 120%) during negative shoulder elevation compared to the theoretical moment, due primarily to friction. Even so, a WPCSE prototype, compensating for about 25% of the shoulder elevation moment due to gravity, showed a trend of reducing root mean square electromyogram magnitudes of several muscles crossing the shoulder during shoulder elevation and horizontal adduction/abduction movements. Our results also showed that the WPCSE did not constrain or impede shoulder movements during the tested

movements. The results provide proof-of-concept evidence that our WPCSE can potentially assist shoulder movements against gravity.

Introduction

Shoulder disability is a global health burden [2, 51] associated with several common orthopedic and neurological disorders, such as rotator cuff tear [41], peripheral nerve injury [10], muscle atrophy [11], and stroke [9]. Many people with shoulder disability have mild to moderate disability, meaning that they can still move their shoulder but with lower strength and range of motion than that of a healthy shoulder. Furthermore, people with shoulder disability often have trouble elevating the shoulder or holding the arm up against gravity [14, 16, 52]. Such functional deficits can make it hard for individuals to perform activities of daily living, particularly those for which gravity is a dominant external contributor to shoulder loading [17]. Consequently, shoulder disability can degrade a person's quality of life, self-esteem, and independence.

For people with shoulder disability, there is a clinical need for medical devices that can provide continuous, home-based movement assistance to compensate for gravity at the shoulder. Gravity compensation can assist upper extremity motor function by reducing the joint moments that muscles need to generate for a given movement [52]. We previously showed that anti-gravity assistance reduces activations of muscles that mainly contribute to positive shoulder elevation [53]. By reducing muscle activations, gravity compensation at the shoulder could help people perform upper extremity tasks with less effort and reduce muscle tissue loads. Additionally, for people with shoulder disability, gravity compensation could enhance range of motion and shoulder strength by encouraging them to be more physically active.

A wide variety of assistive and rehabilitative exoskeletons (sometimes called orthoses) have been developed for people with disabilities. Exoskeletons, which are typically worn on and transmit forces to the body [20], generate forces either actively or passively. Active exoskeletons, such as ARMin III [23] and MGA [43] use powered actuators, usually located near the joints, to generate forces that are transmitted to the body by rigid links. The high weight and rotational inertia reduce the transparency and power density of these exoskeletons. Some powered exoskeletons incorporate cable-driven mechanisms, which increases the power-to-weight ratio by allowing actuators to be mounted farther away from the user's joints. Cable-driven exoskeletons can have either serial or parallel design architecture. Serial cable-driven exoskeletons such as CADEN-7 [20], L-EXOS [54], and IntelliArm [55] still use rigid links with revolute joints but have lower weight and rotational inertia compared to conventional exoskeletons. Conversely, parallel cable-driven systems such as CAREX [56] and CARR-4 [57] use flexible cables with rigid joint cuffs to actuate the exoskeleton, which highly reduces the overall weight and moment of inertia of the moving parts. Active exoskeletons can provide more flexible assistance since the forces they generate can be modulated by control software. However, they are relatively heavy, large, expensive, and complex because they require motors, power sources (e.g., batteries), and computer hardware. These features make active exoskeletons less wearable and portable, limiting their application to clinical and laboratory settings.

Passive exoskeletons generate assistive forces using counterweights (such as the Mobility Arm, Nitzbon), rubber bands [32], or springs [26]. The assistive forces generated by passive exoskeletons are fixed according to their mechanical design and cannot be modulated in real time, as with active exoskeletons. However, passive exoskeletons are appealing for providing continuous, home-based movement assistance since they do not require electromechanical hardware (e.g., motors, batteries). Thus, passive exoskeletons are potentially more lightweight, cost-effective, low-maintenance, wearable, and portable than active exoskeletons.

Existing wearable passive shoulder exoskeletons compensate for gravity by releasing and storing energy from elastic springs as the shoulder is elevated and lowered, respectively [33]. Commercially available wearable passive shoulder exoskeletons, intended primarily for occupational or industrial settings, include EksoVest (Ekso Bionics Holdings, Inc., Richmond, CA), SuitX (US Bionics, Inc., Emeryville, CA), and AirFrame (Levitate technologies, Inc., San Diego, CA).However, these existing exoskeletons may not be ideal for assisting activities of daily living for people with shoulder disability because they are designed for application-specific and high-load tasks (e.g., overhead drilling and heavy lifting) [34, 35]. They also typically have a high profile (i.e., they extend out far from the user's body) because they incorporate rigid linkages and mechanical joints.

There are several passive devices that have been developed and commercialized for clinical applications. Early devices include passive mobile arm supports, such as SaeboMAS, that mount on a wheelchair, wall, or table [30, 31] and compensate for gravity using counterweights [58] or parallelograms that are equipped with spring-cam [26] or spring mechanisms. The Wilmington Robotic Exoskeleton (WREX) [32], is another wheelchair-mounted arm support that uses elastic bands to compensate for decoupled gravity at the shoulder and elbow joints. T-WREX, a more recent version of the WREX [27, 33], was equipped with position and grip sensors that permit movement therapy through virtual interfaces (e.g., computer games). These passive devices can completely balance the arm and are mostly intended for patients who have severe neurological shoulder disability. However, their level of gravity compensation is usually unmodulated over the shoulder's range of motion, and they must be mounted on rigid frames or fixed bases. These features make such devices an inappropriate solution for patients with greater mobility and only mild to moderate shoulder disability.

We propose a new wearable, passive, cam-based shoulder exoskeleton (WPCSE) that addresses limitations of existing devices for providing continuous, at-home assistance to patients with mild to moderate shoulder disability. The main, novel contribution of the WPCSE is a spring-cam-wheel module whose assistive force can be customized for each patient to compensate for any proportion of the shoulder elevation moment due to gravity. Additionally, the assistive force is transmitted to the arm through a Bowden cable that passes through self-aligning spherical bearings, which allows the WPCSE to assist movements across a wide range of shoulder elevation planes. Since the spring-cam-wheel module is compact and lightweight, the WPCSE could potentially be worn on the body comfortably throughout the day under clothing. The overall objective of our study was to design, fabricate, and preliminarily evaluate a WPCSE prototype that includes the novel spring-cam-wheel mechanism. We first developed a theoretical model and prototype design of the WPCSE. We then fabricated a physical benchtop model to quantify the mechanical performance of the spring-cam-wheel module and WPCSE. We expected that friction and spring hysteresis, which were unaccounted for in our theoretical model, would reduce the assistive moment generated by the physical benchtop model compared to the theoretical model. Finally, we performed a pilot biomechanics study to test the concept that the WPCSE could reduce the activity of muscles crossing the shoulder; secondarily, we evaluated the effect of the WPCSE on shoulder kinematics.

Methods

Design of the WPCSE

System Concept

Our WPCSE compensates for gravity at the shoulder using an elastic spring whose force is transmitted to the arm through a Bowden cable that passes over the superior aspect of the shoulder. A common example of a gravity compensation system is the use of counterweights to balance the weight and reduce the force required to raise and lower an elevator car. Instead of counterweights, our exoskeleton uses a spring that is stretched when the arm is beside the body and pulls on the Bowden cable as the arm elevates.

As the shoulder elevation angle increases from 0° to 90°, the magnitude of the negative shoulder elevation moment due to gravity increases. We designed our exoskeleton to provide increasing assistance in proportion to the increasing gravity moment. This was accomplished by incorporating a cam-wheel component between the spring and arm (Figure 2-6). The variable-radius cam and a constant-radius wheel are fixed to each other so that they rotate together about the same axis. As shoulder elevation angle increases, the moment arm of the of a wrapping rope (connects the spring and cam) with respect to the cam-wheel increases while the moment arm between a Bowden cable (crossing the shoulder) and constant-radius wheel stays the same. Thus, the cam-wheel functions as a gearing mechanism that modulates the Bowden cable's pulling force according to the moment arm ratio between the cam and wheel. The Bowden cable was clamped at the superior aspect of the shoulder using a self-aligning spherical bearing. The bearing allowed the Bowden cable to pivot and align with the arm across a large range of elevation plane angles. All components were mounted on a custom back brace, while the Bowden cable was attached to an arm cuff.

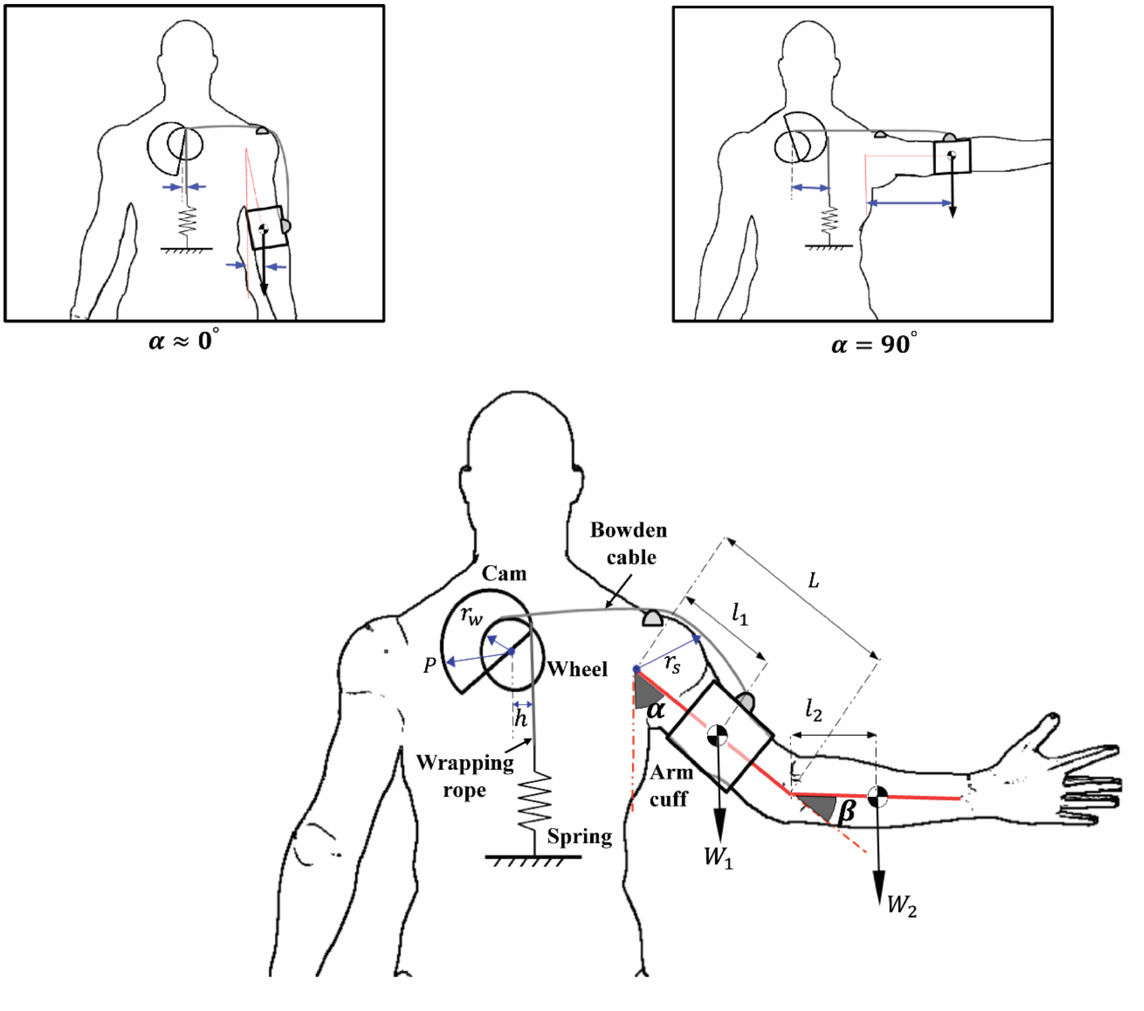

Figure 2-6. Schematic diagram of shoulder exoskeleton system concept (posterior view on right arm). Upper left and right figures represent two extreme configurations for shoulder elevation in the frontal plane. As the shoulder elevates from the 0° (upper left figure) to 90° (upper right figure), the cam-wheel rotates and adjust its effective moment arm relative to the wrapping rope to modulate the Bowden cable pulling force.

The proposed exoskeleton improves on previous wearable passive shoulder exoskeleton designs in several ways. First, it provides mechanical assistance through a soft, cable-driven mechanism instead of rigid links, which (1) enables us to place force-generating components (i.e., the cam-wheel and spring) away from the shoulder joint, (2) permits shoulder rotations to occur freely about biological axes of rotation without conflicting with axes of rigid linkages, and (3) reduces the exoskeleton's weight. Second, the geometry of the cam-wheel gearing component can be customized to "tune" the gravity-compensating force to support a wide range of tasks and users. Finally, with our compact spring-cam-wheel module design, the exoskeleton can maintain a low profile.

Calculation of Shoulder Elevation Moment due to Gravity

The magnitude of the gravity moment about the shoulder depends on the upper extremity posture, while the orientation of the gravity moment depends on the orientation of the torso with respect to gravity. In our design calculations, we assumed that the torso is upright and aligned with the gravity vector. In this case, gravity will primarily generate a moment in the direction of negative shoulder elevation and, thus, can be calculated with a planar model of the arm. The shoulder gravitational moment was calculated as:

$$\tau_G(\alpha, \beta) = W_1 l_1 \sin(\alpha) + W_2(\mathrm{L}\sin(\alpha) + l_2 \sin(\alpha + \beta)) \quad (1)$$

where W_1 is the weight of the arm; W_2 is the sum of the forearm and hand weight; l_1 is the distance from the glenohumeral joint center to the arm's center of gravity; l_2 is the distance from the elbow joint center to the center of gravity of the combined forearm-hand segment; L is the length of the arm segment; and α and β are the shoulder elevation and elbow flexion angles, respectively (Figure 2-6). Equation (1) shows that the gravitational moment depends on both shoulder and elbow posture and increases nonlinearly as the shoulder elevates from 0° to 90°. We estimated the value of τ_G in (1) based on anthropometric data of a 50th percentile male (age 27.45 ± 5.64 years) and assuming a fully extended elbow [59, 60].

$$\tau_G(\alpha, 0) = 10.4 \ \sin(\alpha) \ \mathrm{Nm} \quad (2)$$

Selection of Elastic Spring Component

The force-generating components of previous passive exoskeletons are typically either zero-free-length springs, constant-force springs [61], or rubber bands [62]. For the shoulder joint, which has the largest range of motion of all human joints, an ideal passive element must be able to generate force over large deflections. We selected a constant-torque spring (Figure 2-7) which has a compact design since their deflection is achieved by rotating a set of spools. The constant-toque spring also simplifies the design of the cam since it makes the shoulder gravity moment the only variable in Eq. (5). In a constant-torque spring, a coiled, elastic metal strip is wrapped over a storage spool. The metal strip is stretched by wrapping and rotating it around an output spool in the opposite direction in which it is coiled. Energy is released from the spring when the metal strip unwinds from the output spool back onto the storage spool. When the spring is stretched, it generates constant torque τ_{spring} about the axis of the output spool [63]. We converted the torque into a tension force in a wrapping rope by attaching a pulley to the output spool (Figure 2-7).

Based on the gravity moment in Eq. (2) and (5), we selected a commercially available constant-torque spring that can nominally produce a torque, $\tau_{spring} = 0.84 \pm 0.08\ Nm$ when wound 10 turns around the output spool, according to the manufacturer (SV12J192, Vulcan Spring & Manufacturing, Telford, PA, USA). The spring material is 301 Stainless steel and the design parameters recommended by the manufacturer are shown in the table in Figure 2-7.

The torque generated by a constant-torque spring is higher during the stretching phase (i.e., spring winding onto the output spool) than during the recoil phase (i.e., spring winding back onto the storage spool). We opted to perform the design of WPCSE based on the torque generated during the recoiling phase during which it assists positive shoulder elevation movements. The torque, τ_{spring}, that we measured (see Experiments section.) from the constant-torque spring during the recoiling phase was $0.67 \pm 0.02\ Nm$.

Development of Cam-Wheel Profile

The cam-wheel is the key component of the WPCSE that adjusts the cable pulling force to output the desired increasing positive shoulder elevation moment with increasing shoulder elevation angle (Figure 2-8).

The rotation of the wheel (φ) is related to the shoulder elevation angle (α) based on simple gear modeling, and can be described as (3):

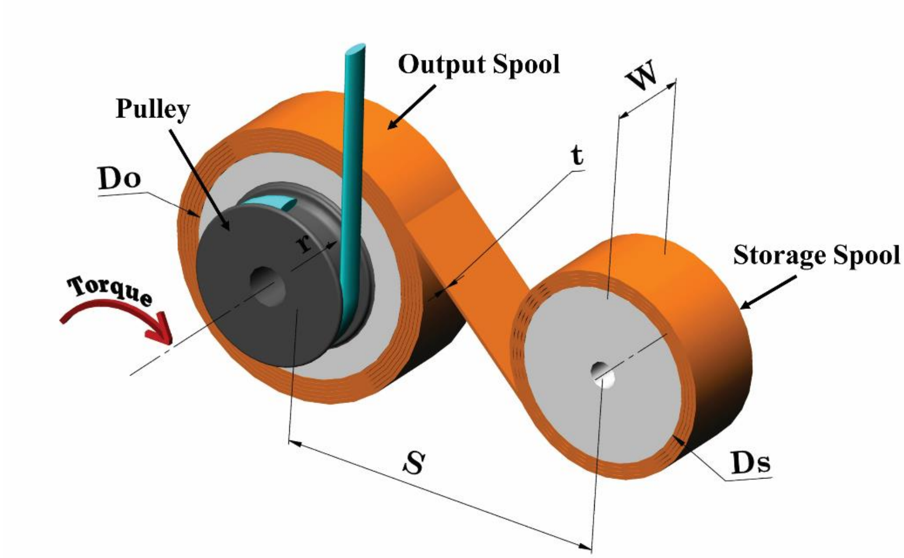

t (m)	W (m)	S (m)	Do (m)	Ds (m)
0.0003	0.016	0.660	0.062	0.036

Figure 2-7. Schematic view of a constant-torque spring. The geometrical properties of the selected spring assembly are listed in the table.

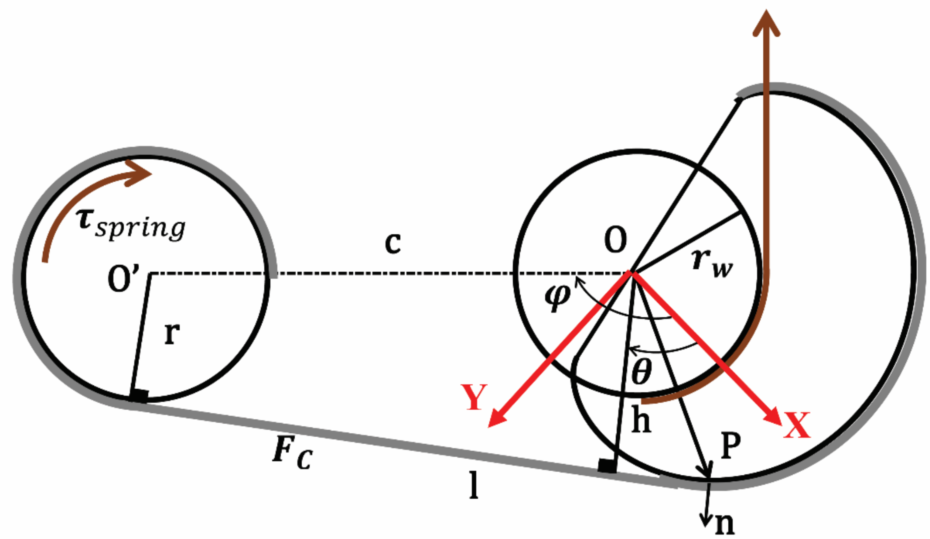

Figure 2-8. Schematic representation of the spring-cam-wheel module.

$$\varphi = \frac{r_s}{r_w}\alpha \tag{3}$$

where r_w represents the radius of the constant-radius wheel and r_s is the moment arm of the shoulder cable about the glenohumeral joint. Theoretically, the WPCSE can be designed to generate an assistive positive shoulder elevation moment τ_E that counteracts some proportion, k, of the gravity moment, $\tau_G(\alpha, 0)$. A value of $k = 1$ is expected to completely balance the upper extremity weight in all static shoulder elevation postures. However, in this study, we set $k = 1/4$, for three main reasons. First, during dynamic positive shoulder elevation movements, full static assistance coupled with the inertia of the moving upper extremity mass would exceed the negative shoulder elevation moment due to gravity. Second, our preliminary theoretical model did not account for friction and other factors that increase the WPCSE moment during negative shoulder elevation, since the quantitative effect of these factors was unknown at the time of the study. Third, in a preliminary study of an exoskeleton prototype with $k = 1/2$, some users needed to actively lower their arm with the WPCSE [64] to counteract the exoskeleton moment.

$$\tau_E = k\tau_G(\alpha, 0) \tag{4}$$

For the cam-wheel to be statically balanced, assuming no loss due to friction:

$$F_C(\varphi)h(\varphi) - \frac{r_w}{r_s}\tau_E = 0 \tag{5}$$

where $F_C(\varphi)$ is the tension force in the wrapping rope that connects the constant-torque spring to the variable-radius cam, and $h(\varphi)$ is the moment arm of the wrapping rope with respect to the cam's axis of rotation.

We first determined the form of $h(\varphi)$ in (5) to calculate the final geometry of the cam. The value of r_s was set to $0.06m$, which we estimated from a computational musculoskeletal model [65]. The cable tension force was calculated by dividing τ_{spring} by the radius r of the pulley which is attached to the output spool. To determine the form of $h(\varphi)$ and values of r_w and r, we performed a constrained, global numerical optimization using the GlobalSearch function in MATLAB (MathWorks, Inc., Natick, MA). The optimization identified parameter values that minimized the sum of the squared error between the actual (τ_E) and desired ($\frac{1}{4}\tau_G$) assistive shoulder elevation moment by the exoskeleton, $||\tau_E - \frac{1}{4}\tau_G||^2$. From among five forms for $h(\varphi)$, including linear, quadrature, polynomial, power, and sinusoidal functions, that we tested in our global optimization procedure, we chose a sinusoidal form because it generated the lowest error [64]. This makes sense since the form of τ_G in (2) is also sinusoidal.

$$h(\varphi) = A\sin(B\varphi) + C \quad (6)$$

The design parameters computed during the global optimization procedure are displayed in Table 2-3.

We then determined the geometrical profile of the cam analytically using a complex form of the loop closure method [66]. The coordinate of the contact point, P, between the wrapping rope and the cam surface (Figure 2-8), can be represented as:

$$\vec{P} = ce^{i\varphi} + e^{i\theta}(r - li) \quad (7)$$

where c is the center-to-center distance between cam-wheel and the spring output spool; l is the length of the unwrapped portion of the wrapping rope; and θ is the angle of the moment arm. The angle φ can be written as a function of the moment arm $h(\varphi)$:

$$\varphi = cos^{-1}\left(\frac{h-r}{c}\right) + \theta \quad (8)$$

We set $c = 0.010\ m$ to have the final integrated spring-cam-wheel module as compact as possible while still maintaining clearance between the cam-wheel component and the constant-torque spring. The value of l was derived using the contact condition between the cable and the cam $\vec{n} \cdot \left(\frac{d\vec{P}}{d\emptyset}\right) = 0$. This leads to the following equation to calculate l.

$$l = C\frac{d\varphi}{d\theta}\sin(\varphi - \theta) \quad (9)$$

where $\frac{d\varphi}{d\theta}$ can be determined by taking the derivative of (8):

$$\frac{d\varphi}{d\theta} = 1 - \frac{1}{\sqrt{C^2 - (h-r)^2}}\frac{dh}{d\theta} \quad (10)$$

Table 2-3. Optimized design parameters

r_w *(m)*	r *(m)*	***A***	***B***	***C***
0.030	0.030	-0.057	-0.492	0.000

Equations (7) to (10) are sufficient to develop the final profile of the cam-wheel (Figure 2-9A). The coordinates of three hundred points representing the cam profile were obtained to develop its computer-aided design (CAD) model (Figure 2-9B).

Exoskeleton Prototype

Based on the design parameters and dimensions above, we fabricated a prototype of the WPCSE using off-the-shelf and 3D-printed components, as described below.

Spring-cam-wheel Module Assembly

The CAD models of the cam-wheel, spring spools, and pulley were developed in Solidworks software (2018, Dassault Systémes SolidWorks Corp., MA, USA). From the CAD models, the parts were 3D printed in ABS plastic (Figure 2-9B, C, D). The constant-torque spring and output pulley were assembled and installed on a 304-alloy stainless-steel sheet (14 × 17 × 0.16 cm3) using Clevis pins and retainer rings. To facilitate the rotation of the spools, two deep-groove ball bearings (688-ZZ) were pressed in each spool. The cam-wheel was equipped with a single row ball bearing (Koyo, EE4C3) that was bolted to the stainless sheet. An inelastic, solid-braid nylon rope (9.50 mm thickness) connected the cam and spring pulley. To prevent the constant-torque spring from suddenly winding onto the storage spool, a mechanical stopper (pin inside circular groove) was incorporated in the output spool to limit its rotation to 350°. A similar stopper was incorporated in the cam-wheel to limit its rotation such that the WPCSE applied force to the arm for shoulder elevation angles between 0° and 90°.

Custom Braces

The WPCSE prototype consisted of a back brace and an arm cuff, on which other components were mounted. We custom-made a thermoplastic back brace (acrylic sheet) by casting a person’s torso with plaster gauze and fabricating positive and negative molds. The back brace was attached to a back-support vest that straps across the shoulder and around the waist (Figure 2-10A). The inside of the back brace was covered with padding to improve fit and comfort. A thermoplastic cuff was attached to an adjustable, slide-on elbow support that straps to the arm both above and below the

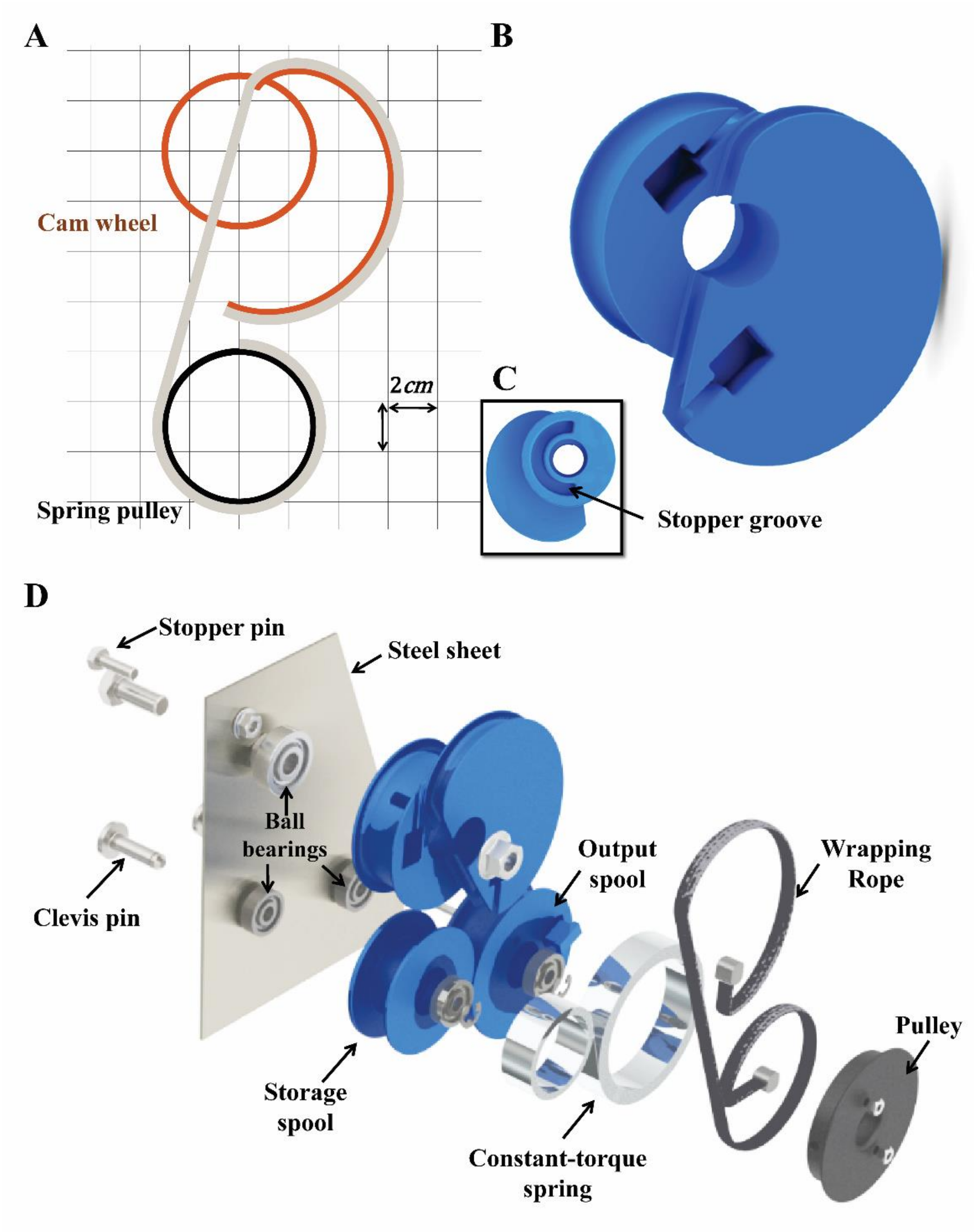

Figure 2-9. A) Profile of the cam-wheel. B) CAD model of the cam-wheel. C) Posterior view of the cam-wheel. D) Exploded view of the spring-cam-wheel module assembly.

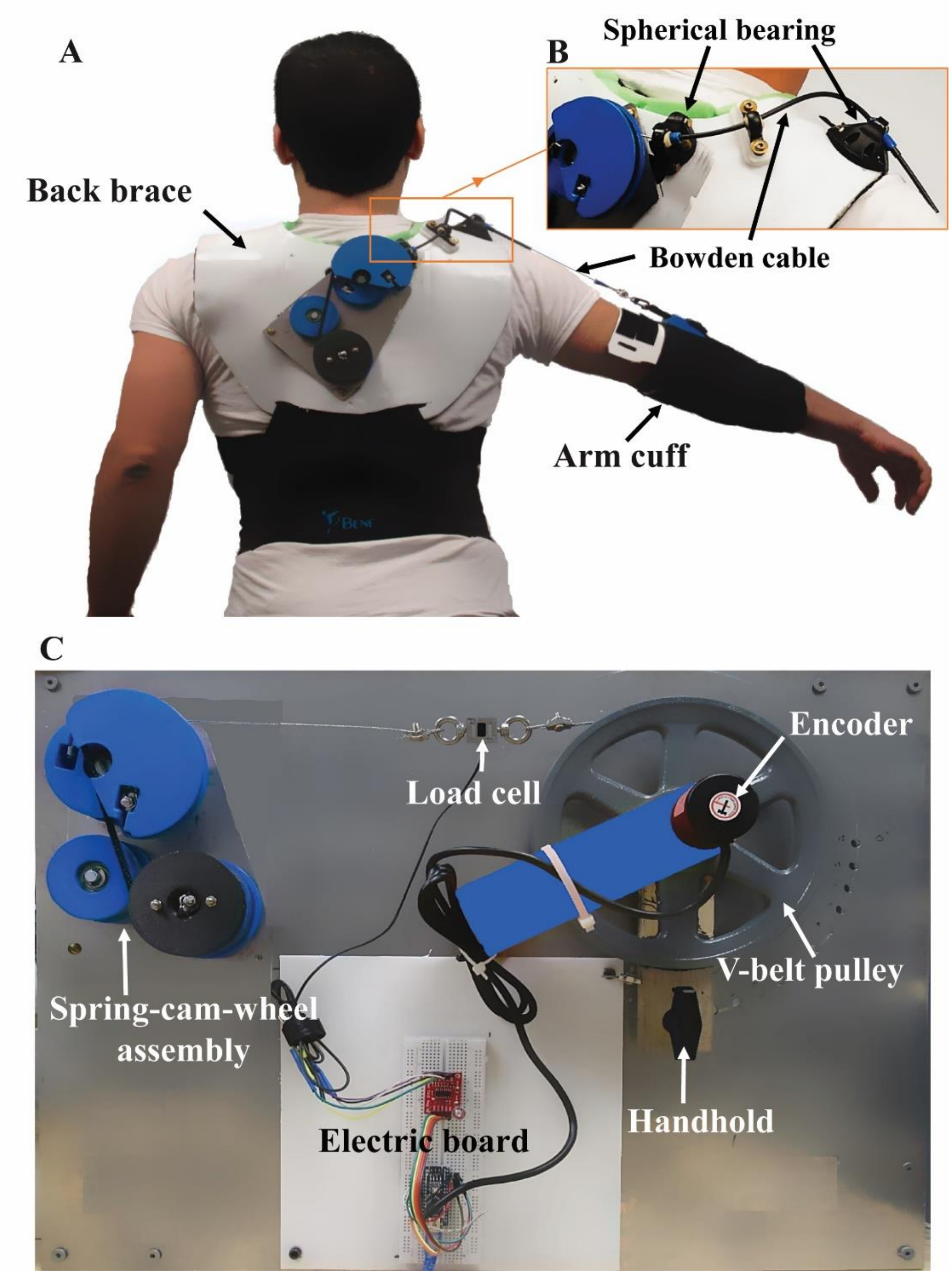

Figure 2-10. A) WPCSE prototype. B) Bowden cable routing path over the shoulder. C) Benchtop prototype.

elbow joint (Figure 2-10A). This prevented the arm cuff from sliding proximally while still permitting elbow flexion.

Cable Routing

A Bowden cable transmitted the force from the spring-cam-wheel module assembly to the arm cuff. A Bowden cable consists of an inner cable (commonly of steel) and an outer casing (a composite of helical steel wire and a plastic outer sheath). The inner wire wrapped around the wheel on one end and connected to the arm cuff on the other end using a spring snap.

The Bowden cable casing was clamped at each end and in the middle by self-aligning spherical bearings (maximum pivot angle = 60°) that were bolted to the back brace (Figure 2-10B). Clamping the casing was required so that the inner wire could move relative to it and transmit the pulling force. The spherical bearings permitted the cable to pivot and align with the arm as elevation plane angle changed. The path of the Bowden cable was designed to minimize friction (i.e., by avoiding bends with small radius of curvature). A small (~5 *cm*) length of casing extended distally from the bearing mounted over the shoulder to enable the inner cable to curve smoothly over the shoulder.

Prototype Specifications

The final prototype of the WPCSE weighed 1.82 *kg*, of which 0.83 *kg* was due to the spring-cam-wheel module assembly, 0.82 *kg* was due to the back brace, and 0.17 *kg* was due to the arm cuff. The total weight of the WPCSE is relatively low and mostly borne on the torso, so we do not expect it to have a large effect on user fatigue. It was also designed to be donned/doffed independently by the user. However, the length of the inner wire of the Bowden cable needed to be adjusted once for each user according to their anthropometry.

Benchtop Setup

In addition to the WPCSE prototype, we developed a benchtop prototype (Figure 2-10C) to preliminarily evaluate the mechanical output of the WPCSE and its components. The benchtop prototype consisted of a v-belt pulley (radius = 0.08 *m*) representing the Bowden cable wrapping over the shoulder; the pulley had an embedded handhold so that it could be rotated manually to mimic shoulder elevation movements. Depending on the test (*Experiments* section), the v-belt pulley was connected to either the spring-cam-wheel assembly or to the WPCSE. A rotary encoder (LPD-3806-600bm-G5-24c, GTEACH, China) was installed on top of the v-belt pulley to measure its rotation angle for computing the mimicked shoulder elevation angle. An s-type load cell (ATO-LC-S04, 50 kg capacity, ATO, Diamond Bar, CA, USA) was also placed along the cable path to measure its pulling force. An Arduino Nano board was programmed to compute the shoulder elevation moment and angle from the measured force and angle, respectively.

Experiments

Mechanical Performance Evaluation

Using the benchtop prototype, we measured the torque generated by the spring alone, the spring-cam-wheel module alone, and the entire WPCSE. The spring-cam-wheel module and WPCSE were essentially the same except that the WPCSE also included the Bowden cable and its routing path on the back brace. The WPCSE was placed on the fabricated positive mold of the torso and fixed to a workbench. The side of the Bowden cable that attaches to the arm cuff was connected to the v-belt pulley. To test the spring-cam-wheel module alone, we fixed it to the benchtop board and connected the wheel to the v-belt pulley via the inner Bowden cable (Figure 2-10C). The v-belt pulley was manually rotated from 0° to 67.5° to simulate the shoulder elevation from 0° to 90°. The angle difference was due to the difference between the v-belt pulley radius and the estimated moment arm of the Bowden cable about the shoulder.

The v-belt pulley was rotated manually counterclockwise (i.e., simulated positive shoulder elevation) and clockwise (i.e., simulated negative shoulder elevation), three times at a slow speed (i.e., quasi-static condition). Cable pulling force and pulley rotational angle data were collected at 20 Hz. The shoulder elevation moment was calculated by multiplying the cable pulling force by the radius of the v-belt pulley. Measured pulley rotation angles were multiplied by $\frac{4}{3}$ (pulley-to-shoulder moment arm ratio) to compute the simulated shoulder elevation angles. The final moment-angle relationships for the spring-cam-wheel module and WPCSE were obtained by resampling the simulated positive and negative shoulder elevation phases into 50 points each and averaging across the three repetitions.

To test the constant-torque spring alone (i.e., pre-cam), the spring was installed on the benchtop board. The output pulley was attached to the v-belt pulley via an inner Bowden cable. We wound the spring strip 10 turns around the output spool. The torque of the spring was calculated by multiplying the cable tension force by the radius of output pulley (0.03 *m*). We computed the spring's torque-angle relationship as described above for the spring-cam-wheel module and WPCSE.

Biomechanical Performance Evaluation

Participants

We conducted a biomechanics study to preliminarily determine the effect of the WPCSE on the neuromuscular activity of muscles crossing the shoulder and on shoulder kinematics. Eight able-bodied (6 male and 2 female) volunteered to participate in the pilot study (mean ± SD, age = 33 ± 9 *years*, height = 1.76 ± 0.08 *m*, weight = 72 ± 7 *kg*). Eligible participants were 18 to 70 years old with no self-reported history of upper limb pain or injury within the previous year.

Instrumentation and Experimental Procedure

The experimental procedure was approved by the institutional review board at the University of Tennessee, Knoxville (UTK IRB-19-04990-FB, 2020), and all participants provided their informed consent. Participants were fitted with the WPCSE and asked to perform three different shoulder movements with and without assistance (Figure 2-11A). For the without-assistance condition, the Bowden cable was detached from the arm cuff. The movements were shoulder elevation in the sagittal and frontal planes (Figure 2-11B, C), and shoulder adduction/abduction in the horizontal plane (Figure 2-11D). These movements were chosen because they capture the functional ranges of shoulder motion required to perform activities of daily living [67] and used clinically to evaluate shoulder mobility [68]. For each trial, participants moved the shoulder from 0° to 90° and back to 0° in the relevant plane (Figure 2-11). The trials were performed with the elbow fully extended, at the participant's preferred speed, and with a brief (1-2 seconds) pause at the upper (90°) and lower (0°) limit of movement.

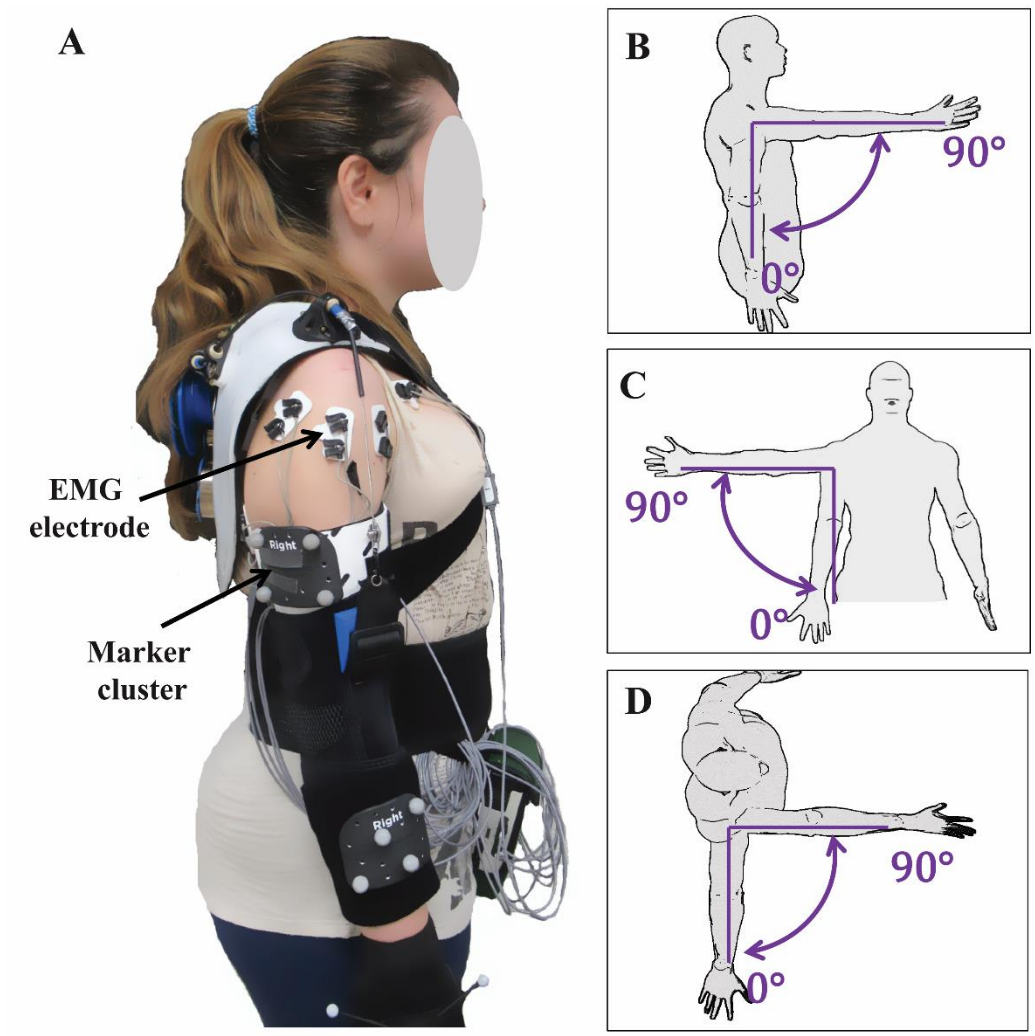

Figure 2-11. A) A participant with WPCSE, EMG electrodes, and reflective marker clusters. B). Shoulder elevation in the sagittal plane. C) Shoulder elevation in the frontal plane. D) Shoulder adduction/abduction in the horizontal plane.

In each trial, participants performed 10 continuous repetitions of each shoulder movement while sitting upright on a stool. We randomized the order of exoskeleton condition (with and without WPCSE) and, within each exoskeleton condition, randomized the order of shoulder movements. Participants rested between trials for about 30 seconds to reduce the likelihood of fatigue.

During the trials, we synchronously measured electromyograms (EMG) and kinematics of the participants. We recorded EMG from several muscles crossing the shoulder, including anterior (AD), middle (MD), and posterior deltoid (PD), pectoralis major (PM), latissimus dorsi (LD), infraspinatus (ISP), trapezius (TRAP), biceps brachii (BB), and triceps brachii (TB) (Fig. 6A). EMG data were recorded at a sampling frequency of 3000 Hz (TeleMyo 2400 G2, Noraxon, AZ, USA) using surface electrodes (bipolar silver/silver chloride electrodes) attached to the participant's skin. Before starting the experiment trials, baseline EMG of muscles at rest and during maximum voluntary contraction (MVC) were recorded based on a previously described method [69]. We used a 7-camera infrared motion capture system (OptiTrack Prime 13) to track the three-dimensional positions of reflective marker clusters that were placed on the participant's upper back, arm, forearm, and hand [70]. Marker cluster position data were recorded at 120 Hz.

Data Processing

The EMG data for each movement repetition were divided into positive elevation/adduction, and negative elevation/abduction phases based on the kinematics. The raw EMG data was band-pass filtered at 10-500 Hz, full wave rectified, and low pass filtered with a 4^{th} order Butterworth filter at a cut-off frequency of 6 Hz. For each participant, the processed EMG for each muscle were normalized by the maximum processed-EMG value recorded from the respective muscle during MVCs.

The *MotionMonitor* software (V8.0, Innovative Sports Training, Inc., Chicago, IL, USA) was used to compute and resample (at 3000 Hz) the shoulder elevation and plane of elevation angles from the marker cluster position data. Shoulder elevation angle (sagittal and frontal trials only) or elevation plane angle (horizontal trials only) was considered for further analyses since movements were predominantly along these degrees of freedom. Angular velocity was also calculated by taking the derivative of the predominant shoulder angles.

The root mean square (nRMS) of the normalized EMG, angular displacement, and angular velocity were calculated and averaged across eight middle repetitions (i.e., out of 10 repetitions) for each trial and movement phase [71, 72]. All data processing was performed using MATLAB packages and custom-made scripts (MathWorks, Natick, MA).

Statistical Analysis

Paired Student's t-tests were used to compare nRMS EMG between exoskeleton conditions. Normality of nRMS EMG data was evaluated by Kolmogorov-Smirnov test ($\alpha = 0.05$). When normality test was violated, nonparametric Wilcoxon rank-sum test was used. Statistical analysis was executed using SPSS 27 (IBM Corporation). We also perform paired t-tests by one-dimensional statistical parametric mapping (SPM) [73] to compare the one-dimensional angular displacement and velocity time series between exoskeleton conditions ($\alpha = 0.05$). Since the biomechanics experiment was preliminary, we did not correct for multiple tests so that we could identify potential trends in differences between exoskeleton conditions.

Results

Mechanical Performance

Under quasi-static conditions, the constant-torque spring was able to produce a nearly constant torque ($0.77 \pm 0.02\ Nm$) that was in the range of the manufacturer's specified nominal torque ($0.84 \pm 0.08\ Nm$) for the stretching phase (Figure 2-12). The torque generated by the spring during the unloading phase was $0.67 \pm 0.02\ Nm$, which was 20% lower than the nominal torque.

For the spring-cam-wheel module assembly, the measured moment matched reasonably well with the theoretical moment during simulated positive shoulder elevation. This was expected because we optimized the design parameters of the cam-wheel based on the torque value that spring generates during its unloading phase. However, a larger moment, up to 50% larger than the theoretical moment, was required during simulated negative shoulder elevation to stretch the spring. The difference in

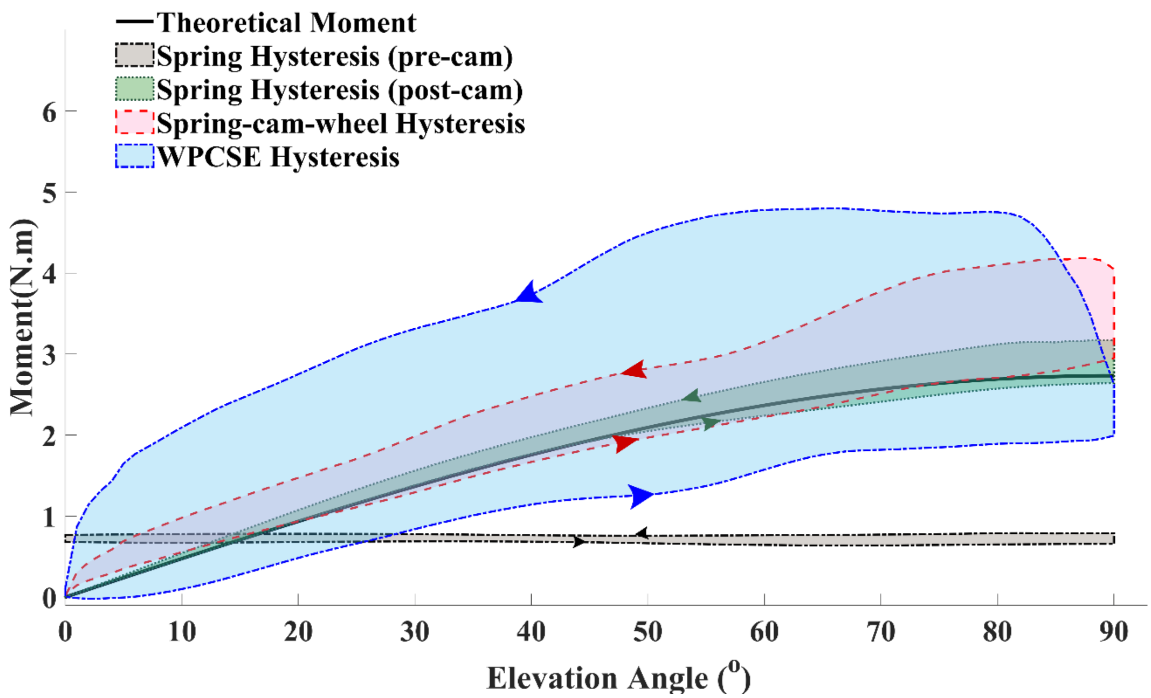

Figure 2-12. Joint moment produced by the constant-torque spring (pre- and post-cam), spring-cam-wheel module, and WPCSE during simulated shoulder elevation. The shaded regions indicate the degree of hysteresis, which is the difference in torque or moment between the positive and negative shoulder elevation phases.

moment between simulated positive and negative shoulder elevation phases was even greater for the WPCSE (Figure 2-12, blue area); the measured WPCSE moment was up to 30% lower than the theoretical moment during simulated positive shoulder elevation, and up to 120% higher than the theoretical moment during simulated negative shoulder elevation.

Biomechanical Performance

During positive elevation/adduction, nRMS EMG values of several muscles tended to be lower for trials with exoskeleton assistance across the participants (Figure 2-13). However, the reduction in nRMS was only significant for the MD (33%) and ISP (20%) muscles in the sagittal plane (*p-value* < 0.05). The mean of muscle activity across the subjects was also reduced, but not significantly so, for the AD (17%), PD (13%), and TRAP (18%) muscles during positive shoulder elevation in the sagittal plane; for the AD (7%), MD (10%), PD (22%), ISP (19%), and TRAP (18%) muscles during positive shoulder elevation in the frontal plane; and for the AD (10%), MD (12%), PD (8%), ISP (17%), and TRAP (21%) muscles during horizontal adduction. During negative shoulder elevation/abduction movements (Figure 2-14), nRMS EMG was significantly reduced for the TRAP muscle in the frontal (30%) and horizontal (17%) planes (*p-value* < 0.05). The average of nRMS also tended to be lower, but not significantly so, for the AD (10%), and ISP (15%) muscles in the sagittal plane; for the PD (20%), and ISP (21%) muscles in the frontal plane; and for the AD (13%), MD (9%), PD (9%), and ISP (15%) muscles in the horizontal plane.

The SPM results showed no significant difference for the shoulder angular displacement and velocity between with and without exoskeleton conditions. Although the standard deviation (blue shadows) of normalized angular displacement and velocity of shoulder movements was higher with exoskeleton assistance, the spatial/temporal aspects of their profiles and the durations of the acceleration/deceleration phases were similar between assistance conditions (Figure 2-15, Figure 2-16).

Discussion

We presented the design of a wearable passive cam-based shoulder exoskeleton (WPCSE), whose novel feature is a spring-cam-wheel module that can provide nonlinear, customizable mechanical output; in our case, the mechanical output

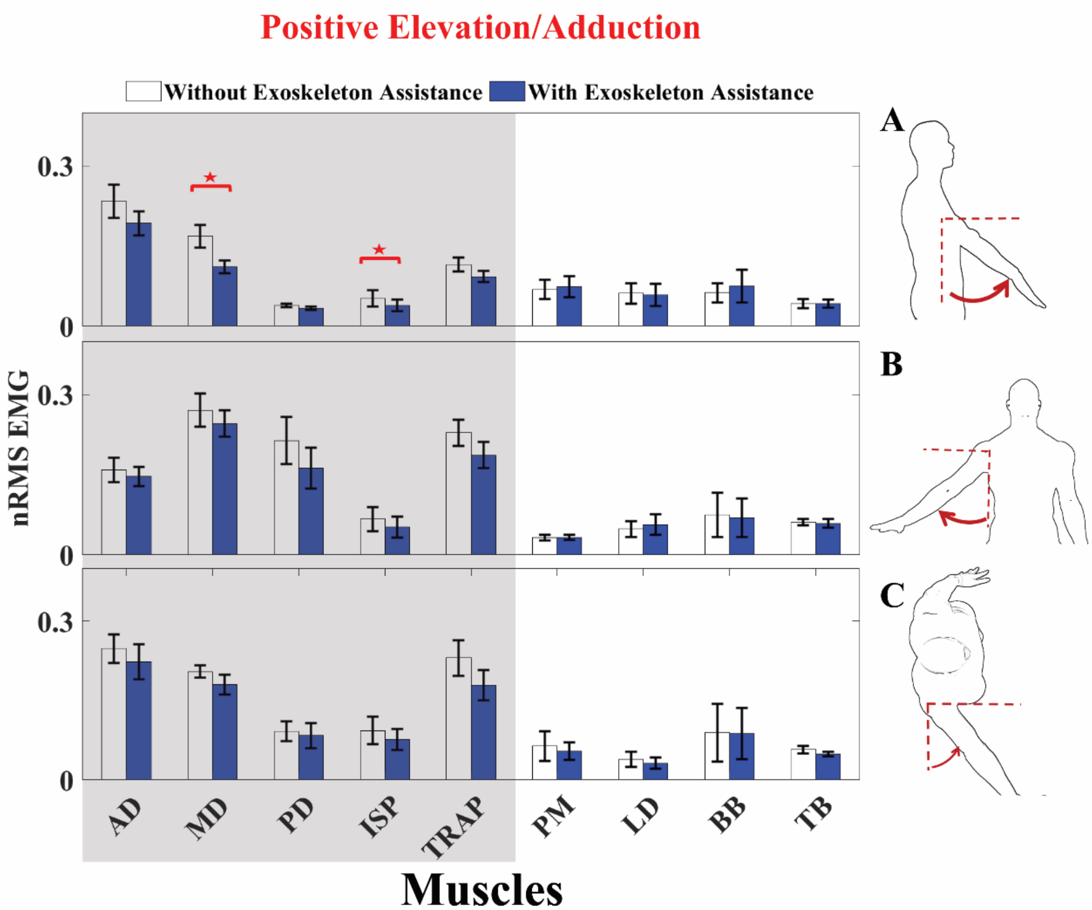

Figure 2-13. Root mean square of the normalized EMG (nRMS EMG) of several muscles crossing the shoulder during positive shoulder elevation in the sagittal plane (A), shoulder elevation in the frontal plane (B), and horizontal adduction (C) with and without exoskeleton assistance. Each bar shows the mean nRMS EMG across subjects. White and blue bars indicate trials without and with exoskeleton assistance, respectively. Error bars represent the standard error. * indicates statistically significant differences between trials with and without the exoskeleton. Shaded area shows muscles that primarily contribute force in the direction of positive shoulder elevation, based on their moment arms.

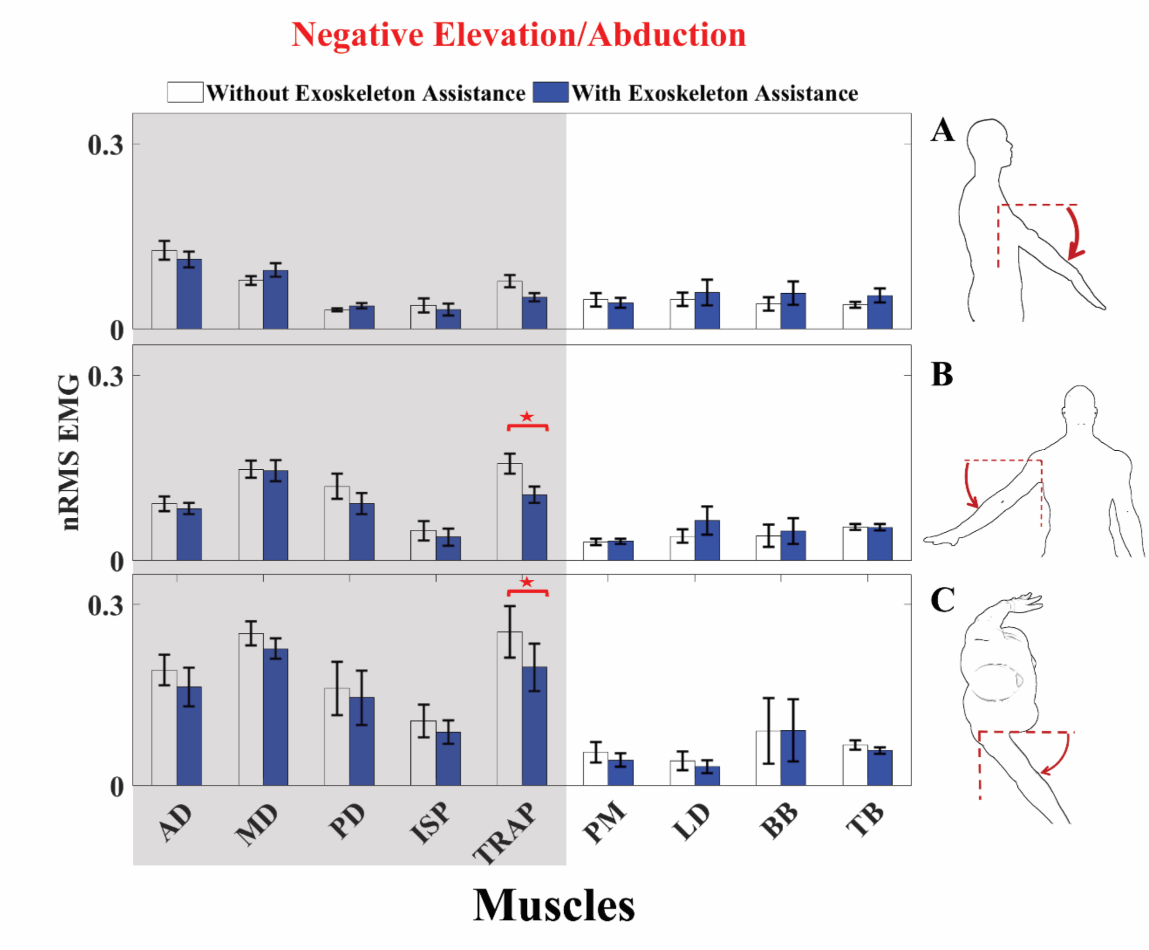

Figure 2-14. Root mean square of the normalized EMG (nRMS EMG) of several muscles crossing the shoulder during negative shoulder elevation in the sagittal plane (A), negative shoulder elevation in the frontal plane (B), and horizontal abduction (C) with and without exoskeleton assistance. Each bar shows the mean nRMS EMG across subjects. White and blue bars indicate trials without and with exoskeleton assistance, respectively. Error bars represent the standard error. * indicates statistically significant differences between trials with and without the exoskeleton. Shaded area shows muscles that primarily contribute force in the direction of positive shoulder elevation, based on their moment arms.

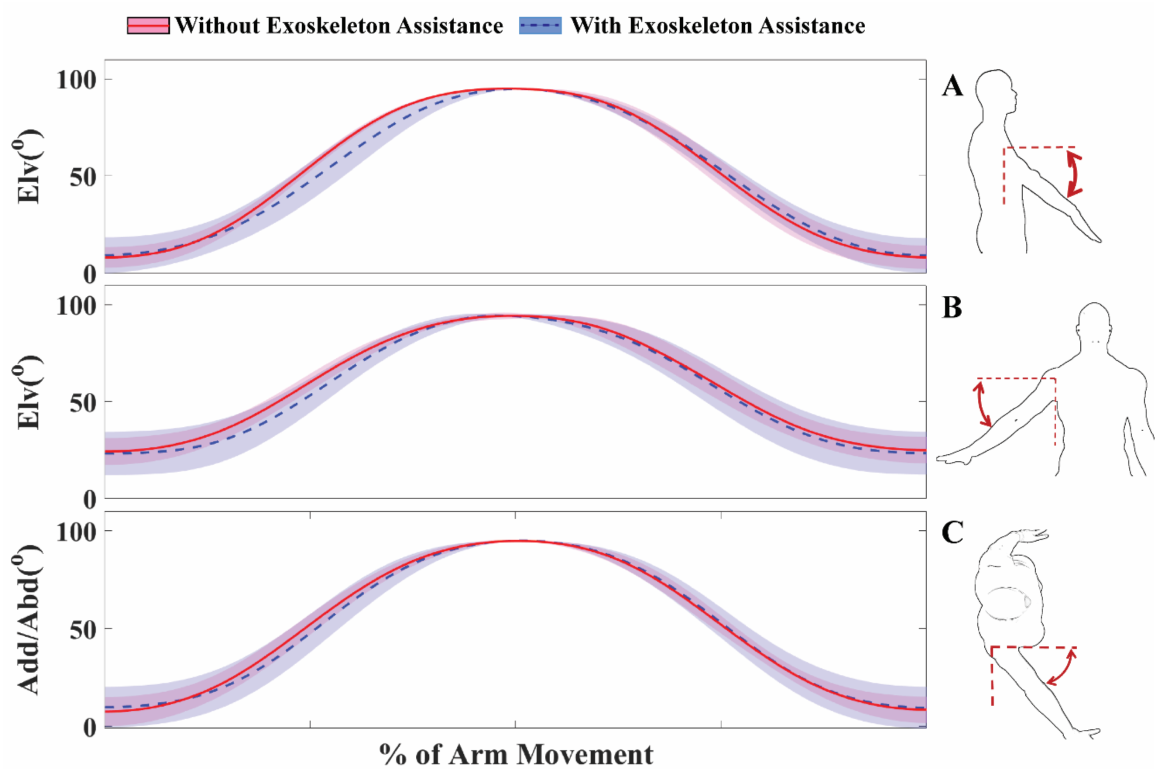

Figure 2-15. Mean of shoulder angular displacement and standard deviations (SD) during elevation in the sagittal plane (A), elevation in the frontal plane (B), and horizontal adduction/abduction (C) with and without exoskeleton assistance. The solid red curve and purple shadow show the mean and ±SD of dominant angular displacement across subjects for trials without exoskeleton. The blue dashed curve and blue shadow show the mean and ±SD of dominant angular displacement across subjects for trials with exoskeleton.

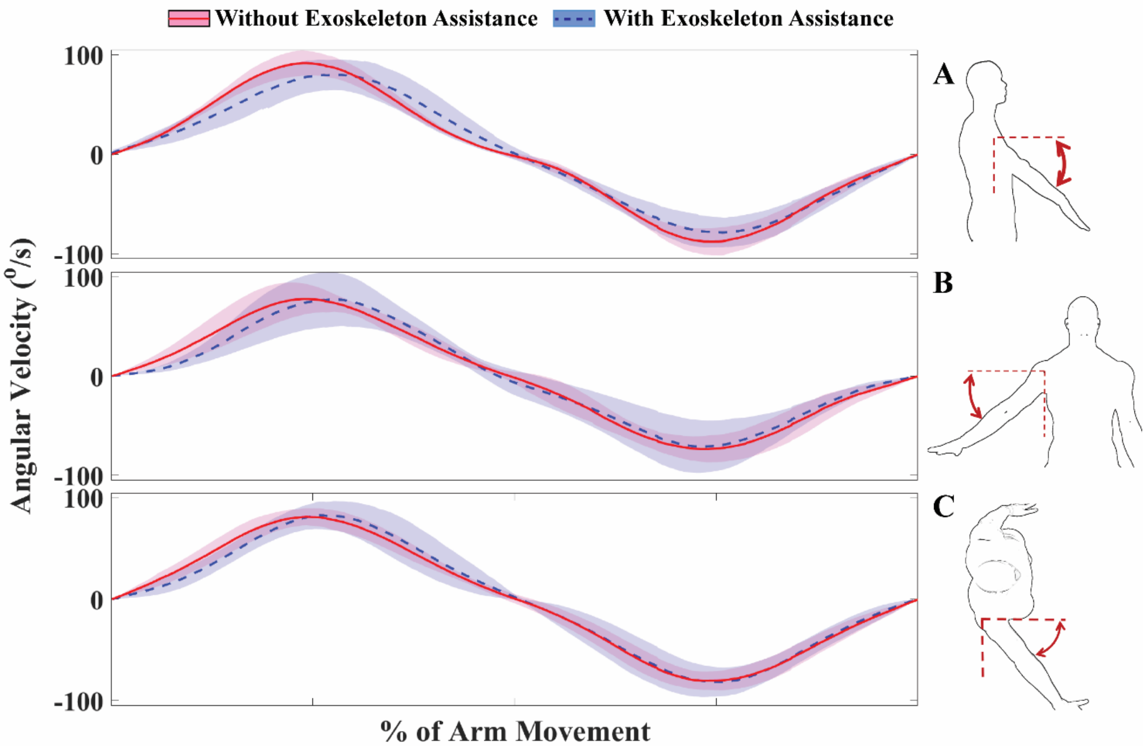

Figure 2-16. Mean of shoulder angular velocity and standard deviations (SD) during elevation in the sagittal plane (A), elevation in the frontal plane (B), and horizontal adduction/abduction (C) with and without exoskeleton assistance. The solid red curve and purple shadow show the mean and ±SD of dominant angular velocity across subjects for trials without exoskeleton. The blue dashed curve and blue shadow show the mean and ±SD of dominant angular velocity across subjects for trials with exoskeleton.

assists the shoulder in the direction of positive shoulder elevation based on the configuration of a force transmission cable.

The customized assistance is made possible specifically by the variable-radius cam, which acts as a gearing mechanism to modulate the force output of the spring. Cams are excellent design features that modulate force according to their shape. Thus, cams have been used in other passive mechanisms, including gravity-compensating arm supports that need to be mounted on walls or rigid frames, such as tables or wheelchairs [48]. Customizable assistance is an essential feature of exoskeletons since assistance requirements vary (1) across users as a function of their anthropometry and functional ability level and (2) across applications and tasks.

For both the spring-cam-wheel module and the WPCSE, the moment measured during the mechanical performance evaluation was larger during negative shoulder elevation (i.e., as the spring was being stretched) than during positive shoulder elevation (i.e., as the spring recoiled). We suspect that this so-called hysteresis behavior was primarily due to friction, for instance, at bearings and between the cables and components they wrap around. Inefficiency in the energy storage and return within the spring itself, inherent in all elastic springs, is another potential source of loss. The quantitative friction data from this study will be incorporated in our theoretical model so that it can be accounted for in future design iterations of our WPCSE prototype.

The hysteresis effect was more dramatic (i.e., more than 2x larger) with the WPCSE, which included the Bowden cable, than with the spring-cam-wheel module alone. Bowden cables are advantageous in wearable robotics applications in terms of design flexibility and remote actuation. However, Bowden cables introduce considerable friction [74] and appeared to be the main cause for the hysteresis behavior in the WPCSE. This friction, which originates from the contact between the inner wire and outer casing of the Bowden cable, is considered to be a nonlinear function of multiple geometric and material properties [75]. In the design of the WPCSE, we tried to minimize the Bowden cable friction by (1) fixing the cable's routing path using self-aligning spherical bearings and (2) placing the bearings so that the cable followed the most direct and shortest path from the spring-cam-wheel module to the shoulder and arm cuff. For future WPCSE design iterations, we will explore other Bowden cable configurations and alternative force transmission methods to reduce friction.

Promisingly, while only compensating for one-fourth of the gravity moment, the WPCSE showed a trend of reducing the root mean square (ranging from 9% to 33%) normalized EMG of several muscles crossing the shoulder consistently across the subjects. Reductions in muscle activity were mostly consistent across the subjects for the deltoid and rotator cuff muscles, which play major roles in compensating for gravity and stabilizing the glenohumeral joint during shoulder movements [76]. Our results are consistent with several previous studies that also showed that varying levels of gravity compensation at the shoulder can reduce muscle activity [52, 53, 77, 78]. The results of our pilot study justify and will facilitate the design of a biomechanical study with greater statistical power (i.e., larger sample size) to rigorously validate the efficacy of the WPCSE in reducing the activity of muscles crossing the shoulder. To support clinical translation, it will also be important to identify what magnitude of muscle activity reductions are clinically meaningful; this likely depends on factors such as pathology (e.g., rotator cuff tear vs nerve injury) and treatment objective (e.g., improve motor function vs offload tissues).

Interestingly, during negative elevation/abduction movements, the WPCSE tended to reduce the activity of the anterior deltoid, posterior deltoid, trapezius, and/or infraspinatus muscles across the subjects. This indicates that the participants were likely able to lower their arm using mostly gravity, even though the moment generated by the WPCSE during negative shoulder elevation was considerably higher than predicted by our theoretical model. This result, promisingly, contrasts with our previous computational study, which predicted higher activity in several muscles during negative shoulder elevation [65]. One possible explanation is that, during such movements, the WPCSE offloads muscles that contribute to positive shoulder elevation and are usually eccentrically contracted to control the shoulder’s angular descent. Additionally, participants may adapt their kinematics in subtle ways to avoid increasing muscle activity. We will test these hypotheses in a future, more comprehensive biomechanical study of the WPCSE.

The kinematic features of the tested movements were the same with and without exoskeleton assistance. With exoskeleton assistance, subjects could attain the lower and upper limits of movements and continuously move their arms between them, similar to the without-assistance condition. This suggests that the WPCSE did not constrain or impede subjects’ motions during the tested movements; this was supported by verbal feedback from the subjects as well. The shape of the angular velocity profile was similar between with and without exoskeleton conditions. However, subjects seemed to have more spatial and temporal variation throughout the tested movements with exoskeleton assistance, as indicated by the wider shadows for the angular displacement (Figure 2-15) and velocity (Figure 2-16). The slower movements may be due to subjects having no prior experience with the exoskeleton; in future studies, we will test the effect of experience (i.e., time of use) on kinematics.

The level of mechanical assistance generated by the WPCSE is expected to strongly influence neuromuscular activity, joint loads, and motor function at the shoulder. A desirable level of assistance would be one that both maximally assists and minimally resists user-generated moments. For example, though a high level of gravity compensation at the shoulder would maximally assist positive shoulder elevation movements, it might also require the user to generate higher negative shoulder elevation moments to overcome the gravity compensation and lower the arm. More research is needed to investigate the relationship between exoskeleton assistance level and biomechanical performance, which will inform the future design and prescription of wearable passive shoulder exoskeletons.

We chose to compare biomechanics with and without exoskeleton assistance, rather than with and without the exoskeleton, for two main reasons. First, the chosen comparison controlled for any effect that simply wearing the exoskeleton components (independent of the assistance force) may have on biomechanics. Second, the chosen comparison permitted a more rigorous study design; since subjects wore the exoskeleton for both assistance conditions, we could more easily and reliably randomize the order of trials of each condition while reducing within-condition variability (e.g., variation in exoskeleton placement due to repeated don/doff of the device). Since the without-assistance condition may not represent the subject’s normal “free” movement, it will be important to include a without-exoskeleton condition in future biomechanics studies of the WPCSE.

The WPCSE prototype and study had some notable limitations. First, as with most other passive shoulder exoskeletons, our WPCSE was designed to support the shoulder when the torso is upright and aligned with gravity; when the torso is flexed or extended, the exoskeleton and gravity moments will not be aligned, and the user may not be able to rely on gravity alone to counteract the exoskeleton moment. Second, as it was a prototype, the tested WPCSE likely requires further refinement before it can be used clinically. For example, the prototype did not include fail-safe or adjustment features that would allow a patient to deactivate or adjust the assistive force. Additionally, the Bowden cable, because of the way it was routed over the shoulder, contacted the skin during parts of the movement, which could be uncomfortable; we will explore different routing geometries and skin padding in future prototypes to avoid direct cable-skin contact. Third, our study of biomechanics was limited to able-bodied subjects. Testing in a patient population will be essential for demonstrating device safety and efficacy to support clinical use. However, patients with shoulder disability may have underlying tissue injuries, muscle coordination patterns, or other conditions that could put them at increased risk for injury or re-injury when using a novel, untested device prototype. Thus, testing the exoskeleton on able-bodied subjects first provided valuable data that will inform how the prototype can be (1) tested safely on people with shoulder disability, and (2) refined to make it safer and more effective. The data also support our hypothesis, which we will test in our follow-up study, that the exoskeleton can reduce muscle activity in patients with shoulder disability. Other studies have similarly reported results from able-bodied subjects only when testing early-stage prototypes of assistive devices [79, 80]. Finally, our human subjects experiment included only three one-degree-of-freedom movements and eight subjects; as with testing in a patient population, larger and more comprehensive studies of biomechanics and other clinically relevant outcomes [81] will be needed to support clinical translation.

Conclusion

To address an unmet clinical need for movement assistance at the shoulder, we presented the design of a WPCSE based on a novel spring-cam-wheel module. As a first step toward clinical translation, we preliminarily evaluated the mechanical and biomechanical performance of our WPCSE prototype. Our results showed that the WPCSE, compensating for a modest one-fourth of the gravity moment at the shoulder, tended to reduce the activity of several muscles crossing the shoulder, including the deltoid and rotator cuff muscles. However, our mechanical evaluation revealed aspects of the design that limit the assistance that the WPCSE could provide. In our future work, we will test different WPCSE assistance levels and identify a range of assistance that most enhances shoulder motor function and biomechanics without impeding movements. More comprehensive biomechanical studies will be performed to assess the WPCSE for more biomechanical parameters (e.g., range of motion and endpoint/hand kinematics), more participants (both able-bodied subjects and people with shoulder disability), and more movements that typify activities of daily living. Finally, several design refinements, especially those that reduce friction in the system, will be explored.

Acknowledgements

This study was supported by start-up funds from the Department of Mechanical, Aerospace and Biomedical Engineering at the University of Tennessee. The authors thank Vulcan Spring & Manufacturing for providing the constant-torque springs.

CHAPTER 3 : IDENTIFYING AN OPTIMAL ANTI-GRAVITY ASSISTANCE LEVEL FOR SELECT FUNCTIONAL SHOULDER MOVEMENTS: A SIMULATION STUDY

Abstract

The level of assistance torque (i.e., mechanical assistance) is one key design parameter for passive shoulder exoskeletons. High assistance levels may perturb arm movements, while low assistance may not provide functional benefits. The objective of this study was to use computational tools to identify an optimal anti-gravity assistance level for passive shoulder exoskeletons.

We used the task space framework to perform biomechanical simulations of arm movements in OpenSim (Stanford, CA, USA). The simulated movements, which mimicked functional tasks, included shoulder elevation and lowering movements in frontal and scapular planes, as well as forward and lateral reaching movements. These movements were simulated across a range of assistance torque levels from 0% (no-assistance) to 100% of the maximum shoulder gravity torque, in increments of 10%. Muscle activations and bone-on-bone joint contact forces at the glenohumeral joint were estimated using static optimization and joint reaction analysis, respectively. The optimal assistance level was identified based on analysis of hand kinematics, muscular response efficiency, and glenohumeral joint stability.

As the assistance level increased from 10% to 40%, the variability of hand movements nearly doubled, and this trend continued for higher assistance levels. The total muscle effort rate was minimized at an assistance level ranging from 20% to 30%. While the stability of the glenohumeral joint was mostly maintained across assistance levels, it decreased slightly at higher assistance levels. The results of this study indicated that, for the simulated movements, an optimal assistance level lies within the range of 20-30% of the maximum gravity torque at the shoulder joint. Assistance levels above 40% could cause undesired effects such as greater variability of end-limb kinematics, reduced muscular efficiency, and compromised glenohumeral joint stability.

Introduction

Arm weight compensation has been the design paradigm for many powered and passive (i.e., unpowered) shoulder exoskeletons developed for medical rehabilitation [82-86] and movement assistance/support [36, 38, 87]. The shoulder gravity torque generated by the mass of the distal limb segments is much greater than inertial torques during daily activities [17]. This is especially the case for patients with neurological and orthopedic shoulder disability who move their arm at lower speeds than healthy people. Weight compensation of the upper extremity can enhance motor function and extend the reaching workspace for such patients [52, 88, 89]. Thus, many end-effector robots [19, 88, 89], cable-driven manipulators [90] and exoskeletons [22, 91-93] for clinical applications function as gravity compensators. Gravity compensating exoskeletons have been also developed for motion augmentation and assistance during occupational tasks (e.g., overhead activities or manual handling) [36, 38, 87, 94]. Occupational exoskeletons physically aid workers during high-demanding tasks and reduce the risk of work-related injuries by removing excessive musculoskeletal strains and fatigue [38, 95].

Powered upper limb exoskeletons can provide transparent, feedback-controlled, gravity balance in any arm posture [88, 89, 96]. Thanks to the advanced design mechanisms, embedded position/force sensors, and control strategies, powered exoskeletons can provide decoupled, full-arm balance in any pose and trajectory without restricting other degrees of freedom of the arm. However, achieving such flexible gravity-compensating capacity comes with trade-offs, such as high weight, obstruse design, and high maintenance cost, which limit the wearability and portability of powered exoskeletons. These disadvantages have recently given rise to the development of passive exoskeletons as an attractive solution for providing continuous, portable gravity compensation to assist or support arm movements [27, 36, 64, 82, 87].

Passive exoskeletons mainly consist of energy-shuffling mechanisms in which counterweights and/or elastic elements (e.g., mechanical springs and rubber bands) store mechanical energy during specific movement phases and return it during others [87, 97]. Counterweights are avoided for wearable devices since they increase the overall weight of the device. Manufacturing mechanical springs with zero free length or specific force-displacement profiles is also costly [98]. Therefore, multi-linkage [87], parallelogram- [26, 98], pulley- [36], and cam-based [82] mechanisms have been used to modulate the force output of off-the-shelf, non-zero free length springs and, thus, tune the assistance level as desired. Depending on the targeted end user, these mechanisms can help to produce arm balance [26, 98] at certain angles or modulated bionic assistive torque across the range of arm elevation [38, 82, 87].

The assistance level is a crucial design parameter for passive shoulder exoskeletons. However, there is no consensus on what assistance level is most beneficial to the user [36]. A study of the ShoulderX exoskeleton [37] reported up to 80% reduction in activation of the anterior deltoid and upper trapezius muscles with an assistive torque ranging from 8.5 to 20.0 Nm. In an experimental evaluation of the Proto-MATE [38] with an assistive torque equal to 50% of the estimated gravity torque (i.e., up to 5.5 Nm), activations of the shoulder flexor muscles were reduced by up to 43%. Rossini *et. al.* [36] also reported up to 22% reduced activation of shoulder flexor muscles when the Exo4Work shoulder exoskeleton delivered 3 Nm assistive torque. However, in a study with able-bodied subjects, Asgari et. al. reported that users experienced discomfort [64] and greater muscle activity during arm lowering movements when a wearable passive shoulder exoskeleton compensated for 50% of the shoulder gravity torque [82]. Some studies also suggest that an optimal level of assistance might be task dependent [28].

Increasing assistance level can substantially reduce the activity of the muscles responsible for positive shoulder elevation/flexion against gravity. However, too much assistance can be associated with undesirable effects such as higher levels of activation in antagonist muscles [37, 39, 40], compromised joint stability and stiffness [65, 99], and altered joint kinematics and end-point precision [100]. Studies of occupational exoskeletons reported that, during overhead reaching tasks, the activity of shoulder flexor muscles (e.g., deltoids, trapezius) was less, while the activity of antagonist muscles (e.g., triceps and latissimus dorsi) was greater, with the exoskeletons than without [37, 40]. When faced with external assistive forces or perturbations, the neuromuscular system stabilizes the upper body joints and end-limb by modulating the magnitude and patterns of activations of agonist-antagonist muscle pairs [101, 102]; this has important implications for joint stiffness and stability. Specifically, over-assistance could compromise agonist-antagonist muscle coordination and joint and end-limb stability [103, 104], resulting in higher muscle activations and reduced task performance and precision for the wearer [39].

The main objective of this simulation-based sensitivity study was to determine the effect of anti-gravity assistance level at the shoulder on (1) muscular response efficiency and (2) stability at the joint and end-limb. Our hypothesis was that there exists an optimal assistance level, above which may degrade GH joint stability or task performance, and below which may provide less improvement in muscular efficiency.

Our overall approach was, using a task space (i.e., operational space) framework, to perform predictive biomechanical simulations of selected arm reaching and elevation movements; simulations were performed for eleven different anti-gravity assistance levels ranging from no assistance (0%) to 100% of the maximum gravity torque at the shoulder, in increments of 10%.

Methods

The musculoskeletal model

For our musculoskeletal simulations, we used an existing upper limb musculoskeletal model [105] implemented in OpenSim (version 4.1) [106]. The upper extremity model includes 7 degrees of freedom (DOFs), with sets of three, two, and two DOFs describing the shoulder, elbow, and wrist kinematics, respectively. The skeletal geometry of the model is defined based on the anthropometric data of a 50th percentile male. The model is actuated by fifty Hill-type muscle-tendon units crossing shoulder, elbow, and wrist joints.

The task space framework

The task space framework is a model-based control approach to track a desired trajectory defined in the task coordinate system [107-113]. Unlike the joint coordinate systems, the task coordinate system is directly attached to the end-effector whose motion and contact forces describe the performed task. Therefore, developing the equations of motion in the task coordinate system simplifies the control problem by abstracting away the generalized coordinates in the joint space. The task space controller incorporates a dynamic model of the control plant to directly estimate the joint torques that are required to execute a dexterous and compliant tracking motion (i.e., task). This control strategy resembles the way humans control their upper limb motion where the central nervous system (CNS) acts as a high-level controller and executes goal-oriented hand movements. Among different task space controllers designed for over-actuated systems (i.e., redundant), Khatib's [107, 114] approach appealing as it decouples the dynamics of the task from that of the null space (i.e., posture). This approach is well-suited for musculoskeletal models, such as the upper limb model used in this study, in which the number of DOFs, n, is larger than the task dimension, m [114, 115]. Since musculoskeletal models are also subject to different constraints $\Phi(q) = \mathbf{0}$

(e.g., holonomic), we used an orthogonal projection scheme, proposed by Aghili [116, 117], to firstly eliminate the constraint forces by projecting the plant dynamics onto the constraints' manifold.

The joint-space equation of motion (EOM) for the upper limb with n DOF and k linearly independent constraints, whose generalized coordinate vector is $\boldsymbol{q} \in \mathbb{R}^n$, can be written as [111]:

$$M(\boldsymbol{q})\ddot{\boldsymbol{q}} + h(\boldsymbol{q}, \dot{\boldsymbol{q}}) + \boldsymbol{\tau}_{ext} = B\boldsymbol{\tau} + J_C^T(\boldsymbol{q})\lambda \tag{1}$$

where $M(\boldsymbol{q}) \in \mathbb{R}^{n\times n}$ is the mass matrix; $h(\boldsymbol{q}, \dot{\boldsymbol{q}}) \in \mathbb{R}^n$ includes gravity, centripetal, and Coriolis forces; $\boldsymbol{\tau}_{ext} \in \mathbb{R}^n$ is the vector of externally imposed forces/torques; $\boldsymbol{\tau} \in \mathbb{R}^n$ is the vector of generalized forces; $B = diag(b_1, \dots, b_n)$ with $b_i = 1$ for actuated coordinates and $b_i = 0$ for passive coordinates; $J_C^T(\boldsymbol{q})$ is the transpose of the constraint Jacobian; and $\lambda \in \mathbb{R}^k$ shows the constraint forces. For the sake of brevity, we replace $M(\boldsymbol{q})$ by M, $h(\boldsymbol{q}, \dot{\boldsymbol{q}})$ by h from this point forward.

To eliminate the constraint forces form (1), we multiply both sides by an orthogonal projection operator P (P is orthogonal if $P = P^2 = P^T$) to obtain the projected EOM [113, 116]:

$$PM\ddot{\boldsymbol{q}} + P(h + \boldsymbol{\tau}_{ext}) = P\boldsymbol{\tau} \tag{2}$$

Since $PJ_C^T = 0$, we can obtain $P = I - J_C^+ J_C$, where J_C^+ is the Moore-Penrose pseudoinverse of the constraint Jacobian J_C. We can conclude from the first differentiation of the k constraint $J_C\dot{\boldsymbol{q}} = 0$ that the vector of generalized velocity lies in the null space of the constraint Jacobian matrix [116]. This concludes:

$$(I - P)\dot{\boldsymbol{q}} = 0 \tag{3}$$

Differentiating form (3):

$$(I - P)\ddot{\boldsymbol{q}} - C\dot{\boldsymbol{q}} = 0 \tag{4}$$

and $C = \left(\frac{d}{dt}\right)P$ and can be obtained as $C = -J_C^+ \dot{J}_C$. Substituting (4) in (2) gives:

$$PMP\ddot{\boldsymbol{q}} + P(h - MC\dot{\boldsymbol{q}} + \boldsymbol{\tau}_{ext}) = P\boldsymbol{\tau} \tag{5}$$

Multiplying (4) by $(I - P)M$ and adding it to (5) yields:

$$M_c\ddot{\boldsymbol{q}} + P(h + \boldsymbol{\tau}_{ext}) - C_c\dot{\boldsymbol{q}} = P\boldsymbol{\tau} \tag{6}$$

where $M_c = PMP + (I-P)M(I-P)$, and $C_c = (I-2P)MC$. Unlike the PM term in (2), M_c is always invertible and symmetric, preserving the physical characteristics of the inertia matrix M [116]. To map the projected joint-space EOM onto the task space, we multiply (6) by JM_C^{-1} and substitute $J\ddot{\boldsymbol{q}}$ with $\ddot{\boldsymbol{x}} - \dot{J}\dot{\boldsymbol{q}}$ [107, 111]. Note that every task $\boldsymbol{x} \in \mathbb{R}^m$ with m DOFs can be related to the generalized coordinates by the task Jacobian $\dot{\boldsymbol{x}} = J(\boldsymbol{q})\dot{\boldsymbol{q}}$.

$$\ddot{\boldsymbol{x}} - \dot{J}\dot{\boldsymbol{q}} + JM_C^{-1}P(h + \boldsymbol{\tau}_{ext}) - JM_C^{-1}C_c\dot{\boldsymbol{q}} = JM_C^{-1}P\boldsymbol{\tau} \tag{7}$$

The joint-space generalized forces, $\boldsymbol{\tau}$, can also be similarly mapped onto the task space forces, $\boldsymbol{F}$, via $\boldsymbol{\tau} = J^T\boldsymbol{F}$. Thus, the EOM can be defined in the task space:

$$\Lambda_c\ddot{\boldsymbol{x}} + \Lambda_c JM_C^{-1}P(h + \boldsymbol{\tau}_{ext}) - \Lambda_c JM_C^{-1}C_c\dot{\boldsymbol{q}} = \boldsymbol{F} \tag{8}$$

where $\Lambda_c = (JM_C^{-1}PJ^T)^{-1}$ and is called a constraint-compliant inertia matrix. In the case where $\boldsymbol{\tau}_{ext}$ is available, as outlined by Khatib [107], the controller law can be modeled as:

$$\boldsymbol{\tau} = J^T\boldsymbol{F} + \left(I - J^T J^{T^\#}\right)\boldsymbol{\tau}_{\boldsymbol{p}} \tag{9}$$

where $J^{T^\#} = (JM_C^{-1}PJ^T)^{-1}JM_C^{-1}P$, and $\boldsymbol{\tau}_{\boldsymbol{p}} \in \mathbb{R}^n$ is the posture vector defining the joint impedance behavior. $J^{T^\#}$ guarantees the decoupling of the task space from the posture space (i.e., the null space). In equation (9), $\boldsymbol{F}$ can be computed from (8) based on a command task acceleration $\ddot{\boldsymbol{x}}_{\boldsymbol{d}}$ that defines the desired trajectory for the end-limb [107, 111, 112]:

$$\ddot{\boldsymbol{x}} - \ddot{\boldsymbol{x}}_{\boldsymbol{d}} + k_d(\dot{\boldsymbol{x}} - \dot{\boldsymbol{x}}_{\boldsymbol{d}}) + k_p(\boldsymbol{x} - \boldsymbol{x}_{\boldsymbol{d}}) = 0 \tag{10}$$

where k_d and k_p are positive-definitive gain matrices and $\boldsymbol{x} = \boldsymbol{f}(\boldsymbol{q})$ is the forward kinematics tracking trajectory (Figure 3-1). In a similar way, $\boldsymbol{\tau}_{\boldsymbol{p}}$ can be estimated via a command joint acceleration $\ddot{\boldsymbol{q}}_{\boldsymbol{d}}$ that defines the impedance behavior in the null space [118]:

$$\boldsymbol{\tau}_{\boldsymbol{p}} = \ddot{\boldsymbol{q}} - \ddot{\boldsymbol{q}}_{\boldsymbol{d}} + K_d(\dot{\boldsymbol{q}} - \dot{\boldsymbol{q}}_{\boldsymbol{d}}) + K_p(\boldsymbol{q} - \boldsymbol{q}_{\boldsymbol{d}}) - \boldsymbol{\tau}_{ext} \tag{11}$$

K_d and K_p are positive-definitive matrices representing, in turn, the damping and stiffness.

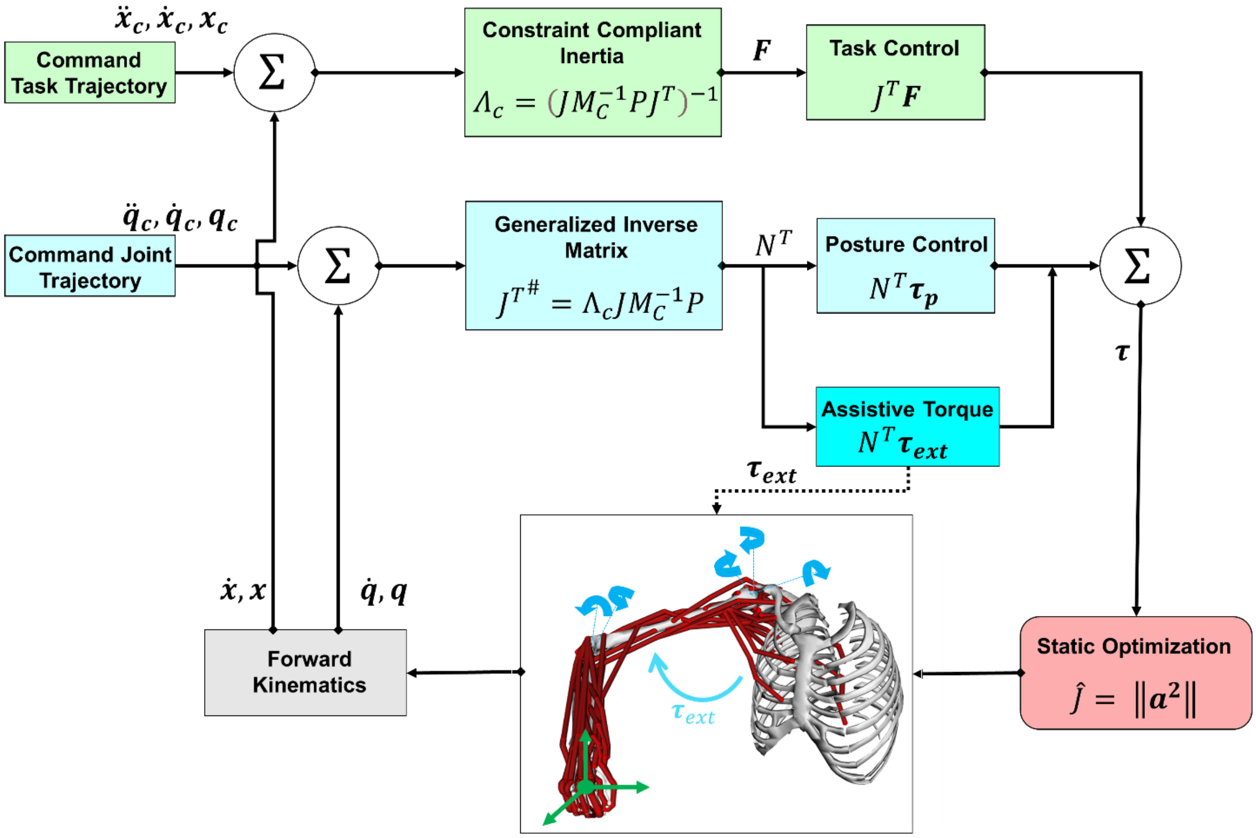

Figure 3-1. A task/posture space upper limb controller with static optimization to estimate muscle activations.

Estimation of muscles activation

We used static optimization (SO) to address the muscle redundancy problem [115, 119]. SO estimates the optimal muscle activations a_i such that muscle forces produce the generalized torques specified by the task space controller, i.e., equation (9), while minimizing the following performance criterion:

$$\hat{J} = \sum_{i=1}^{n_m} a_i^2$$

subject to: (12)

$$\tau_j = \sum_{i=1}^{n_m} r_{i,j} F_{mt,i}\ ,$$

$$0 \leq a_i \leq 1 \ \forall\ i \in \{1, 2, \dots, n_m\}.$$

where $r_{i,j}$ is the moment arm of muscle i about the axis joint j, and $F_{mt,i}$ represents the force generated by the musculotendon unit i. We assumed a linear relationship between muscle activation and muscle force and ignored the muscle activation and contraction dynamics.

$$F_{mt,i} = a_i F_{mt,i}^{max}(\boldsymbol{q}, \dot{\boldsymbol{q}}) \tag{13}$$

$F_{mt,i}^{max}(\boldsymbol{q}, \dot{\boldsymbol{q}})$ represents the maximum force generating capacity for the i^{th} muscle estimated based on the instantaneous generalized coordinates and speeds [119, 120].

Simulations

The presented task space framework was used to execute predictive upper limb movement simulations with eleven levels of assistance at the shoulder joint for select functional tasks. The targeted assistance levels k are no-assistance (k=0) and 10, 20, 30, 40, 50, 60, 70, 80, 90, and 100, with k being a percentage of the maximum gravity torque at the shoulder. Using the upper limb model, we estimated the maximum gravity torque in the frontal plane with a fully extended elbow and 90-degree arm elevation as following:

$$\tau_G^{ma}(\alpha) = 12.9 \ \sin(\alpha) \ \text{(Nm)} \tag{14}$$

where $\tau_G(\alpha)$ is the gravity torque and α is the shoulder elevation angle [64, 82, 105]. For simplification, we used an idealized coordinate actuator to model the external assistive torque in the positive direction of the shoulder elevation coordinate. The assistive torque was modeled by the following equation:

$$\tau_{ext}(\alpha) = \frac{k}{100}\tau_{G}^{ma}(\alpha) \tag{15}$$

The select functional tasks included shoulder elevation and lowering movements in two different planes of elevation and reaching movements to four target positions (Figure 3-2). We selected these reaching and elevation movements as they are clinically significant and involve complex coordination of multiple upper joints [121]. Furthermore, these motions require positive/negative elevation, which is a significant movement of the shoulder during daily activities[122].

The shoulder elevation movements were simulated in the coronal (i.e., plane of elevation 0º, Figure 3-2(A)), and scapular planes (i.e., plane of elevation 30º, Figure 3-2-2(B)) for the two targets, one placed at shoulder height and one above shoulder height. The target positions during elevation were selected such that they can be reached with the elbow extended. For the lateral (Figure 3-2 (C)) and forward reaching (Figure 3-2 (D)) movements, the hand moved from an initial position alongside the body to target positions in front of the model at above shoulder- and shoulder-height levels. For the forward reaching movements, the above-shoulder target was located 25 cm superior and 45 cm anterior to the GH joint center, and shoulder-height target was located 50 cm anterior and at the same height as GH joint center. For the lateral reaching movements, the targets were shifted 15 cm lateral to the GH joint.

The movement planning for the simulated functional tasks was encoded based on equation (10), where the hand's center of mass (i.e., end-limb) tracks the desired positional trajectory kinematics with three DOFs as the command input. We locked the wrist joint during all the simulations while the other five DOFs were set free, guaranteeing kinematic redundancy. Table 3-1 includes the initial angles as well as the lock/unlock status of the model's DOFs during the simulated movements.

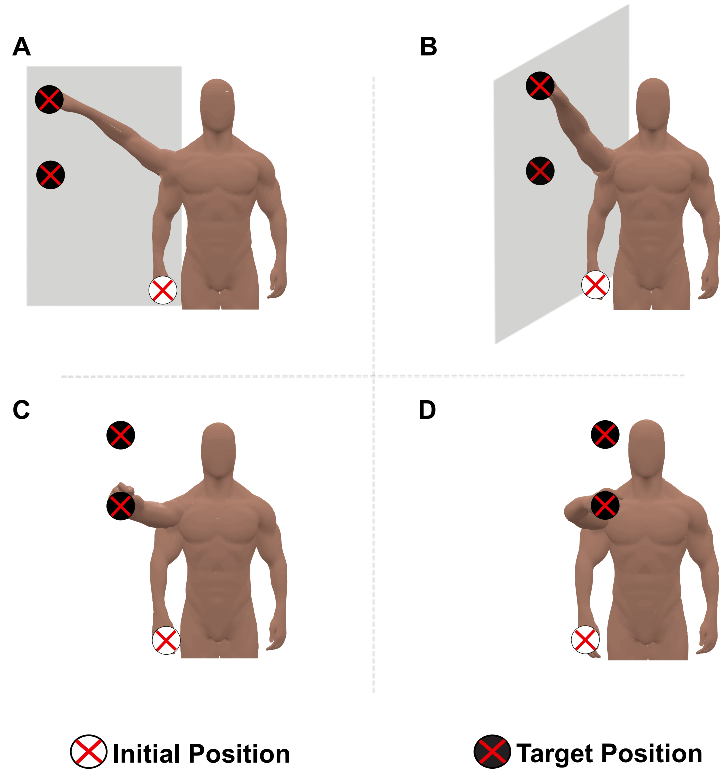

Figure 3-2. Select functional shoulder movements. Shoulder elevation in the coronal plane (A), and scapular plane (B), lateral reaching (C), and forward reaching (D) movements. Simulations were performed at two targets positions for each of the above movements. For the elevation movements, targets were placed at the shoulder height and above shoulder height such that they can be reached by fully extended elbow. For the lateral and forward reaching movements, targets were closer to the body and can be reached with flexed elbow.

Table 3-1 Initial angles and the joint lock/unlock status for the simulated functional tasks.

Functional tasks		Initial angles													
		Plane of Elevation		Elevation		Shoulder Rotation		Elbow Flexion		Elbow Supination		Wrist Flexion		Wrist Deviation	
		Deg	Lock	Deg	Lock	Deg	Lock	Deg	Lock	Deg	Lock	Deg	Lock	Deg	Lock
Coronal Elevation	Shoulder-height Above Shoulder	0	🔓	30	🔓	0	🔓	30	🔓	0	🔓	0	🔒	0	🔒
Scapular Elevation	Shoulder-height Above Shoulder	30	🔓	30	🔓	30	🔓	30	🔓	0	🔓	0	🔒	0	🔒
Lateral Reaching	Shoulder-height Above Shoulder	60	🔓	30	🔓	30	🔓	30	🔓	0	🔓	0	🔒	0	🔒
Forward Reaching	Shoulder-height Above Shoulder	80	🔓	30	🔓	0	🔓	30	🔓	0	🔓	0	🔒	0	🔒

The hand's desired trajectory was decoded based on a fifth-order polynomial function to minimize jerk between the initial and target positions [123, 124]. Such a function also produces bell-shaped velocity profiles that are commonly observed for voluntary point-to-point arm movements. The derivative and proportional gain matrices were set to $k_p = 100$ and $k_d = 20$. We did not consider a command joint acceleration for the null space control as in equation (11) and set $\boldsymbol{\tau}_p = K_d \dot{q} - \boldsymbol{\tau}_{ext}$ with $K_d = -0.25$. The external torque $\boldsymbol{\tau}_{ext}$ is the modeled gravity-compensating assistive torque, which was estimated using equation (15). Each of the select functional tasks consists of advancement and retreat phases. During the advancement phase, the hand moves from its initial position to a target position while during the retreat phase it returns to the initial position. The duration of each simulated task was estimated by dividing the hand-to-target distance over the mean target-approaching velocity for the able-bodied participants reported in [121]. The advancement and retract phases had the same execution time, with a 500-millisecond interval between them when the hand was held at the target.

Data analysis

Hand Kinematics

The proposed task-posture controller assumes that the control of the assistive torque takes place in the posture space (i.e., null space) of the task, where the acceleration generated by the assistive torque should not interfere with the acceleration of the hand positional task. Thus, we tracked the position of the hand's center-of-mass (COM) in 3-dimensional (3-D) space during the simulations. Then, for each assistance level, we calculated the variability in hand position across the eight simulated tasks. To calculate the hand position variability, we resampled the simulations with different assistance levels to the same number of points for every task, and used following equation:

$$\text{Position Variability} = \frac{1}{n}\sum_{i=1}^{n}\left\|\boldsymbol{x}_{k,i} - \boldsymbol{x}_{0,i}\right\|_2 \tag{16}$$

where k and i represent the assistance level and resampled point number, respectively. n is the total number of resampled points for every task, and 0 subscript stands for the no-assistance level simulations. $\| \|_2$ shows the Euclidean norm. It is expected that the hand position variability should not increase for an optimal level of assistance.

Muscular Response Efficiency

During dynamic or quasi-static tasks, the involved muscles can have a load-bearing or fine-tuning contribution depending on whether they lengthen or shorten [103]. To compare the muscular activity across the assistance levels, we computed the total muscle effort rate and efficiency. The total muscle effort rate, $\dot{E}_{total}$, was defined as the sum of the individual muscle output calculated based on equation (17).

$$\dot{E}_{total} = \sum_{i=1}^{n_m} \frac{1}{T_f - T_s} \int_{T_s}^{T_f} {a_i}^2 dt \tag{17}$$

T_s and T_f are the start and finish times of each simulated task, a_i is the muscle activation estimated in (13), and n_m is the number of shoulder muscles. The included shoulder muscles were anterior, middle, posterior deltoids, supraspinatus, infraspinatus, subscapularis, teres major and minor, pectoralis major, latissimus dorsi, coracobrachialis, triceps brachii, and biceps brachii. To quantify the muscular response efficiency, we first categorized the shoulder muscles as being either agonist or antagonist during each phase of the simulated tasks based on whether their fiber length was shortening or lengthening. The categorization was performed for the no-assistance trials and assumed to stay the same across assistance levels. Our anticipation is that the gravity-compensating assistive torque will result in decreased activation of both agonist and antagonist muscles, as it aligns with the purpose of these muscles to generate torque in order to counteract the gravity force. However, the decreasing trend for the antagonist muscles is expected to be limited since they have a fine-tuning function to provide stiffness for the shoulder joint and decelerate the arm. Therefore, depending on the task type, with an optimal level of assistive torque, the synergistic function of agnostic-antagonist muscles is expected to be most efficient, indicated by a maximum reduction in their activations. Therefore, the efficiency was defined as:

$$\text{Efficiency} = \left| 1 - \frac{\dot{E}^{antag}}{\dot{E}_{total}} \right| * 100 = \left| \frac{\dot{E}^{agon}}{\dot{E}_{total}} \right| * 100 \tag{18}$$

where $\dot{E}^{antag}$ and $\dot{E}^{agon}$ are the total muscle effort rate for the antagonistic and agonistic shoulder muscles, respectively.

GH stability

We used the joint reaction analysis tool in OpenSim to estimate the GH joint contact forces [125, 126] during the simulated tasks. To determine the spatial orientation of the glenoid fossa, we placed extra markers around the center of the glenoid fossa in the musculoskeletal model and used their cartesian coordinates to construct a local cartesian coordinate system aligned with and centered at the glenoid rim. This enabled us to transform the estimated contact forces to the anatomical coordinate system of the glenoid fossa (Figure 3-3) at each time instant and compute the compressive and shear forces at the GH joint. The compressive component pushes the humeral head into the glenoid concavity while the shear components in the superior-inferior (SI) and anterior-posterior (AP) directions destabilize the joint by causing the humeral head to translate away from the center of the glenoid fossa [127]. In this study, we calculated the ratio of SI and AP shear forces to the compressive force as θ_{SI} and ϕ_{AP}, respectively, and quantified the GH joint stability as:

$$GH_{stability} = \left(\frac{\theta_{SI}}{\theta_{glenoid}}\right)^2 + \left(\frac{\phi_{AP}}{\Phi_{gelnoid}}\right)^2 \quad (19)$$

Equation (19) estimates the glenoid rim as an ellipse whose width and height are 28.4 mm in the AP direction and 36.6 mm in the SI direction, respectively [128]. $\theta_{glenoid}$ and $\Phi_{gelnoid}$ are the maximum angles that the GH joint contact force can have in the SI and AP direction, respectively. For $GH_{stability} > 1$, when the resultant GH joint contact force points outside of the glenoid rim, the GH joint is considered unstable; conversely, for $GH_{stability} < 1$, when the resultant GH joint contact force points within the glenoid rim, the GH joint is considered stable. The $GH_{stability}$ was calculated at each sampling point for all the tasks.

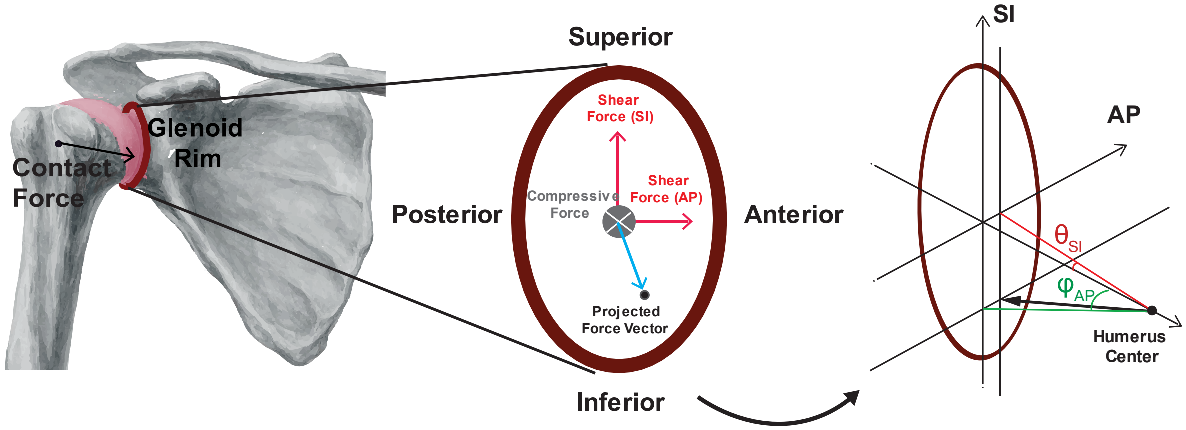

Figure 3-3. Glenohumeral joint stability. Contact forces at GH joint were transformed to the glenoid fossa, which is represented as an ellipse, and decomposed into compressive and shear forces in superior-inferior (SI) and anterior- posterior (AP) directions. The ratio of SI and AP shear forces to the compressive force were then calculated as θ_{SI} and ϕ_{AP} angles and used to determine the GH joint stability.

Results

Hand Kinematics

The level of assistance directly affected the variability of the hand position across the simulated tasks. Figure 3-4 shows an example of the components of the hand trajectory for coronal elevation to a target placed above shoulder-height for the no-assistance and 40% assistance trials. Across all tasks, as the assistance level increased from 10% to 40%, the hand variability almost doubled and surpassed 10 cm (Figure 3-5). The variability continued to increase beyond an assistance level of 40%, indicating dynamic instability for the hand in the simulated shoulder tasks. Dynamic instability can be defined as the inability of the upper limb model to closely track the desired hand trajectory resulting in lack of precision in task execution [129]. Figure 3-6 further highlights this instability, showing that the resultant hand COM trajectory deviates from the desired trajectory for assistance levels beyond 40%.

The model performed well in terms of following the desired trajectory during the acceleration phase at assistance levels below 50% (Figure 3-6). However, as the phase progressed to the deceleration part, there was an increasing deviation from the desired trajectory. At assistance levels of 50% and higher, the model exhibited higher divergence from the desired trajectory, resulting in an unstable hand trajectory for the entire simulation. It's worth noting that the initial position of the hand COM moved further away from the body when the assistance level was set at 50% and higher.

Muscular Response Efficiency

The simulation results confirmed that the level of assistance torque affects the total effort rate during simulated tasks. In general, an initial decrease in the total effort rate was observed as the level of assistance increased. However, the downward trend bottoms out within the 20%-30% range of assistance. A visual representation of this trend is presented by a heatmap, Figure 3-7. The row of the heatmap shows the scaled total effort rate across the assistance levels for each simulated task. As the assistance level increases beyond 30%, the total effort becomes larger. Notably, the lateral and forward reaching movements to the shoulder level target deviated from this trend, as their total effort rate increased when the assistance level exceeded 10%.

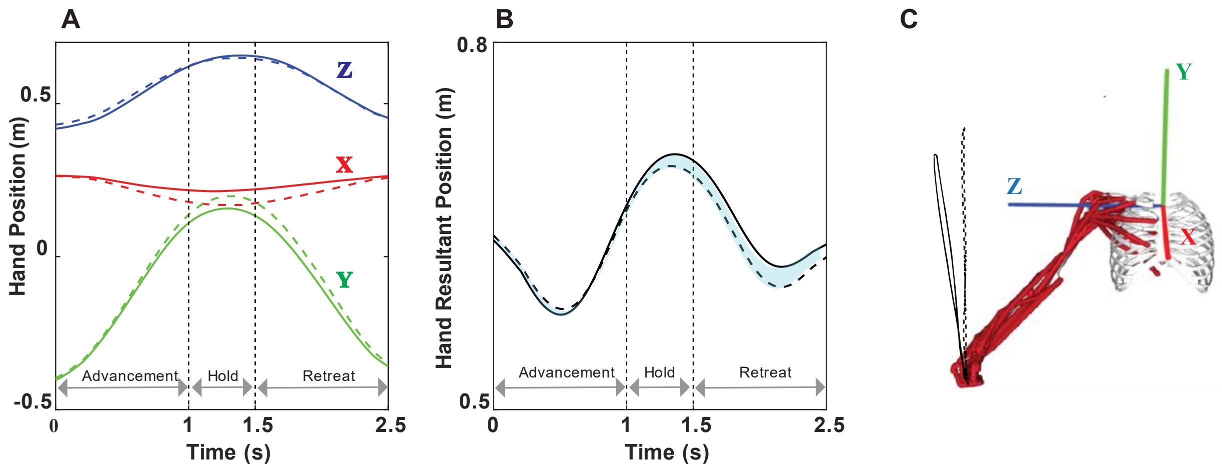

Figure 3-4. Hand position variability. (A) Hand COM trajectory components for the no-assistance (solid lines) and 40% assistance (dashed lines) trials when shoulder elevation to the above-shoulder target is simulated in the coronal plane. (B) The shaded area between the solid and dashed curves shows the resultant deviations across the movement cycles for the no-assistance and 40% assistance simulations. (C) The musculoskeletal model and 3D trajectory of the hand COM for the no-assistance (solid curve) and 40% assistance (dashed curve) simulations.

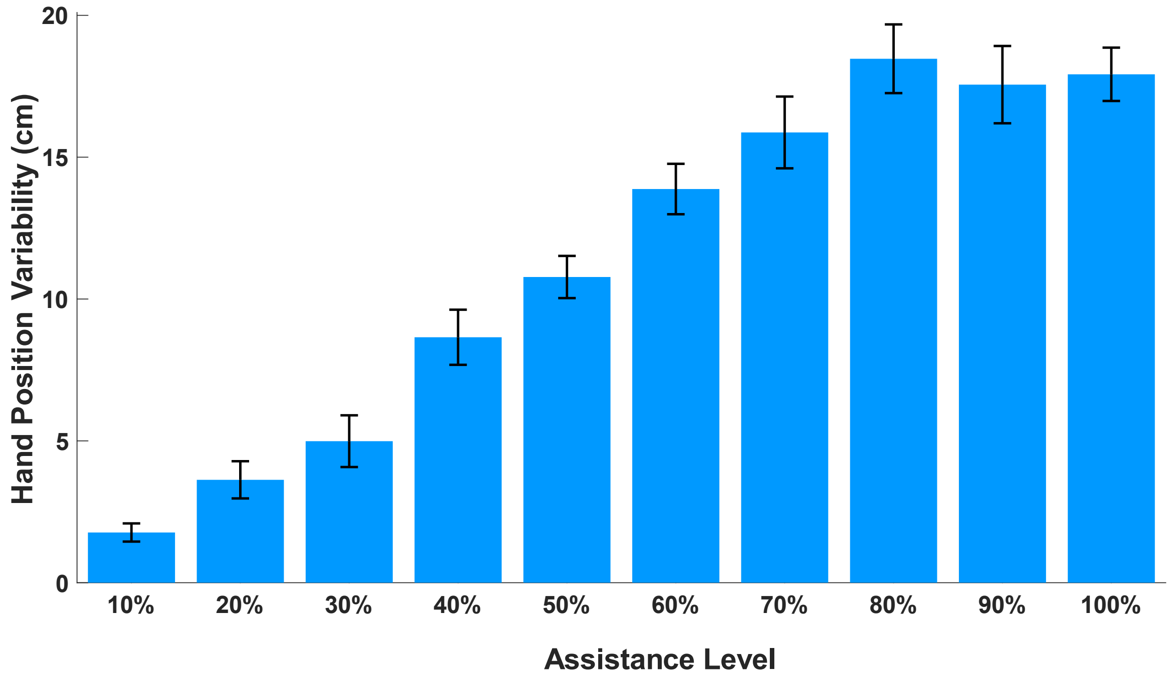

Figure 3-5. Hand position variability vs. assistance level for the simulated shoulder tasks. The bars and error bars show the mean the standard error of the end-point variability across the shoulder tasks.

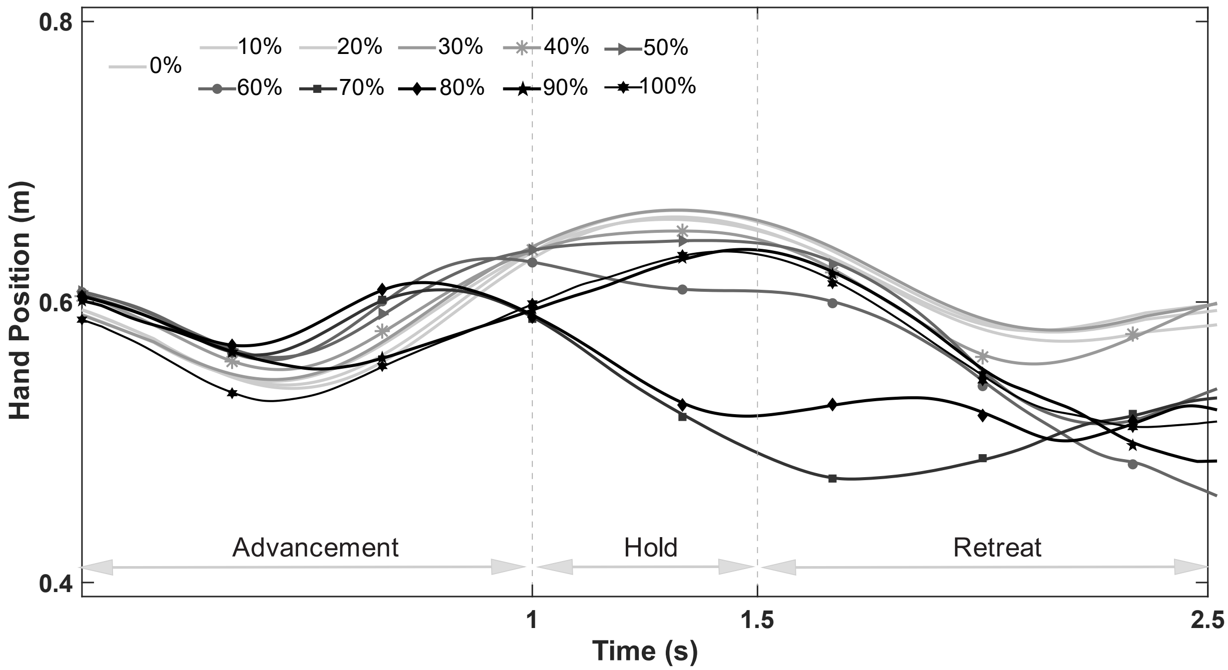

Figure 3-6. Hand resultant position for the scapular elevation to an above shoulder target. For assistance levels above 40%, the hand COM trajectory shows higher divergence, less precision, and dynamic instability.

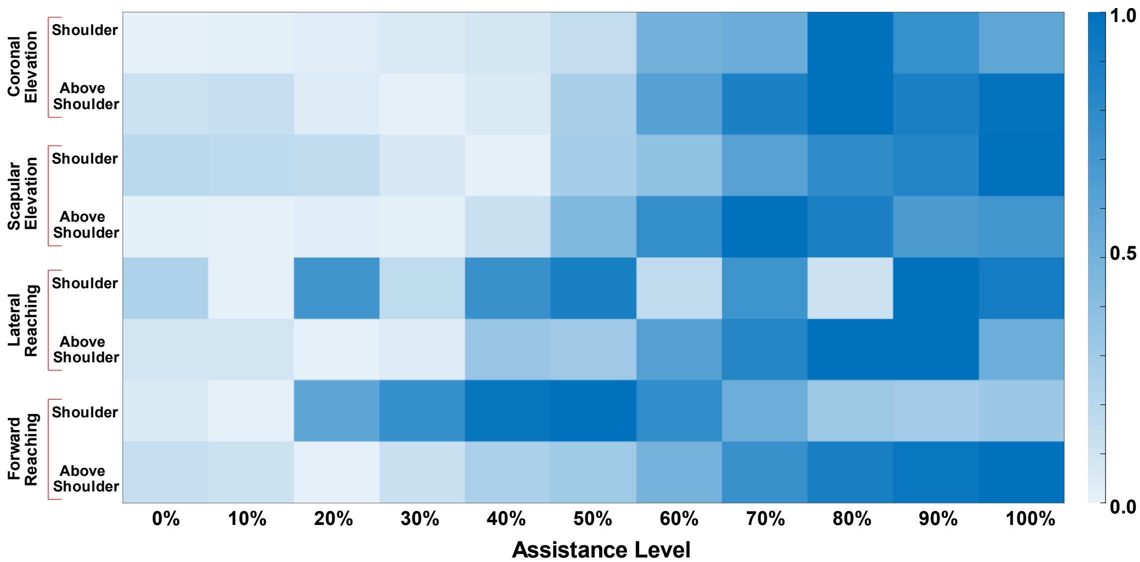

Figure 3-7. Total muscular effort rate for the simulated shoulder tasks. The sum of the effort rate of the shoulder muscles across the assistance levels was scaled to [0, 1]. Light color cells show less effort rate and darker ones show higher effort rate for the simulated task.

Efficiency, as defined in (18), ranged from 45% to 57% across all assistance levels (Figure 3-8). A large decrease in efficiency was observed for assistance levels greater than 20% compared to the no-assistance condition. Specifically, the average efficiency decreased from 54.10% to 51.81% with an increase in assistance torque from 20% to 30%. However, for assistance levels higher than 30%, efficiency remained consistently below 54.11%, without a clear trend.

GH stability

As can be seen in Figure 3-9, the median and variability of $GH_{stability}$ remained below one across all assistance levels. This suggests that the stability of the GH joint was mostly maintained across simulations, and that the resulting contact force at the GH joint was oriented within the glenoid rim. Between assistance levels of 10% and 30%, the median showed a slight decrease, while the interquartile and upper quartile ranges and the peak of the upper quartile increased compared to the no-assistance condition. At assistance levels of 40% or higher, the median and the magnitude and number of outliers generally increased with assistance level.

Figure 3-10 depicts the overlay of the AP and SI components of GH joint contact forces on the glenoid fossa for the lateral reaching task as an example. Consistent with the findings presented in Figure 3-9, the projected points onto the glenoid rim spread over a larger trace as the assistance level increases up to 30%. However, when considering assistance levels greater than 40%, there is a noticeable difference in the spread or distribution of the projected points compared to the spread observed for assistance levels below 40%.

Discussion

Identifying an optimal anti-gravity assistance level or range of levels for passive shoulder exoskeletons can potentially improve muscular efficiency while minimizing the undesirable effects on the user [36, 53, 82]. In this study, we leveraged the task space framework from robotics [130-132] to perform neuromusculoskeletal modeling and simulations to explore and identify an optimal assistance level for select functional shoulder movements. The simulated dynamic shoulder movements involved elevations in both the coronal and scapular planes, as well as forward and lateral reaching motions. These movements were simulated for two distinct hand target positions, one located at

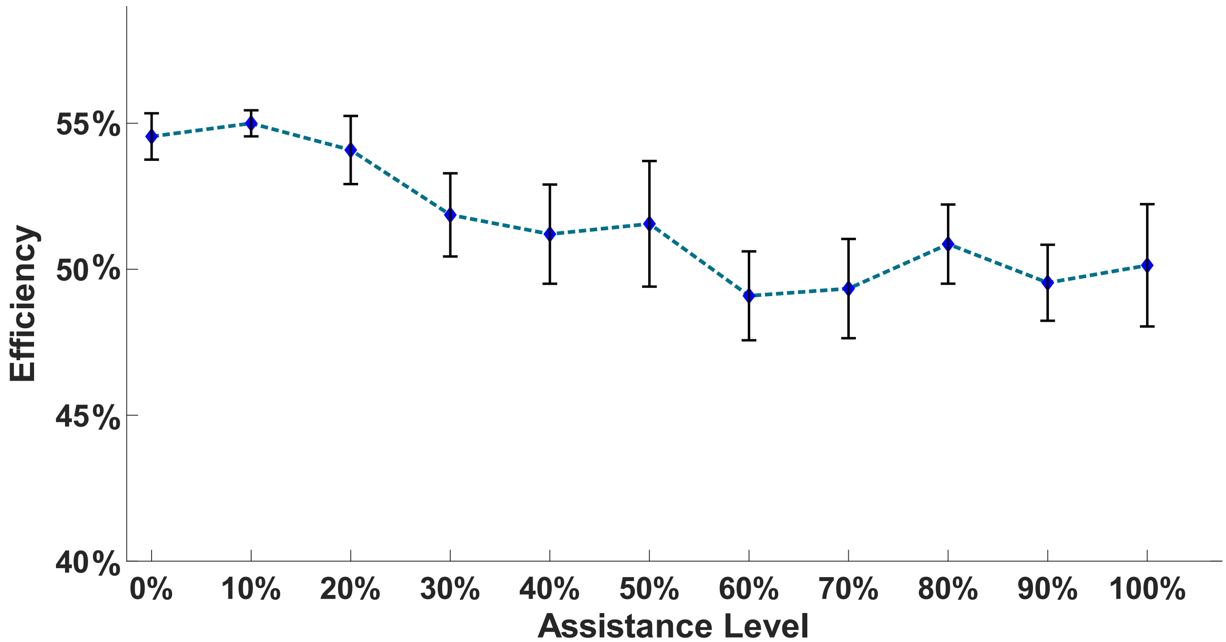

Figure 3-8. Mean efficiency ± standard error across the simulated task. The estimated efficiency reduces when assistance level is higher than 20%.

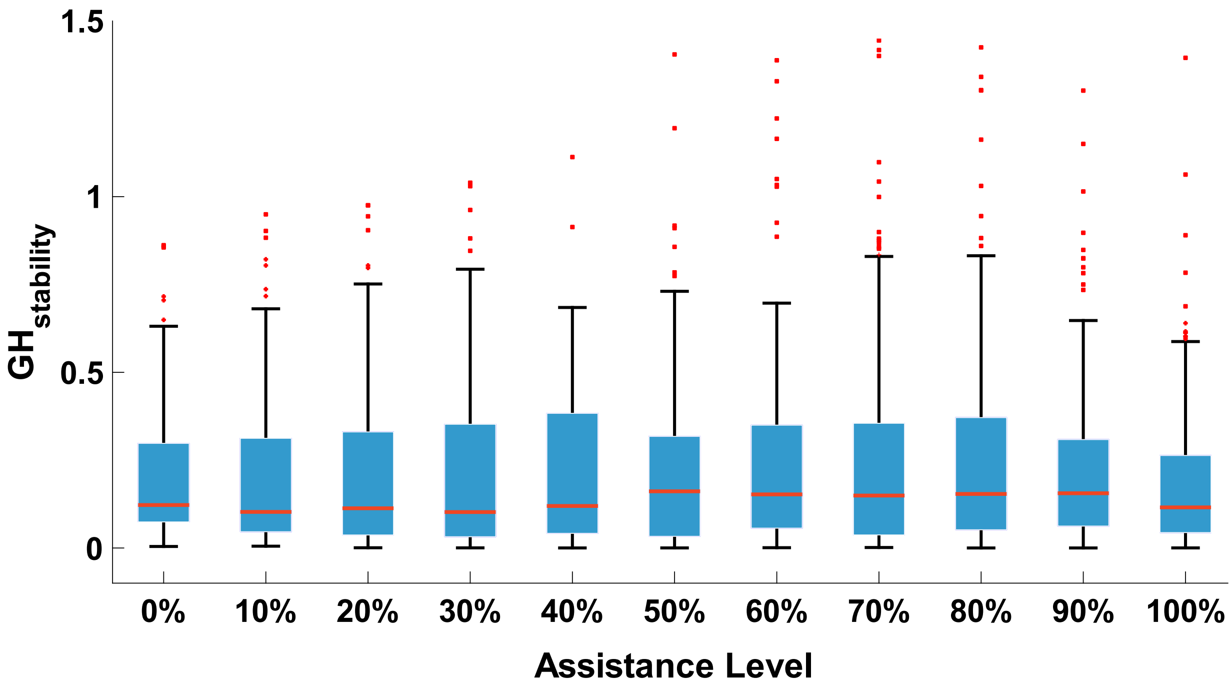

Figure 3-9. Box plot showing glenohumeral stability index vs. assistance level. The error bars show the standard error within the simulated tasks. For GHStability < 1, the GH joint is considered stable.

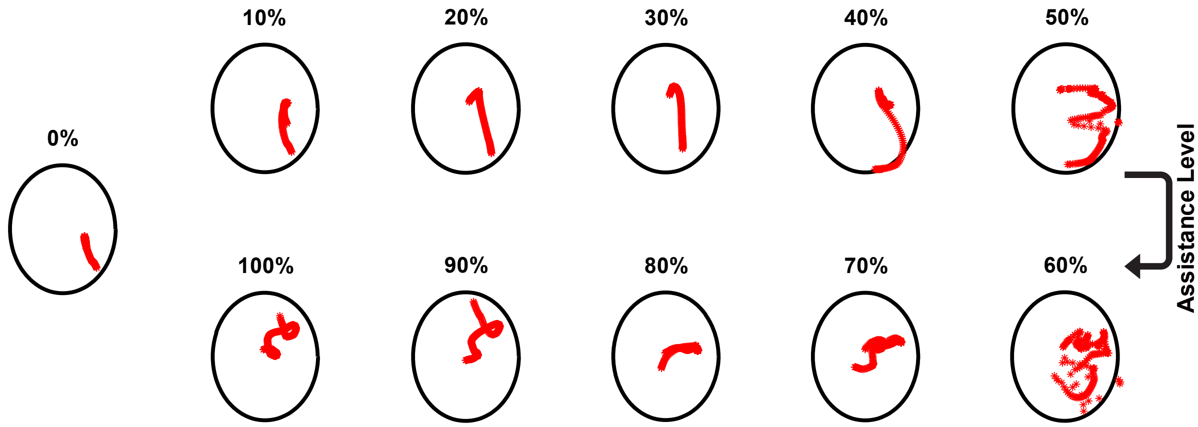

Figure 3-10. Projection of the glenohumeral contact force of the lateral reaching task onto the glenoid fossa for different assistance levels. The shape of the glenoid fossa was represented as an oval and the projection points were estimated using the ratio of the AP and SI components to the compressive component. The projected points are plotted every 20ms.

shoulder height and the other above it. Our simulation results demonstrated that, overall, an assistance level above 40% of the maximum gravity torque at the shoulder joint (defined above) can be associated with undesired negative effects during the simulated dynamic arm movements. These included greater end-limb (i.e., hand) movement variability, greater total muscle effort rate, less efficiency, and compromised GH stability and alignment.

The level of anti-gravity assistance applied to the shoulder joint can negatively impact the hand (i.e., end-limb) kinematics and dynamic stability [39]. The results obtained from our predictive task space framework indicate that the ability of the upper limb model to accurately track the desired hand trajectory decreases as the amount of anti-gravity assistive torque at the shoulder joint increases. This eventually led to higher amounts of divergence from the desired trajectory, and therefore hand dynamic instability, when assistance level was above 40%. This observation is consistent with studies on the use of the passive shoulder exoskeletons for overhead tasks, which reported higher errors and reduced quality for tasks that demanded higher precision like overhead drilling [39, 133]. Similarly, studies of robot-assisted rehabilitation for reaching movements reported performance degradation and higher endpoint error with increase in assistive force [134].

The simulated arm movements involved five DOFs of the upper extremity (Table 2-3), which is greater than the number of DOFs required for the 3-D positioning of the hand in the task space. This kinematic redundancy enables the task-posture controller to effectively decompose the generalized torques into two decoupled torque vectors that correspond to the desired hand trajectory and the arm posture [108, 130]. This decoupling prevents the torques, which are responsible for generating arm postural behaviors, from causing accelerations towards the end-limb task. However, at the muscle level, there are physiological limitations in muscular force generation that may impede the ability of the muscles to meet the kinetic demands of the task-posture control [135]. This potentially explains (1) the arm instability and end-limb divergence from the desired trajectory for high levels of assistive torque and (2) why the onset of hand resultant deviation in 3-D space was primarily coincident with the hand transition from acceleration to deceleration during the advancement phase (Figure 3-6).

Our results supported our hypothesis that there is an optimal assistance level for which the total shoulder muscle effort rate and efficiency are minimized. Previous studies provide evidence for the existence of an optimal assistance level for a passive ankle exoskeleton based on metabolic cost [136] and for assisted elbow flexion/extension movements based on muscular efficiency [103, 104]. In general, the optimal assistance level appears to be one that balances decreased activations of agonist muscles with increased activations of antagonist muscles. We used total muscle effort rate [65] and efficiency [104] to account for this balance. Our findings suggest that, for most of the simulated dynamic tasks, an assistance level of 10-30% minimized the total muscle effort rate and maximized efficiency. These results are consistent with previous studies that evaluated passive shoulder exoskeletons, such as WPCSE [82] and Exo4Work [36] , in which the maximum assistance torque was set to approximately 30% of the maximum shoulder gravity torque.

Interestingly, our results (Figure 3-8) indicated that, for reaching movements toward a shoulder-height target, an assistance level lower than 30% may be optimal, implying that the optimal level of assistance can be task-dependent. However, the assistance torque provided by some other commercially available passive overhead exoskeletons is closer to 50% [38] of the estimated gravity torque. This discrepancy may be attributed to the fact that commercial exoskeletons are primarily intended for use in static and quasi-static overhead tasks, while our simulated tasks involved dynamic overhead and shoulder-height reaching movements. Another potential explanation for this difference could be related to the fact that many experimental studies primarily employ surface electrodes to measure the electromyographic (EMG) activity of the shoulder muscles. This can limit their assessment of muscular effort to only the superficial muscles and not all the muscles spanning the shoulder joint.

Our study also revealed that high assistance, i.e., beyond 50% for the simulated tasks, might reduce efficiency. This is consistent with previous studies on assistance of single-joint movements, where increasing assistance force beyond an optimal level reduced the efficiency of the muscular response [103, 104, 137]. The provision of shoulder assistance during dynamic or quasi-static tasks can impact the activity of both agonist and antagonist muscle pairs [36, 37, 65, 82]. High levels of gravity-compensating torque have been shown to significantly decrease the activity of shoulder flexor muscles that mainly function to counteract gravity torque (i.e., load bearing muscles). However, the activity of the antagonist muscles, which are essential for joint stabilization and deceleration (i.e., fine-tuning muscles), does not necessarily decrease [36]. Studies have also reported that, in instances where the timing of a perturbing, high force is predictable, individuals tend to voluntarily increase the activation of their muscles in an attempt to stiffen their joint [137, 138]. Therefore, to deliver a higher efficiency, an optimal assistance level should not interfere with the synergistic activation of agonist and antagonist muscle pairs.

Shoulder exoskeletons should be designed to ensure the stability of the GH joint. Our study showed that the glenohumeral joint stability and alignment can be negatively influenced by high levels of shoulder assistance. The GH joint is a ball-and-socket joint that has an inherently unstable structure since the glenoid “socket” does not sufficiently surround the humeral head [1]. The bones, joint capsule [139], and ligaments [140] contribute most to the static stability of the GH joint [141]. The GH stability during dynamic movements, however, highly depends on the muscles surrounding the joint [141-143]. GH stability is maintained by ensuring that the resultant bone-on-bone joint contact force between the humerus and scapula is oriented within the boundary of the glenoid rim [141, 144]. Our results showed that, with increasing assistance level, the resultant GH joint contact force advanced closer to the edge of the glenoid rim and, therefore, the GH joint became less stable. Such instances of heightened instability and joint misalignment could eventually lead to injury and joint degeneration [145, 146].

Our simulation-based study had some limitations. First, we employed an ideal sinusoidal assistive torque to model the external assistive force/torque of a passive exoskeleton worn by the user. This approach, while simple, allows for generalizability of the results to a range of passive shoulder exoskeletons with differing designs. Nevertheless, in the future, including a model of an exoskeleton with inertial and other dynamic (e.g., damping) properties could provide more insightful and realistic outcomes. A second limitation of our study was that our simulations only explored dynamic reaching and elevating arm movements with fixed initial angles, thereby only capturing a limited subset of possible shoulder movements. To obtain a more comprehensive understanding of user-exoskeleton interaction, future studies should include a larger number of static, quasi-static, and dynamic movements that are representative of the wide range of tasks for which exoskeletons may be used. A third limitation of our study was the use of a fixed movement speed across all simulated tasks. It is important to note that movement speed plays a crucial role in the net torque generated at the shoulder joint during dynamic tasks, thereby affecting the level of muscular activity and demand [133]. Research in gait studies has indicated that the optimal exoskeleton stiffness level (comparable to gravity compensation level) that minimizes steady-state metabolic demand is higher at faster walking speeds [147]. This implies that different optimal assistance levels may be required for movements of varying speeds. Therefore, future studies should consider simulating arm movements at various speeds and explore the potential relationship between the assistance levels and movement speed.

Conclusion

In summary, the present study demonstrated the feasibility of using a robotics-based task-posture control framework to simulate goal-directed upper limb movements with external assistance. The dynamic task-posture decomposition enabled the execution of the goal-oriented movement in the task space while the assistance was provided in the posture space. Our study suggested that there may be an optimal level of anti-gravity assistance for passive shoulder exoskeletons depending on the types of movements or tasks that they are intended to support. This optimal level of assistance minimizes the user muscular effort rate and achieves a more efficient muscular response without compromising joint stability and limb kinematics. Specifically, our results indicate that for dynamic forward and lateral reaching movements and shoulder elevations in the frontal and scapular planes, an optimal assistance level lies within the range of 20-30% of the maximum gravity torque at the shoulder joint. However, future studies should explore a wider variety of movements with varying speeds to investigate the relationship between the level of assistance and movement speed.

CHAPTER 4 : DEVELOPING A REALISTIC MODEL OF FORCE-IMPEDANCE CONTROL FOR UPPER LIMB MOVEMENTS

This work is published as a conference paper for the 43rd Annual International Conference of the IEEE Engineering in Medicine & Biology Society (EMBC).

M. Asgari and D. L. Crouch, "Estimating Human Upper Limb Impedance Parameters From a State-of-the-Art Computational Neuromusculoskeletal Model," 2021 43rd Annual International Conference of the IEEE Engineering in Medicine & Biology Society (EMBC), 2021, pp. 4820-4823, doi: 10.1109/EMBC46164.2021.9630074.

Section 4-1: A Computational Approach to Estimate Human Upper Limb Impedance Parameters

Abstract

The human neuro-musculoskeletal system constantly deploys passive (e.g., posture adjustment) and active (e.g., muscle co-contraction) control strategies to regulate upper limb impedance and stability while interacting with the outside world. Upper limb impedance has been assessed through *in vivo* experiments and model-based simulations. The experiments are practically limited to small samples of able-bodied subjects and few limb postures, and model-based approaches have mostly used simplified arm models. Our objective was to develop and validate a computational approach to estimate upper limb impedance parameters - stiffness, viscosity, and inertia - at the endpoint (i.e., hand) using a neuromusculoskeletal model with a realistic geometry. We added a planar manipulandum to an existing upper limb model implemented in OpenSim (version 3.3) and used contact modeling to attach the manipulandum's handle to the musculoskeletal model's hand. The hand was placed at several locations lateral to the shoulder joint along anterior/posterior and medial/lateral axes. At each location, during forward dynamics simulations, the manipulandum applied small perturbations to the hand in eight different directions. The spatial variation of the computed, model-based impedance parameters was similar to that of experimentally measured impedance parameters. However, the overall size of the stiffness and viscosity components was larger in the model than from experiments.

Clinical Relevance— Our preliminary results suggest that computational modeling and simulations can be used to estimate upper limb impedance properties to complement and overcome the limitations of experiments. The computational approach

could ultimately inform new interventions and devices to restore limb stability in people with shoulder disabilities.

Introduction

The mechanical impedance of the human upper limb describes the limb's ability to resist moving when it is displaced from an equilibrium position [148], [149]. It is well-established that the human neuro-musculoskeletal system regulates limb impedance both passively (e.g., posture) and actively (e.g., muscle contraction) to maintain stability while manipulating objects and interacting with the environment [150]. There are many common orthopedic (e.g., rotator cuff tear) [151] or neurological (e.g., stroke) injuries that often lead to devastating shoulder disability. There is evidence that such disability can impair the passive and active mechanisms of the neuro-musculoskeletal system for impedance modulation, destabilizing the shoulder joint and hand position [152].

Impedance can be characterized by physical parameters stiffness, viscosity, and inertia from engineering dynamics [149]. The stiffness and viscosity components originate from the properties of the musculoskeletal system's passive and active tissues and can be further regulated by changing levels of muscle activation and co-activation. However, the inertia only depends on the arm posture and physical properties of the upper limb, like mass and length [153]. The standard technique to identify the impedance parameters is to build a second-order linear model from the experimental hand force field data [153], [154]. The hand force field describes the relation between displacements and restoring forces when the hand is perturbed about a given equilibrium position. Perturbations are typically applied to the hand by a planar robotic manipulandum. Impedance can be estimated either at the endpoint (i.e., hand) or at the joint level (i.e., shoulder and elbow) [150].

Impedance has been measured experimentally or estimated computationally. Due to practical reasons, experimental studies have limited testing to small numbers of able-bodied subjects (due to risk of injury to people with disability), trials (due to subject fatigue), and limb postures. At the same time, model-based studies have mainly used simplified models (e.g., with a few numbers of muscles) [155] or only estimated the stiffness parameter using muscle short-range stiffness modeling [156]. These limitations prevent full understanding of how the neuro-musculoskeletal system regulates impedance over the entire upper limb workspace under healthy and impaired conditions. Addressing this knowledge gap would inform new interventions and devices to help regulate impedance and restore limb stability in people with shoulder disability.

Computational approaches and simulations with use of more realistic musculoskeletal models can complement and overcome the limitations of current studies to more fully characterize the impedance properties of the upper limb. Thus, the overall objective of the proposed project was to develop a computational approach using an upper limb neuromusculoskeletal model with realistic geometry to estimate upper limb impedance parameters and validate the computational impedance results against published experimental results.

Methods

Modelling the musculoskeletal-manipulandum system

Our strategy in this preliminary study was to replicate a typical experiment set-up [153]. We added a planar two-joint manipulandum to an existing upper limb musculoskeletal model [105] implemented in OpenSim (version 3.3) [157]. The upper extremity model had 7 degrees of freedom, with three describing the shoulder kinematics and four describing the elbow and wrist kinematics. The model geometry is defined based on a 50th percentile male population's anthropometric data and contains fifty Hill-type muscle-tendon units crossing shoulder, elbow, and wrist joints. The manipulandum consisted of two rigid cylindrical links and massless torque actuators. The links have lengths of 0.30 and 0.25 m and moments of inertia of 0.0037 and 0.0013 $Kg.m^2$, respectively. The inertia of the manipulandum (i.e., mass matrix) was designed to be smaller than the model's arm to minimize the effect of nonlinear dynamic forces on the arm movements. The torque actuators were placed at the manipulandum joints to apply torques about the *z-axis* in the global coordinate system (Figure 4-1). The manipulandum included a handle (i.e., end-effector) whose centroid point along the *z-axis* was aligned with the shoulder along the *z-axis.*

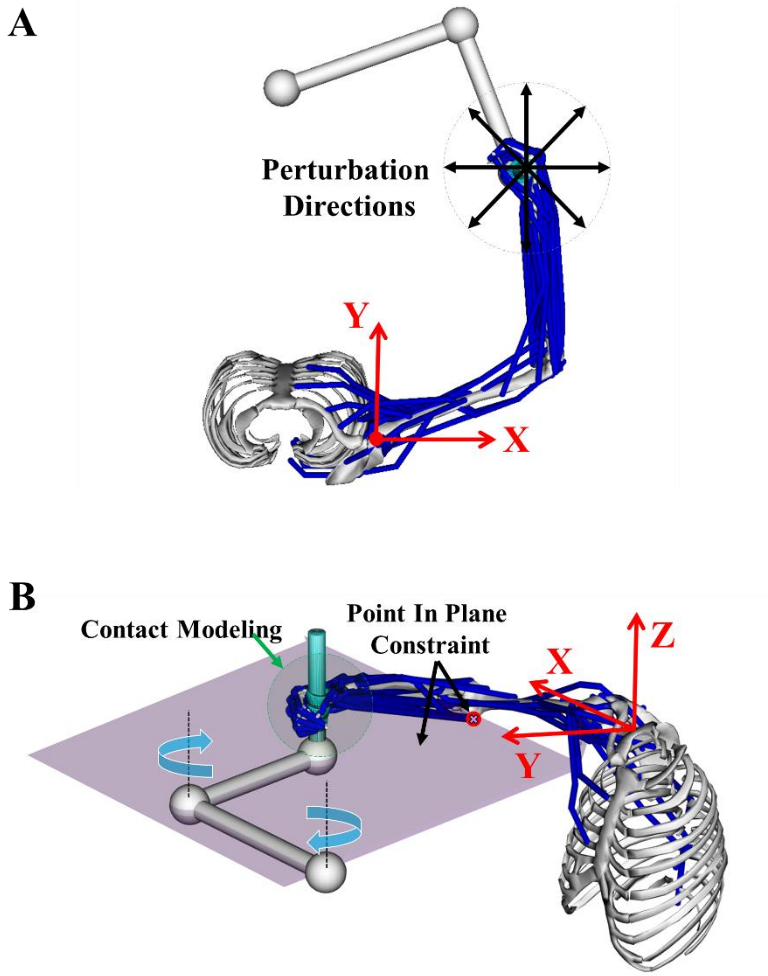

Figure 4-1. Musculoskeletal-manipulandum model. A) The arrows show the eight directions of perturbations applied to the hand. B) The meshed geometry of the handle was surrounded with three meshed disc geometries to represent the hand grip. The humerus trochlea was constrained to move on the horizontal plane.

We used contact modeling to attach the handle to the model's hand using OpenSim's elastic foundation algorithm. To resemble the fingers' grip around the handle, the meshed geometry of the handle was placed inside three meshed disk geometries. Contact parameters of stiffness and dissipation were set, respectively, to $25\text{x}10^6$ (N/m) and 0.4 Ns/m. Other coefficients of static, dynamic, and viscous friction were also defined based on Savescu's work [158].

A linear PD controller placed the handle in any desired position across the limb's reachable workspace and applied external perturbations to the hand (Figure 4-1. Musculoskeletal-manipulandum model. A) The arrows show the eight directions of perturbations applied to the hand. B) The meshed geometry of the handle was surrounded with three meshed disc geometries to represent the hand grip. The humerus trochlea was constrained to move on the horizontal plane. (A)). We used the following control law to determine the torque vector required to navigate the handle position:

$$\tau = J(q)^T \left[K_m (X_d - X) - B_m \dot{X}\right] \tag{1}$$

where τ is the torque vector; $J(q)$ is the Jacobian matrix defining the handle cartesian displacement from the manipulandum joint angles q; K_m and B_m represent the manipulandum stiffness and viscosity matrices, respectively; X_d is the desired position; X and $\dot{X}$ show the current position and velocity vectors of the handle. In this study, we fine-tuned the stiffness and viscosity matrices as:

$$K_m = \begin{bmatrix} 400g & 0 \\ 0 & 400g \end{bmatrix} (N/m), \qquad B_m = \begin{bmatrix} 150g & 0 \\ 0 & 150g \end{bmatrix} (Ns/m)$$

where g is the gravitational constant.

Forward dynamics

Though the upper limb was supported against gravity during experiments, participants may have had to actively hold their upper limb in the desired static posture while holding the manipulandum's handle. Thus, we used computed muscle control (CMC) to compute the steady-state muscle excitations required to hold the upper limb in a static posture at each of the handle's starting points. During CMC, the gravity field was set to zero. We assumed that changes in muscle excitations caused by the small hand perturbations during the experiment were negligible; thus, the steady-state muscle excitations were applied to the respective muscles at corresponding handle starting points throughout forward dynamics simulations.

At the start of each forward dynamics simulation, the manipulandum's handle (with hand attached) was moved to the starting point using the feedback control law (Eq. 1). Given the model's limited workspace in which muscle-tendon moment arms were previously validated [105], we chose starting points that were lateral to the shoulder joint. Eight equally spaced starting points (5 cm apart) were 33 cm anterior to the shoulder joint and from 3 to 48 cm along the x-axis (medial/lateral direction). Another eight equally spaced starting points were 23 cm lateral to the shoulder and from 13 to 48 cm along the y-axis (anterior/posterior).

Once at the starting point, the manipulandum perturbed the hand in eight different directions. To ensure that the model's hand and manipulandum handle were at rest, perturbations were applied first at 3 s after reaching the starting point then every 0.6 s thereafter. During perturbations, the wrist joint movement was limited by a rotational bushing force to mimic typical bracing used in experiments. Since participants' upper limbs were supported against gravity during experiments, the movement of the distal point of the humerus was constrained to only move in the horizontal plane at shoulder level (Figure 4-1 (B)) and the gravitational acceleration was set to zero. We set the perturbation amplitude and duration to 2 mm and 1.2 s, respectively. Handle displacements and restoring forces (i.e., contact forces) were recorded during simulations.

Arm endpoint stiffness estimation

To estimate the hand impedance parameters, we regressed a second-order linear model (Eq. 2) to the simulated force field similar to the earlier studies [152, 153].

$$\boldsymbol{M}d\ddot{X}(t) + \boldsymbol{B}d\dot{X}(t) + \boldsymbol{K}dX(t) = -dF(t) \tag{2}$$

where $\boldsymbol{M}$, $\boldsymbol{B}$, and $\boldsymbol{K}$ are inertial, viscosity, and stiffness matrices of the hand impedance, respectively; $d\ddot{X}(t)$, $d\dot{X}(t)$, and $dX(t)$ display, in order, the change in vectors of acceleration, velocity, and displacement of the handle, and $dF(t)$ is the change in restoring forces from perturbation onset. Handle acceleration and velocity were computed by taking second- and first-order derivatives from displacements. We wrote the impedance matrices of $\boldsymbol{M}$, $\boldsymbol{B}$, and $\boldsymbol{K}$ as the sum of a symmetric and an antisymmetric matrix. The symmetric and antisymmetric components define, respectively, the conservative and non-conservative parts of the hand force field (i.e., the relation of hand restoring forces to displacements). We visualized the conservative force field with graphical ellipses whose size, principal semi-axes (i.e., shape), and orientation are defined based on the determinant, eigenvalues, and eigenvectors of the symmetric impedance matrices, respectively. Each ellipse depicts the locus of restoring forces for hand perturbations in every direction by order of one unit (e.g., 1 m displacement for the stiffness). Thus, ellipses with a larger area (i.e., size) represent higher restoring forces at limb posture, and the ellipse's major and minor axes determine the values and directions of the highest and lowest restoring forces, respectively.

Results and Discussion

Figure 4-2 shows the typical handle displacements and restoring forces for perturbations along the *y-axis* from one starting point. Figure 4-3 and Figure 4-4 represent the ellipses of the estimated hand stiffness, viscosity, and inertia for starting points along the medial/lateral and anterior/posterior directions, respectively. At more medial and posterior starting points, the stiffness ellipses had lower eccentricity (Figure 4-3(A), Figure 4-4(A)) and the major axis orientation (i.e., high stiffness direction) changed towards the shoulder joint. For more extreme hand positions, the stiffness ellipses were mainly elongated in the major axis direction, but for medial/posterior positions, the stiffness ellipses became wider.

This confirmed that hand restoring forces were higher and more isotropic for postures that are more central and proximal to the shoulder joint, consistent with results from Tsuji [153]and Mussa-Ivaldi [148]. However, the overall size of our stiffness ellipses is larger than the values reported in [153] but smaller than the ones reported in [148]. The observed spatial pattern for stiffness ellipses is most likely due to increasing passive forces of biarticular muscles (e.g., triceps long head) and higher muscles activation at higher elbow flexion and shoulder horizontal adduction angles. Although CMC accounts for a minimum extent of muscle co-contraction, which might work for involuntary holding postures in our study, we still might have underestimated the level of co-contractions for agnostic/antagonistic muscles.

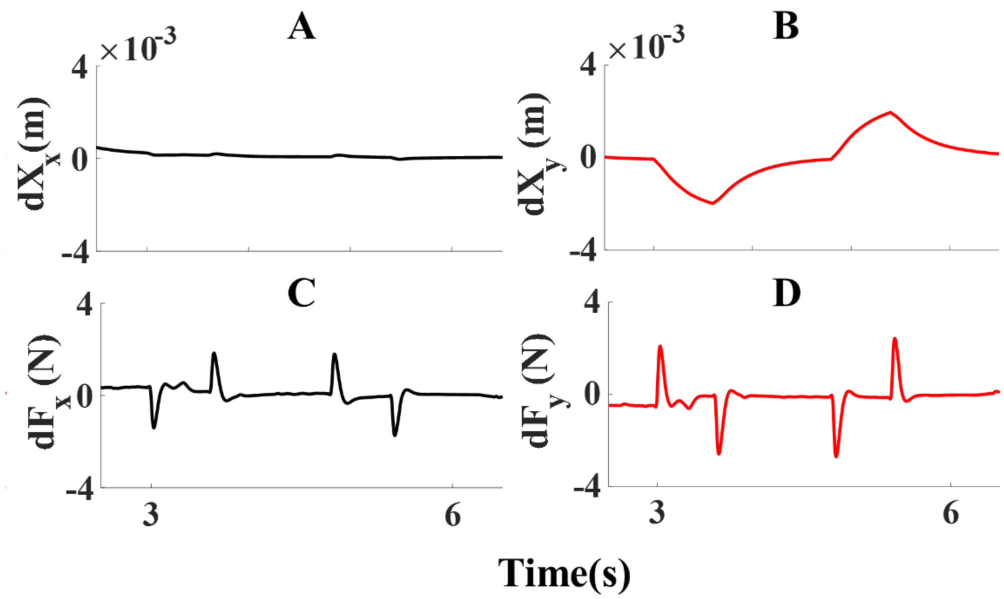

Figure 4-2. Sample handle displacements in x (A) and y directions (B) with corresponding restoring forces in x (C) and y directions (D) for a perturbation in y-axis.

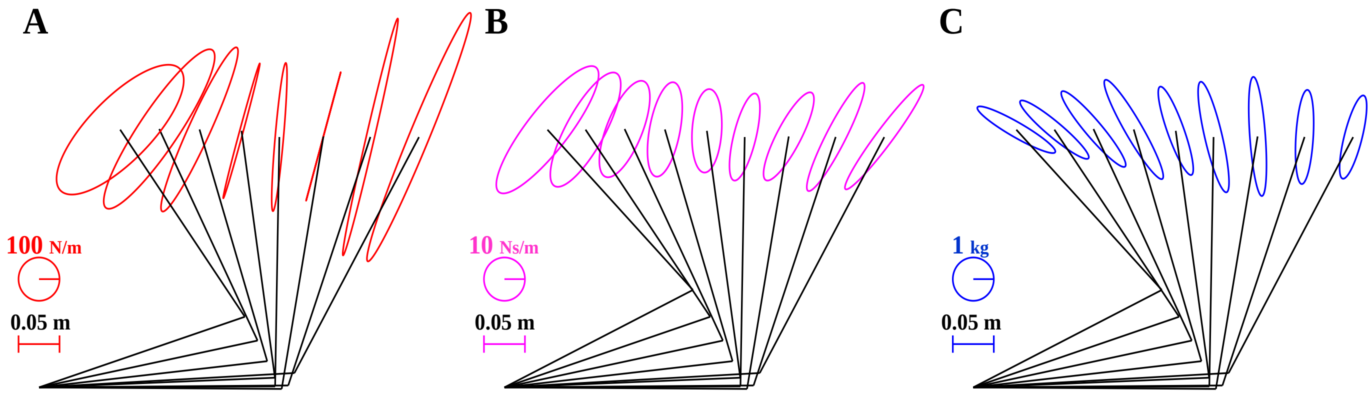

Figure 4-3. Estimated Stiffness (A), Viscosity (B), and Inertia ellipses (C) when hand displaced in the medial/lateral direction.

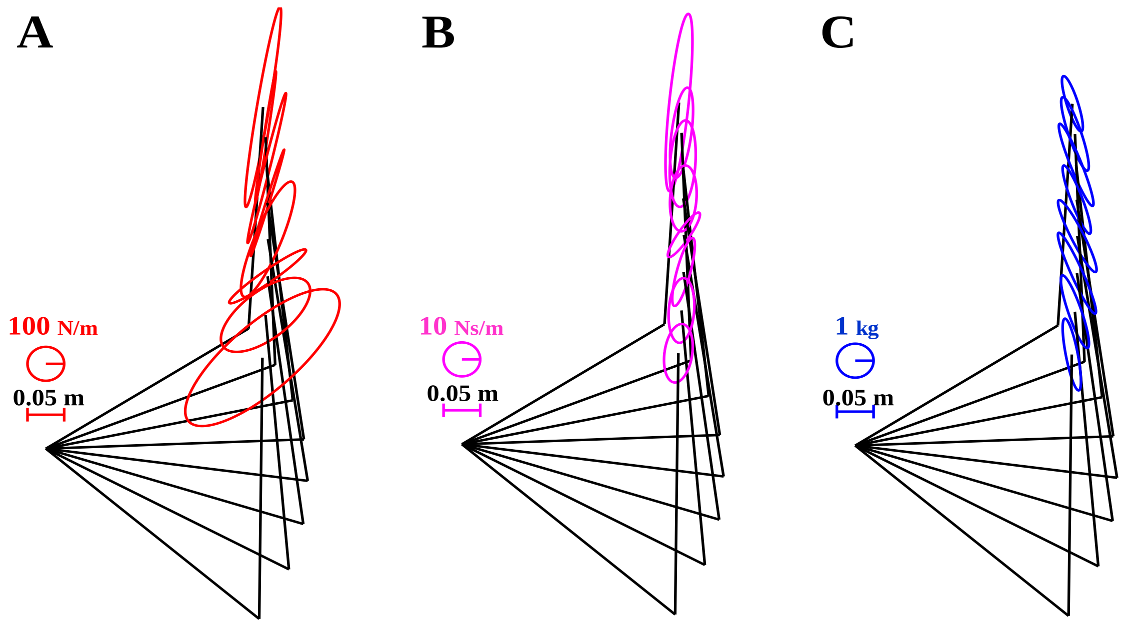

Figure 4-4. Estimated stiffness (A), Viscosity (B), and Inertia ellipses (C) for lateral hand positions when moved in the anterior/posterior direction.

The spatial pattern of the viscosity ellipses was similar to that of the stiffness ellipses, consistent with experimental results [153], [154]. The major axis of viscosity was aligned more towards the shoulder joint (Figure 4-3(B), Figure 4-4(B)), reflecting that the largest restoring forces against the speed occurred in the radial direction of the shoulder joint. The eccentricity of viscosity ellipses decreased toward more medial and posterior starting points, consistent with experiments [153]. The size of our viscosity ellipses, however, was substantially larger compared to experimental results. We suspect that viscosity is likely most influenced by muscles force-velocity relationships, muscles damping ratios, and hand-handle interaction.

The shape and orientation of the estimated inertia ellipses were well-matched with the experimental results. It is expected that the major axis of inertia ellipses will be nearly parallel with the distal segment of the limb (i.e., forearm/hand). This spatial pattern can be seen in Figure 4-3(C) and Figure 4-4(C) where the inertia ellipses rotated with the forearm/hand segment. To assess whether the estimated inertia ellipses were reasonable, we compared them to inertia ellipses computed for a two-joint arm whose links were cylindrical and have the same lengths and masses as the model's upper arm and forearm/hand. Compared to the calculated inertia ellipses, the estimated ones had similar orientations and shapes but smaller eccentricity and size (Figure 4-5). From these observations, we can infer that our modeling approach under-estimated the restoring forces against the acceleration.

Future Work & Conclusion

Our preliminary results suggest that computational modeling and simulations can be used to estimate the arm impedance properties to complement and overcome the limitations of experimental and model-based studies. The results from the simulation were fairly consistent with experimental results as 1) the orientation of the stiffness and viscosity ellipses were toward the center of the glenohumeral joint; 2) the eccentricity of the stiffness and viscosity ellipses increased toward anterior and lateral extreme hand positions; 3) the inertia ellipses were nearly parallel to the forearm/hand segment. There were, however, differences in the sizes of the inertia and viscosity ellipses between our model and previous experiments. These differences may be due to unmodelled muscle co-contractions and stretch reflexes, oversimplification of muscles and ligaments in the model, and missing passive human body components such as skin, veins, and cartilage.

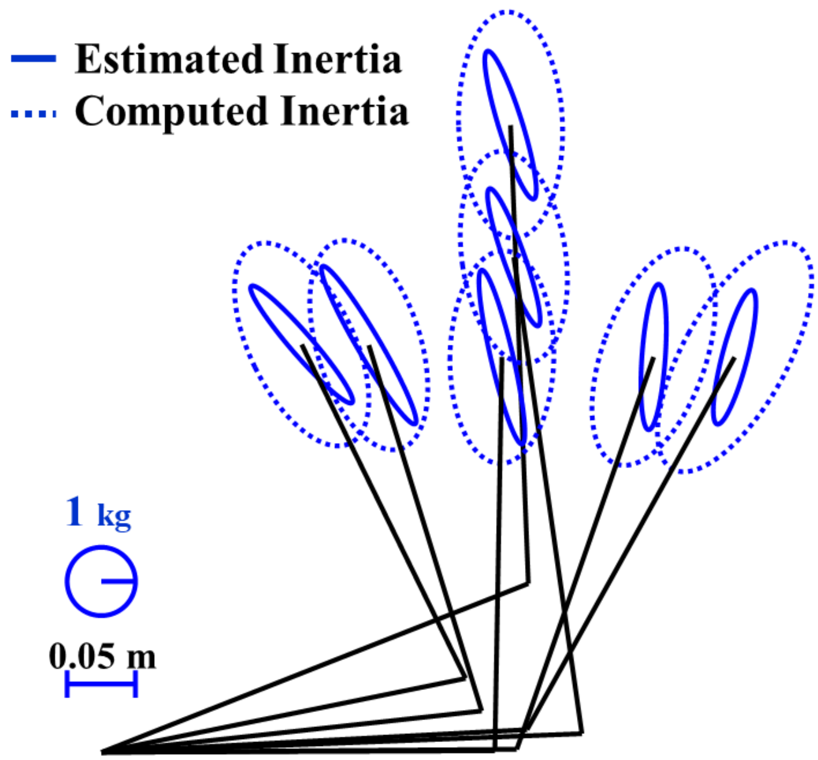

Figure 4-5. Estimated inertia from simulation vs. computed inertia from a simplified arm model with similar masses and lengths to that of the model's arm.

In future studies, we will (1) refine the computational approach to predict experimental data more accurately and (2) identify how anatomical and biomechanical features influence upper limb impedance.

Section 4-2: Three-dimensional computational musculoskeletal model for estimating force-impedance control during dynamic upper extremity movements

Abstract

The human neuro-musculoskeletal system has the ability to learn and adapt to new task dynamics, enhancing task performance and limb stability. This study aimed to develop and validate a realistic neuromusculoskeletal model of the upper limb capable of predicting stiffness modulation and motor adaptation to newly introduced environments and force fields. We employed an inverse task space dynamics approach with a multipriority task control framework for an existing upper limb model in OpenSim (Stanford, CA, USA). The task space controller was responsible for planning and executing muscle-driven goal-oriented movements for the arm while stabilizing these movements against disturbances. We performed simulations involving longitudinal and transverse reaching movements in a horizontal plane at the shoulder level and used the concept of short-range-stiffness to map the stiffness of muscle-tendon units onto end-limb stiffness. Additionally, we studied motor adaptations for longitudinal reaching movements in presence of three position-based divergent force fields and a velocity-dependent force field. Qualitatively, the proposed model and simulations accurately predicted previously reported, experimental end-limb stiffness properties. Our preliminary results indicated the potential of the proposed computational approach for estimating end-limb impedance parameters. Future studies should quantify the level of agreement between the model and experimental measurements for more upper extremity tasks.

Introduction

The neuromusculoskeletal systems stabilizes upper limb postures and movements when humans physically interact with the outside environment to manipulate or move objects [101, 159-161]. Studies show that such stabilization is only accomplished by controlling and modulating dynamic behavior (i.e., limb impedance) at the endpoint (i.e., hand) and joint levels [162, 163]. The endpoint impedance is usually described by an equivalent second-order mass-damping-spring system that has inertia, viscosity, and stiffness components [150, 153, 160]. These components relate restoring forces (or torques) in response to external (or internal) perturbations and determine whether the performing task is stable or unstable [159]. For unstable interactions, the applied disturbances become amplified [101, 102]. Almost every interaction-free upper limb movement that we execute is stable as it tends to return to the reference trajectory when perturbed externally or by inherent variability [101]. However, tasks involving unknown environments (e.g., wearing an assistive device) or use of tools and objects (e.g., carving or drilling) are unstable and require further stabilizing strategies by the central nervous system (CNS) [101]. When exposed to a novel dynamic environment with associated uncertainties, the CNS adapts arm movements against the destabilizing forces by increasing the co-contracting of agonist-antagonist muscle pairs [101, 102]. This motor adaptation is shown to happen only after the CNS learns and develops an inverse dynamic model of the environment by repeatedly interacting with it [160, 164].

A significant body of experimental studies has investigated how CNS regulates the shape, size, and orientation of the endpoint impedance during static postures [154, 165, 166] and dynamic movements [101, 167-169]. Experiments performed on posture maintenance concluded that the neuromusculoskeletal system is only able to regulate the shape and orientation of the stiffness to some limited extent (i.e., 30º counterclockwise) [154, 165, 166]. Contrary to the stiffness, the viscosity and inertia were mostly similar across different levels of muscle co-contractions [167]. Hu et. al. used musculoskeletal modeling to postulate how this limitation in stiffness modulation can be associated with biomechanical constraints and task requirements [170]. For dynamic reaching movements, however, subjects were able, after learning, to arbitrarily adjust the size and orientation of their endpoint stiffness to compensate for the instabilities provoked by velocity-dependent and divergent force fields [101]. The adjustment was associated with an increase in stiffness in the direction of the instability, while stiffness remained unchanged in the orthogonal direction [102, 161]. Most of the above studies constrained the arm movements to a 2-dimensional (2D), horizontal workspace, and only a few studies have attempted to extend the above findings into the 3D space [171]. This is partly due to the complex, multiple-joint, and kinematically redundant nature of 3D upper limb movements during which the CNS can independently modulate the impedance parameters. Another reason is the complications with experimentally measuring the impedance, such as limitations in the number of testing movements, postures, and participants.

Computational musculoskeletal models and simulations can overcome the limitations of experiments and, thus, are powerful tools to predict and better understand how humans interact within a new environment [163, 172]. Hu et al. [156] used a short-range-stiffness (SRS) muscle model and static optimization to characterize the arm endpoint stiffness at different levels of muscle co-contraction for stationary postures. Their model was later extended to estimate the endpoint stiffness during planar arm movements using a task space formulation [132, 173]. However, their methodology can be computationally expensive for 3D and multi DOFs models and cannot be used to predict motor adaptations [174]. On the other hand, Burdet et. al. [163, 172] proposed a simple, torque-driven, 2D model that could explain the force-impedance modulation and motor adaptations for arm postures and movements. They assumed that the joint stiffness was linearly related to the torques at the joints. This assumption was based on findings from experimental studies, which might not hold true for upper limb movements in 3D space [152]. Stochastic optimal control-based models account for the inherent sensorimotor noise while overcoming the pitfall of deterministic and energy-based minimization methods in modeling muscle co-contractions [175, 176]. However, these stochastic models are mainly based on simplified arm models and limited only to the horizontal movements.

The objective of this study was to develop a realistic neuromusculoskeletal model of force-impedance modulation for the upper limb movements that can help predict the dynamic stiffness modulation as well as motor adaptation to the newly introduced environments and force fields, such as those applied by an assistive device. The model was developed in the task space framework where a multi-priority control scheme is applied to plan and execute muscle-driven goal-oriented movements for the hand while stabilizing the hand movements against disturbances. We validated our model by comparing estimates of the end-limb stiffness with experimental data for horizontal reaching movements for: 1) dynamic longitudinal and transverse reaching movements in a horizontal plane in a null force filed (NF), and 2) longitudinal reaching movements in a velocity-dependent force field (VF), and three divergent force fields (DF).

Methods

The musculoskeletal model

For our musculoskeletal simulations, we used an upper limb musculoskeletal model [105] implemented in OpenSim (version 4.1). The model consists of shoulder, elbow, and wrist joints that are spanned by fifty Hill-type muscle-tendon units.

Task-level torque/motion controller

The task space equation of motion (EOM) for a kinematically constrained dynamic plant with generalized coordinate vector $\boldsymbol{q} \in \mathbb{R}^n$ can be summarized as follows:

$$\Lambda_c \ddot{\boldsymbol{x}} + \Lambda_c J M_C^{-1} P(h(\boldsymbol{q}, \dot{\boldsymbol{q}}) + \boldsymbol{\tau}_{ext}) - \Lambda_c J M_C^{-1} C_c \dot{\boldsymbol{q}} = \boldsymbol{F} \tag{1}$$

$$\Lambda_c = (J M_C^{-1} P J^T)^{-1},$$

$$M_c = PM(\boldsymbol{q})P + (I - P)M(\boldsymbol{q})(I - P),$$

$$P = I - J_C^{+} J_C, \text{ and } C = -J_C^{+} \dot{J}_C$$

where $J(\boldsymbol{q})$ is the task Jacobian; $h(\boldsymbol{q}, \dot{\boldsymbol{q}}) \in \mathbb{R}^n$ represents gravity, centripetal, and Coriolis forces; $M(\boldsymbol{q}) \in \mathbb{R}^{n \times n}$ is the mass matrix; $J_C(\boldsymbol{q})$ is the constraint Jacobian; and $\boldsymbol{F}$ represents task space forces. This formulation for the constrained inverse dynamics controller is based on the Aghilii method [113, 116] where the constraints forces get eliminated using an orthogonal projection operator P (where + indicates the Moore-Penrose pseudoinverse). The torque/motion controller law can be written as [107]:

$$\boldsymbol{\tau} = J^T \boldsymbol{F} + \left(I - J^T J^{T^{\#}}\right) \boldsymbol{\tau_0} \tag{2}$$

where $J^{T^{\#}} = (J M_C^{-1} P J^T)^{-1} J M_C^{-1} P$, and $\boldsymbol{\tau_0} \in \mathbb{R}^n$ is the initial posture torque vector. For such control law, the task space forces can be estimated from a desired task motion as the command input:

$$\ddot{\boldsymbol{x}} - \ddot{\boldsymbol{x}}_{\boldsymbol{d}} + k_d(\dot{\boldsymbol{x}} - \dot{\boldsymbol{x}}_{\boldsymbol{d}}) + k_p(\boldsymbol{x} - \boldsymbol{x}_{\boldsymbol{d}}) = 0 \tag{3}$$

where k_d and k_p are positive-definitive gain matrices.

This approach is fundamentally a torque-actuated controller that is statically and dynamically consistent [131]. This implies that the subtasks (i.e., posture control) never generate forces and accelerations that interfere with the ones from the higher priority tasks (i.e., end-limb motion). With the net generalized torques estimated at each step for task/posture control, we computed the required muscle excitations by minimizing the muscular effort through static optimization.

The terms on the right-hand-side (RHS) of equation (2) are mutually orthogonal as the first term is a subspace of the column space of matrix J^T, and the second term belongs to the null-space of J^T. DeSapio *et. al.* [130, 131] utilized the null-space projection to define a PD controller and a dissipative term to respectively minimize the muscular effort and oscillation for posture control. It is also common in the robotics community to leverage the null-space projection to perform two or more tasks simultaneously [118, 177, 178] for a redundant control plant (i.e., when there are more DOFs than necessary to execute a given task). This multipriority control is a well-established framework to execute such simultaneous tasks. This technique prevents tasks from interfering by successively projecting the lower priority tasks (i.e., low-level control primitives) onto the null space of the main task (i.e., high-level control).

The multipriority framework can also be applied to control and deal with the kinematic and dynamic redundancy inherent to the human upper limb [130]. The human upper limb includes extra DOFs at the joint (kinematic redundancy) and muscle (dynamic redundancy) levels to execute a given task in 3D space. The multipriority torque-control equation to perform two concurrent tasks can be formulated as:

$$\boldsymbol{\tau} = J_1^T \boldsymbol{F_1} + N_1^T J_2^T \boldsymbol{F_2} + N_a \boldsymbol{\tau_0}, \tag{4}$$

$$N_1^T = I - J_1^T J_1^{T^{\#}}, \; N_a = I - J_a^T J_a^{T^{\#}},$$

$$\text{and } J_a^T = [J_1^T \quad J_2^T]$$

where subscripts 1 and 2 stand for the primary and secondary tasks. $N_1^T \in \mathbb{R}^{n \times n}$ is the null-space projection matrix for the primary task that constrains the forces generated by the secondary task [130, 178]. J_a^T is called the augmented Jacobian of the primary and secondary tasks.

Mistry et. al. [113] argues that the control torques in (4) can be further reduced by multiplying the RHS by the orthogonal projection operator P as follows:

$$\boldsymbol{\tau} = PJ_1^T\boldsymbol{F_1} + PN_1^TJ_2^T\boldsymbol{F_2} + PN_a\boldsymbol{\tau_0} + (I-P)\boldsymbol{\tau_c} \tag{5}$$

This is true because the constraint forces produce no acceleration at the end-limb. The extra term $(I-P)\boldsymbol{\tau_c}$, however, can be considered to generate constraint forces with no motion in the joint space.

Relation of the task and muscle spaces

Using the principle of virtual work, we can relate the task space and muscle forces as follows:

$$\boldsymbol{\tau}^{\boldsymbol{T}}\boldsymbol{\delta q} = -\boldsymbol{f}_{\boldsymbol{M}}^{\boldsymbol{T}}\delta\boldsymbol{l}(\boldsymbol{q}) \tag{6}$$

$$\boldsymbol{\tau}^{\boldsymbol{T}}\boldsymbol{\delta q} = -\boldsymbol{f}_{\boldsymbol{M}}^{\boldsymbol{T}}\frac{\partial l}{\partial \boldsymbol{q}}\delta\boldsymbol{q}$$

$$\boldsymbol{\tau} = -L^T\boldsymbol{f_M}$$

where $L: \mathbb{R}^n \rightarrow \mathbb{R}^m$ is the muscle Jacobian; $\boldsymbol{f_M}$ is the vector of muscle forces; and the negative sign shows the positive work done during muscle contraction. The muscle force $\boldsymbol{f_M}$ is a nonlinear function of its maximum isometric force (F^{max}), activation level (a), length (l), and contraction velocity (v) and it is scaled along the tendon by the pennation angle ($\cos\,\alpha$) [132, 179].

Task-level neuromusculoskeletal controller

From (5) and (6), a task-level neuromusculoskeletal controller can be modelled as:

$$\boldsymbol{f_M} = -L^{T+}\boldsymbol{\tau} + (I - LL^+)\boldsymbol{f_{m0}} \tag{7}$$

where the task space forces can be mapped into the muscle space $\mathbb{R}^k \rightarrow \mathbb{R}^m$. The RHS terms in (7) are two orthogonal subspaces that belong to $\mathbb{R}^m$.

$$\boldsymbol{f_M} = \boldsymbol{f}_{\boldsymbol{M}}^{\parallel} \oplus \boldsymbol{f}_{\boldsymbol{M}}^{\perp} \tag{8}$$

$$\boldsymbol{f}_{\boldsymbol{M}}^{\parallel} \equiv -L^{T+}\boldsymbol{\tau}, \quad \boldsymbol{f}_{\boldsymbol{M}}^{\perp} \equiv (I - LL^+)\boldsymbol{f_{m0}}$$

The term $\boldsymbol{f}_{\boldsymbol{M}}^{\parallel}$ can be considered as the particular solution for the muscle forces while $\boldsymbol{f}_{\boldsymbol{M}}^{\perp}$ is an arbitrary vector of muscle forces in the null space of the muscle Jacobian. From a physiological perspective, $\boldsymbol{f}_{\boldsymbol{M}}^{\parallel}$ is the set of muscle forces that generate end-limb acceleration and correspond to the feedforward activation mechanism (i.e., reciprocal activation) of agonist-antagonist muscle pairs. Conversely, $\boldsymbol{f}_{\boldsymbol{M}}^{\perp}$ represents muscle forces that have no contribution to the end-limb acceleration and corresponds to the co-contraction mechanism. Note that the muscle forces in (7) are bounded and positive. For simplification, we assume that the muscle force is a linear function of its activation level:

$$\boldsymbol{f}_{\boldsymbol{M}} = \boldsymbol{a} \circ \boldsymbol{F}^{\boldsymbol{max}}(\boldsymbol{q}, \dot{\boldsymbol{q}}), \qquad 0 \leq a_i \leq 1 \tag{9}$$

where ∘ represents the Hadamard product. We then used static optimization [115, 119]. to solve for the muscle activations [180, 181]:

$$\boldsymbol{Minimize}\left[\begin{pmatrix} \hat{J} = \left\|\boldsymbol{a}^{\boldsymbol{2}}\right\| \\ \boldsymbol{a} \circ \boldsymbol{F}^{\boldsymbol{max}} == -L^{T+}\boldsymbol{\tau} + (I - LL^{+})\boldsymbol{f}_{\boldsymbol{m0}} \\ 0 \leq a_i \leq 1 \end{pmatrix}, \boldsymbol{a}\right] \tag{10}$$

Simulations

For validation of the proposed controller, we performed a series of simulations limited to the horizontal plane at the shoulder level and compared the results to those obtained from experimental and computational studies [163, 167]. The simulations included the estimation of end-limb dynamic stiffness during longitudinal and transverse movements (Figure 4-6) as well as adaptation to several known force fields.

Since the upper limb is supported against gravity during experiments, we set the gravity term to zero during our simulations. For successful simulations of the arm movements in a horizontal plane at the shoulder level, we used a multipriority framework with two tasks. The primary task was responsible for planning and executing the end-limb's point-to-point movement in the task space, while the secondary task constrained the elbow joint to move only on a horizontal plane at the shoulder level (i.e., shoulder elevation angle of 90º). Both tasks were positional tasks and were encoded based on equation (3) with specific gain matrices:

Primary task: $k_p = \begin{bmatrix} 100 & 0 & 0 \\ 0 & 100 & 0 \\ 0 & 0 & 100 \end{bmatrix}, k_d = \begin{bmatrix} 20 & 0 & 0 \\ 0 & 20 & 0 \\ 0 & 0 & 20 \end{bmatrix}$

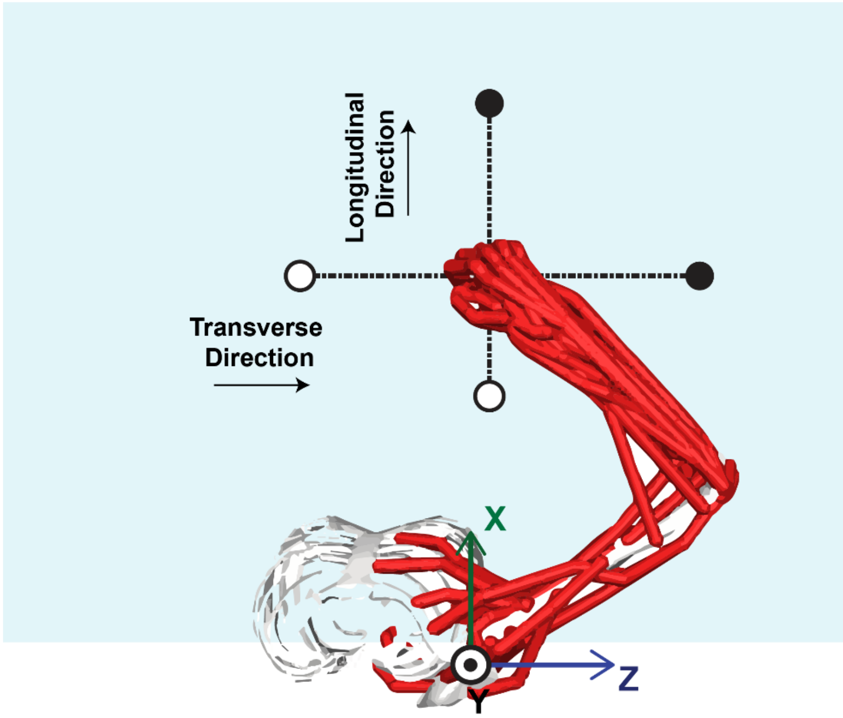

Figure 4-6.Simulation of the horizontal reaching tasks. Simulations were performed for point-to-point reaching movements within the horizontal plane at the shoulder level. Longitudinal movements start at (0.30, 0.0, 0.0) and end at (0.55, 0.0, 0.0) m, while transverse movements were from (-0.2, 0.0, 0.45) to (0.2, 0.0, 0.45) m. The start and end positions of these movements were marked by white and black circles, respectively.

Secondary task: $k_p = \begin{bmatrix} 0 & 0 & 0 \\ 0 & 100 & 0 \\ 0 & 0 & 0 \end{bmatrix}, k_d = \begin{bmatrix} 0 & 0 & 0 \\ 0 & 0 & 0 \\ 0 & 0 & 0 \end{bmatrix}$

During the simulations, we mimicked the typical bracing used in experiments by locking the degrees of freedom (DOFs) of the wrist joint. We also set $\boldsymbol{\tau_c}$ and $\boldsymbol{\tau_0}$ in equation (7) and $\boldsymbol{f_{m0}}$ in equation (10) to zero unless otherwise stated.

Dynamic stiffness

Similar to [163], we evaluated the end-limb stiffness during planar reaching movements at shoulder height, as shown in Figure 4-6. The longitudinal reaching movement started from the initial point (0.30, 0.0, 0.0) and ended at (0.55, 0.0, 0.0) m along the y-direction of the shoulder joint center. Similarly, the transverse reaching movements began at (-0.2, 0.0, 0.45) and concluded at (0.2, 0.0, 0.45) m. The duration of the longitudinal and transverse reaching movements was set to $T = 0.6s$ and $T = 1.0s$, respectively [163]. The desired trajectory for the end-limb (i.e., hand center of mass) was decoded using a minimum-jerk polynomial-based trajectory defined as:

$$\boldsymbol{x} = \boldsymbol{x_0} + \begin{bmatrix} A_x(6t_n^5 - 15t_n^4 + 10t_n^3) \\ 0 \\ A_z(6t_n^5 - 15t_n^4 + 10t_n^3) \end{bmatrix}, t_n = \frac{t}{T} \tag{11}$$

where A_x, and A_z are the movement amplitude in x and z, respectively; $\boldsymbol{x_0}$ shows the starting position. For transverse movement $A_x = 0$, and $A_z = 0.40m$, while for the longitudinal movement $A_x = 0.25m$, and $A_x = 0.25m$.

Motor adaptation to known stable and unstable interactions

We examined the motor adaptations during point-to-point arm reaching movements in the longitudinal directions for three position-based DF, and a VF (Figure 4-7). The general function used for the DF was:

$$\boldsymbol{F_E} = \kappa \begin{bmatrix} \cos\beta \\ 0 \\ \sin\beta \end{bmatrix} \boldsymbol{x} \ \mathrm{(N)} \tag{12}$$

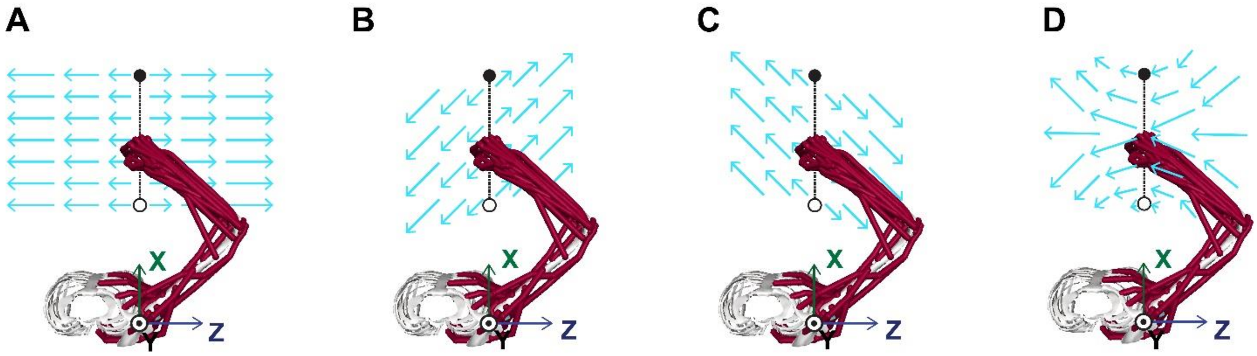

Figure 4-7. Illustration of simulated force fields. (A) divergent force field with $\kappa = 450, \beta = 0^o$, (B) divergent force field with $\kappa = 450, \beta = 45^o$, (C) divergent force field with $\kappa = 450, \beta = -45^o$, (D) velocity-dependent force field.

where κ and β determine the difficulty scale and rotation of the force field. We performed simulations for parameter sets of 1) $\kappa = 450, \beta = 0$, 2) $\kappa = 450, \beta = 45^o$, and 3) $\kappa = 450, \beta = -45^o$. The VF was also defined as:

$$\boldsymbol{F_E} = \begin{bmatrix} 13 & 0 & -18 \\ 0 & 0 & 0 \\ 18 & 0 & 13 \end{bmatrix} \dot{\boldsymbol{x}} \text{ (N)} \tag{13}$$

It was assumed that after motor adaptations are learned to the simulated divergent force (DF), the planned trajectory would resemble the null force field where no external force is applied [163]. However, based on experimental studies [101, 102], an increase in the end-limb stiffness (k_a) was assumed in the opposite direction of the imposed force fields. The Jacobian of the primary task was then used to map this stiffness adaptation term onto the joint space (equation (14)), considering it as constraint forces ($\boldsymbol{\tau_c}$) in the control law, equation (5). This approach allowed us to generate motion similar to the null field simulation while producing corresponding constraint forces at the upper limb joints.

$$\boldsymbol{\tau_c} = J_1^T k_a(\boldsymbol{x} - \boldsymbol{x_d}), \tag{14}$$

$$k_a = -\kappa \begin{bmatrix} \cos\beta & 0 & 0 \\ 0 & 0 & 0 \\ 0 & 0 & \sin\beta \end{bmatrix}$$

In a same way, we used following equation to estimate the constraint forces for the VF simulation:

$$\boldsymbol{\tau_c} = J_1^T k_a(\dot{\boldsymbol{x}} - \dot{\boldsymbol{x}}_{\boldsymbol{d}}), \tag{15}$$

$$k_a = -\begin{bmatrix} 13 & 0 & -18 \\ 0 & 0 & 0 \\ 18 & 0 & 13 \end{bmatrix}$$

Stiffness estimation

The experimental technique to quantify limb impedance involves using system identification tools to compute impedance parameters based on the measured response of the end-limb and joints to external perturbations [148, 149, 153, 160, 167]. The limb impedance behavior originates from the viscoelastic properties of the muscle-tendon units (MTUs) and reflex feedbacks (i.e., involuntary impedance). The musculoskeletal modeling approach also considers the limb stiffness to be a result of the MTU stiffness, and it maps the MTU stiffness onto the joint stiffness with the following equation [156, 170, 182]:

$$K_j = -\frac{\partial L^T}{\partial \boldsymbol{q}} \boldsymbol{f_M} - L^T K_{mtu} L \tag{16}$$

where K_j and K_{mtu} stand for the joint and MTU stiffnesses, respectively. The SRS phenomenon has a significant contribution to the MTU stiffness [156], and it can be modeled as the total stiffness of the muscle fibers K_m and tendons K_t:

$$K_{mtu} = \frac{K_m K_t}{K_m + K_t} \tag{17}$$

where K_t is the slope of the force-strain curve of the tendon, and K_m is estimated with [156]:

$$K_m = \frac{\gamma f_M}{l_0^m}, \qquad \gamma = 23.4 \tag{18}$$

l_0^m is the optimal muscle fiber length. Finally, the joint stiffness can be mapped onto the end-limb (i.e., task) stiffness by the task Jacobian.

$$K_x = J^{+T}(K_j - \frac{\partial J^T}{\partial \boldsymbol{q}} \boldsymbol{F}) J^+ \tag{19}$$

Graphical ellipses were employed to visualize the symmetric component of the end-limb stiffness matrix, K_x, and to assess the changes in its size, shape, and orientation during reaching movements in the presence of simulated force fields. The determinant, eigenvalues, and eigenvectors of the stiffness matrix define the size, shape, and orientation, respectively, of the graphical ellipse.

Results and Discussion

Dynamic Stiffness

Figure 4-8 illustrates the end-limb stiffness during the longitudinal reaching movement in a NF simulation. The stiffness ellipses are plotted with a 0.05 m distance from each other, starting from the position (0.30, 0.0, 0.0) m. Consistent with previous research [160, 163], the ellipses appear wider near the start point (i.e., more posterior)

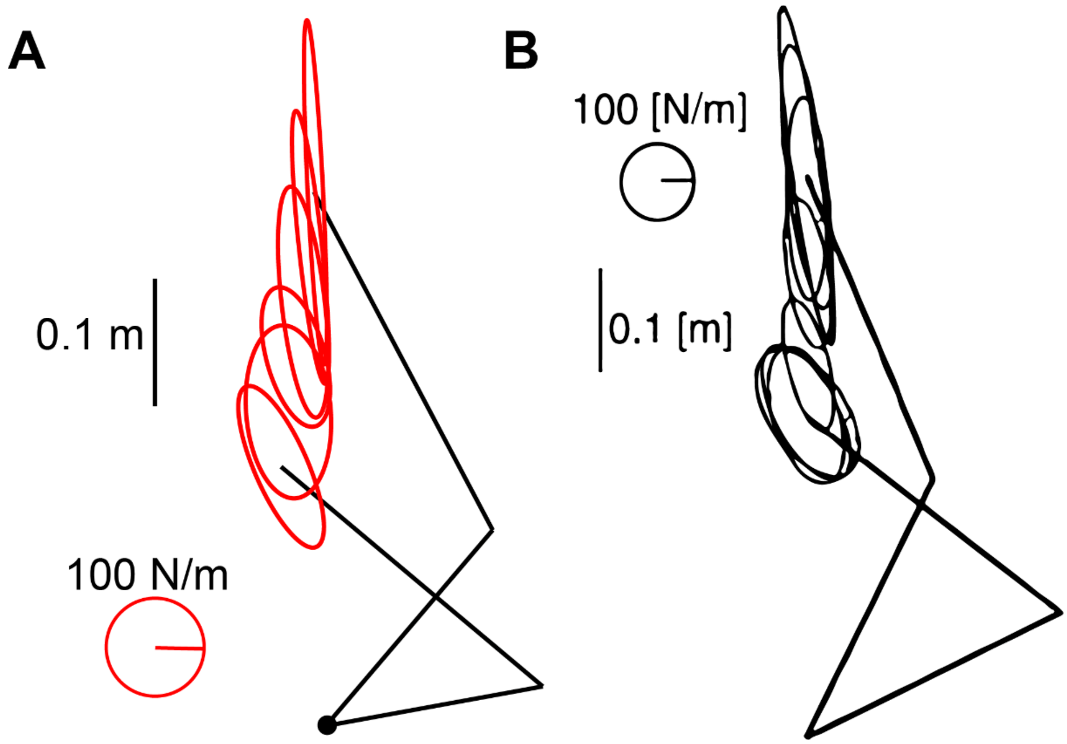

Figure 4-8. Stiffness ellipses for the longitudinal reaching movement in the null force field estimated by the model (A), measured from the experiment (B). In (A) the ellipses are 0.05 m distant from each other.

and elongate in the direction of the major axis as the hand approaches the end point (i.e., more anterior). Additionally, the major axis orientation slightly rotates clockwise, towards the shoulder joint center, as the hand moves towards the end point.

Figure 4-9 displays the stiffness ellipses for the transverse reaching movement, also simulated in a NF with 0.05m distance between each ellipse. As observed, the major axis of the stiffness ellipses orients towards the shoulder joint as the hand moves from more medial positions (i.e., closer to the start point) to lateral positions (i.e., closer to the end point). The stiffness ellipses are wider for the more medial positions and become thinner for positions lateral to the shoulder joint. These results align with findings from experimental [2] and computational [6] studies.

Motor adaptations to stable and unstable interactions with known force fields

Figure 4-10 depicts the stiffness adaptations predicted by the proposed model in response to the simulated force fields. The solid red ellipses represent the end-limb stiffness in the null field, while the dashed blue ellipses show the stiffness after adaptation, estimated 200ms after the start of the movements. It can be observed that for the three simulated force fields, the end-limb stiffness mainly enlarges in the direction of the instability caused by the corresponding force field. This finding is consistent with experimental studies[102, 163, 164, 183] where subjects learned to stabilize their movement trajectory by modulating their biarticular and mono-articular muscles activations. Similarly, the proposed model predicts the stiffness adaptation to the velocity-dependent force field, aligning with available studies [162, 163].

Our results showed that the proposed neuromusculoskeletal model successfully predicted and characterized the end-limb stiffness during the dynamic horizontal reaching movements as well as stiffness adaptations to stable/unstable interactions. The proposed approach could potentially be extended to upper limb movements in the three-dimensional (3D) space. Further studies are required to confirm the model's suitability for use in three-dimensional movement. Franklin et. al. [162] suggest that the end-limb stiffness modulation and adaptations can be achieved using an inverse dynamics model in combination with impedance control. Our study confirmed this as we used an inverse task space controller that tracks the position task goal. When no force is applied at the end-limb, the controller exhibits behavior similar to an impedance controller.

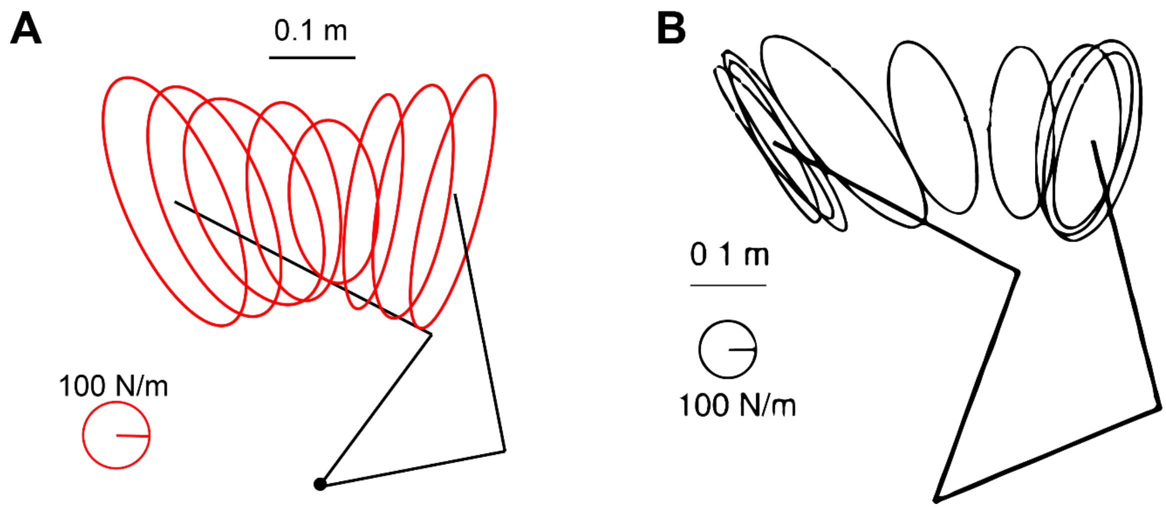

Figure 4-9. Stiffness ellipses depicted for the transverse reaching movement in the null force field estimated by the model (A), measured from the experiment (B). In (A) the ellipses are 0.05 m distant from each other.

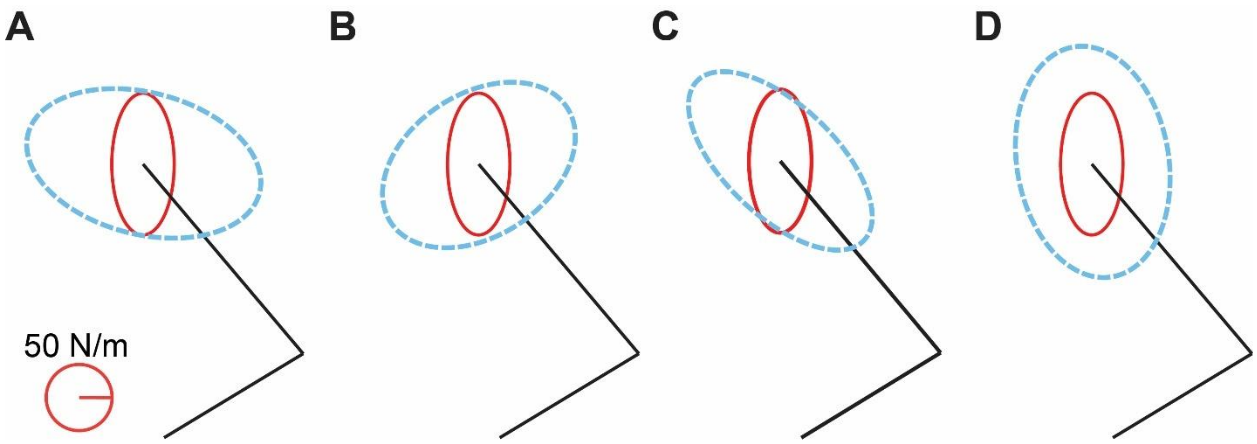

Figure 4-10. Stiffness ellipses after motor adaptations to the simulated force fields. Red ellipses show the end-limb stiffness for the null field simulation. Blue dashed ellipses show end-limb stiffness after adaptations. The stiffness was estimated at the time of 0.20s. stiffness adaptation to the divergent force field with $\kappa = 450, \beta = 0^o$ (A), divergent force field with $\kappa = 450, \beta = 45^o$ (B), divergent force field with $\kappa = 450, \beta = -45^o$ (C), and velocity-dependent force field (D).

By formulating the expected stiffness adaptations as constraint forces mapped onto the joint space, we were able to predict the adapted impedance. However, it is important to note that the proposed model may not be applicable in the presence of unknown interactions where a learning algorithm might be required to predict the motor adaptation.

Our study, in line with other computational investigations[156, 173], assumed that MTUs are the primary contributors to limb stiffness, and their SRS is proportional to the forces they generate. Therefore, musculoskeletal models with higher accuracy in estimating muscle-tendon dynamics and muscle excitations are expected to yield more accurate estimations of joint and end-limb stiffness. The central nervous system is known to achieve limb stability and impedance modulation through reciprocal activations of agonist/antagonist muscle pairs and their co-contractions [154, 159, 162, 174]. In our study, we employed static optimization with linear muscle assumptions for computational efficiency, but it does have limitations in estimating co-contractions [184]. Future research could enhance this model by using nonlinear muscle models and exhaustive search methods to explore the full range of muscle space solutions [173, 185].

Conclusion

This study introduced a comprehensive neuromusculoskeletal model of the arm, incorporating realistic 3D musculoskeletal geometry and a human-like control framework to examine endpoint stiffness during dynamic movements, and in response to environmental disturbances. The model employed an inverse task space dynamics approach with a multi-priority control scheme to execute muscle-driven goal-oriented movements. Simulation results demonstrated the model's ability to reasonably predict dynamic stiffness during horizontal reaching movements; our results were qualitatively consistent with experimental findings. However, further investigations are warranted to quantitatively assess the model's ability to predict stiffness modulation for 3D movements in novel environments, such as force fields applied by assistive devices.

CHAPTER 5 : CONCLUSION

Contributions

The foremost contribution of this research is the development of a prototype of a compact, lightweight, inexpensive, wearable passive cam-based shoulder exoskeleton. The proposed exoskeleton was designed to offer continuous, at-home assistance for dynamic activities of every day. The proposed exoskeleton incorporates a novel spring-cam-wheel module, which can generate a customizable assistive force. This force can be adapted to counteract varying proportions of the shoulder's elevation moment due to gravity.

The second contribution is conduction of a biomechanical study examining the impact of the proposed shoulder exoskeleton on the shoulder neuromuscular biomechanics and kinematics during dynamics elevation movements of the shoulder. Though the outcomes are specific to the proposed exoskeleton design, they have relevant implications for any other gravity-compensating passive shoulder exoskeleton.

The next contribution of this dissertation is demonstration of the feasibility of using a robotics-based task-posture control framework to simulate goal-directed upper limb movements while defining an impedance behavior for posture control.

Another contribution is a simulation study that, firstly, offers a computational robotics-driven methodology to determine the optimal level of anti-gravity assistance for various dynamic shoulder tasks. Secondly, it explores the impact of anti-gravity assistance level on neuromuscular biomechanics of the shoulder in terms of endpoint kinematic variability, muscular response and efficiency, and GH joint stability. The outcomes of this study inform the design of passive shoulder exoskeletons by providing insights into the ideal assistance levels they can offer based on the tasks they are designed for.

The concluding contribution of this research involves the introduction of two computer models focusing on force-impedance modulation for upper limb movements. Both models incorporate a realistic geometry of the upper limb and hold the potential to be applicable for both two- and three-dimensional movements. The first model is a musculoskeletal-manipulandum model that intends to estimate arm impedance properties during posture maintenance tasks. The second model, however, employs a multipriority control framework and can be used for estimation of stiffness modulation and motor adaptations in presence of destabilizing forces.

Future Work

There are several potential directions to progress this research in future studies, some of which are discussed below. These future works should eventually justify future development and clinical translation of portable passive shoulder exoskeletons to be used in home and community settings.

The work covered in chapter 1 serves as the foundation for the development and biomechanical assessment of a wearable passive shoulder exoskeleton (WPCSE). However, the WPCSE is currently in its early prototype stage and requires further enhancement before it can be employed in clinical settings. Some of the proposed refinements for the WPCSE include the incorporation of safety mechanisms, the optimization of routing geometries for the Bowden cable to reduce friction losses, the inclusion of an adjustability feature to offer a range of assistance levels, and the provision of adjustability for a range of user anthropometry. The study of WPCSE on shoulder biomechanics was only limited to able-bodied subjects. Testing in a patient population will be essential for demonstrating device safety and efficacy to support clinical use. However, patients with shoulder disability may have underlying tissue injuries, muscle coordination patterns, or other conditions that could put them at increased risk for injury or re-injury when using a novel, untested device prototype. Thus, more comprehensive biomechanical studies will be performed to assess the WPCSE for more participants (both able-bodied subjects and people with shoulder disability), with more biomechanical parameters (e.g., range of motion and endpoint/hand kinematics), and more movements that typify activities of daily living.

In chapter 3, I conducted a computational study to investigate how different levels of assistance influence the endpoint error and variability, shoulder muscular response, and GH joint stability. The outcomes also showed how an optimal anti-gravity assistance level can be achieved across shoulder functional tasks for passive shoulder exoskeleton. However, the outcomes of this study can be dependent on the simulation’s parameters and settings such as the command task and posture accelerations. Therefore, further sensitivity analysis is required to investigate the effects of gain matrices of command task/posture accelerations on optimal anti-gravity assistance level. Additionally, I performed simulations assuming fixed movement speed for a limited number of shoulder tasks. However, speed plays a crucial role in the net torque generated at the shoulder joint during dynamic tasks. Future studies should explore a wider variety of movements with varying speeds to investigate the relationship between the level of assistance and movement speed.

In chapter 4, I introduced two neuromusculoskeletal models of the arm, incorporating realistic 3D musculoskeletal geometry to examine endpoint stiffness during posture maintenance and dynamic movements. However, our simulations were only carried out for movements constrained to horizontal plane at the shoulder level. Future investigations can progress the work by assessing the applicability of the proposed models in predicting stiffness modulation for movements in 3D space. Since the second model proposed in section 4-2 incorporates a human-like control framework, it can be used to perform more computational studies to investigate the end-limb stiffness in presence of different assistance levels at the shoulder joint during dynamic and static movements.

REFERENCES

[1] J. P. Iannotti, and G. R. Williams, *Disorders of the shoulder: diagnosis & management*: Lippincott Williams & Wilkins, 2007.

[2] R. J. Meislin, J. W. Sperling, and T. P. Stitik, "Persistent shoulder pain: epidemiology, pathophysiology, and diagnosis," *Am J. Orthop.,* vol. 34, no. 12 Suppl, pp. 5-9, 2005.

[3] T. Kuijpers, M. W. van Tulder, G. J. van der Heijden, L. M. Bouter, and D. A. van der Windt, "Costs of shoulder pain in primary care consulters: a prospective cohort study in The Netherlands," *BMC Musculoskeletal Disorders,* vol. 7, no. 1, pp. 83, 2006.

[4] L. Virta, P. Joranger, J. I. Brox, and R. Eriksson, "Costs of shoulder pain and resource use in primary health care: a cost-of-illness study in Sweden," *BMC musculoskeletal disorders,* vol. 13, no. 1, pp. 17, 2012.

[5] N. Bureau of Labor Statistics 2016, " Nonfatal Occupational Injuries and Illnesses Requiring Days Away from Work, 2015. bls.gov, Washington, DC Retrieved from: https://www.bls.gov/news.release/archives/osh2_11102016.pdf."

[6] A. Ostor, C. Richards, A. Prevost, C. Speed, and B. Hazleman, "Diagnosis and relation to general health of shoulder disorders presenting to primary care," *Rheumatology,* vol. 44, no. 6, pp. 800-805, 2005.

[7] T. Burner, D. Abbott, K. Huber, M. Stout, R. Fleming, B. Wessel, E. Massey, A. Rosenthal, and E. Burns, "Shoulder symptoms and function in geriatric patients," *Journal of geriatric physical therapy (2001),* vol. 37, no. 4, pp. 154-158, Oct-Dec, 2014.

[8] H. F. Van der Molen, C. Foresti, J. G. Daams, M. H. Frings-Dresen, and P. P. F. Kuijer, "Work-related risk factors for specific shoulder disorders: a systematic review and meta-analysis," *Occupational and Environmental Medicine,* vol. 74, no. 10, pp. 745-755, 2017.

[9] T. M. Sukal, M. D. Ellis, and J. P. Dewald, "Shoulder abduction-induced reductions in reaching work area following hemiparetic stroke: neuroscientific implications," *Exp. Brain Res.,* vol. 183, no. 2, pp. 215-223, 2007.

[10] D. L. Crouch, A. C. Santago II, J. F. Plate, Z. Li, and K. R. Saul, "Relationship between maximum isometric joint moment and functional task performance in patients with brachial plexus injury: A pilot study," *Gait Posture,* vol. 44, pp. 238-244, 2016.

[11] S. J. Kolb, and J. T. Kissel, "Spinal Muscular Atrophy," *Neurol. Clin.,* vol. 33, no. 4, pp. 831-846, 2015.

[12] J. L. Wofford, R. J. Mansfield, and R. S. Watkins, "Patient characteristics and clinical management of patients with shoulder pain in US primary care settings: secondary data analysis of the National Ambulatory Medical Care Survey," *BMC musculoskeletal disorders,* vol. 6, no. 1, pp. 4, 2005.

[13] A. Yamamoto, K. Takagishi, T. Osawa, T. Yanagawa, D. Nakajima, H. Shitara, and T. Kobayashi, "Prevalence and risk factors of a rotator cuff tear in the

general population," *Journal of shoulder and elbow surgery,* vol. 19, no. 1, pp. 116-120, 2010.

[14] R. A. McCabe, S. J. Nicholas, K. D. Montgomery, J. J. Finneran, and M. P. McHugh, "The effect of rotator cuff tear size on shoulder strength and range of motion," *Journal of Orthopaedic & Sports Physical Therapy,* vol. 35, no. 3, pp. 130-135, 2005.

[15] D. Harryman 2nd, L. Mack, K. Wang, S. Jackins, M. Richardson, and F. Matsen 3rd, "Repairs of the rotator cuff. Correlation of functional results with integrity of the cuff," *JBJS,* vol. 73, no. 7, pp. 982-989, 1991.

[16] P. Collin, N. Matsumura, A. Lädermann, P. J. Denard, and G. Walch, "Relationship between massive chronic rotator cuff tear pattern and loss of active shoulder range of motion," *Journal of shoulder and elbow surgery,* vol. 23, no. 8, pp. 1195-1202, 2014.

[17] J. Rosen, J. C. Perry, N. Manning, S. Burns, and B. Hannaford, "The human arm kinematics and dynamics during daily activities - toward a 7 DOF upper limb powered exoskeleton." pp. 532-539.

[18] J. Liu, R. Hughes, W. Smutz, G. Niebur, and K. Nan-An, "Roles of deltoid and rotator cuff muscles in shoulder elevation," *Clinical Biomechanics,* vol. 12, no. 1, pp. 32-38, 1997.

[19] H. I. Krebs, M. Ferraro, S. P. Buerger, M. J. Newbery, A. Makiyama, M. Sandmann, D. Lynch, B. T. Volpe, and N. Hogan, "Rehabilitation robotics: pilot trial of a spatial extension for MIT-Manus," *J. Neuroeng. Rehabil.,* vol. 1, no. 1, pp. 5, 2004.

[20] J. C. Perry, J. Rosen, and S. Burns, "Upper-limb powered exoskeleton design," *IEEE/ASME Trans. Mechatron.,* vol. 12, no. 4, pp. 408-417, 2007.

[21] T. Nef, and R. Riener, "Shoulder actuation mechanisms for arm rehabilitation exoskeletons." pp. 862-868.

[22] A. Frisoli, M. Bergamasco, M. C. Carboncini, and B. Rossi, "Robotic assisted rehabilitation in virtual reality with the L-EXOS," *Stud. Health Technol. Inform.,* vol. 145, pp. 40-54, 2009.

[23] T. Nef, M. Guidali, and R. Riener, "ARMin III–arm therapy exoskeleton with an ergonomic shoulder actuation," *Appl. Bionics Biomech.,* vol. 6, no. 2, pp. 127-142, 2009.

[24] Y. Mao, and S. K. Agrawal, "Design of a cable-driven arm exoskeleton (CAREX) for neural rehabilitation," *IEEE Transactions on Robotics,* vol. 28, no. 4, pp. 922-931, 2012.

[25] C. Sicuri, G. Porcellini, and G. Merolla, "Robotics in shoulder rehabilitation," *Muscles, ligaments and tendons journal,* vol. 4, no. 2, pp. 207, 2014.

[26] P. Lucieer, and J. L. Herder, "Design of an adjustable compensation mechanism for use in a passive arm support." pp. 491-500.

[27] R. J. Sanchez, J. Liu, S. Rao, P. Shah, R. Smith, T. Rahman, S. C. Cramer, J. E. Bobrow, and D. J. Reinkensmeyer, "Automating Arm Movement Training Following Severe Stroke: Functional Exercises With Quantitative Feedback in a Gravity-Reduced Environment," *IEEE Trans. Neural Syst. Rehabilitation Eng.,* vol. 14, no. 3, pp. 378-389, 2006.

[28] R. Sanchez, D. Reinkensmeyer, P. Shah, J. Liu, S. Rao, R. Smith, S. Cramer, T. Rahman, and J. Bobrow, "Monitoring functional arm movement for home-based therapy after stroke." pp. 4787-4790.

[29] G. F. Lewin, H. S. Alfonso, and J. J. Alan, “Evidence for the long term cost effectiveness of home care reablement programs,” *Clinical interventions in aging*, pp. 1273-1281, 2013.
[30] Y. L. Yasuda, K. Bowman, and J. D. Hsu, “Mobile arm supports: criteria for successful use in muscle disease patients,” *Arch. Phys. Med. Rehabil. ,* vol. 67, no. 4, pp. 253-256, 1986.
[31] M. S. Atkins, J. M. Baumgarten, Y. L. Yasuda, R. Adkins, R. L. Waters, P. Leung, and P. Requejo, “Mobile arm supports: evidence-based benefits and criteria for use,” *J. Spinal Cord Med.,* vol. 31, no. 4, pp. 388-393, 2008.
[32] T. Rahman, W. Sample, S. Jayakumar, and M. M. King, “Passive exoskeletons for assisting limb movement,” *J. Rehabil. Res. Dev.,* vol. 43, no. 5, pp. 583, 2006.
[33] R. Sanchez, D. Reinkensmeyer, P. Shah, J. Liu, S. Rao, R. Smith, S. Cramer, T. Rahman, and J. Bobrow, "Monitoring functional arm movement for home-based therapy after stroke." pp. 4787-4790.
[34] A. de Vries, M. Murphy, R. Könemann, I. Kingma, and M. de Looze, “The amount of support provided by a passive arm support exoskeleton in a range of elevated arm postures,” *IISE Trans. Occup. Ergon. Hum. Factors*, pp. 1-11, 2019.
[35] M. A. Nussbaum, B. D. Lowe, M. de Looze, C. Harris-Adamson, and M. Smets, “An Introduction to the Special Issue on Occupational Exoskeletons,” *IISE Trans. Occup. Ergon. Hum. Factors,* vol. 7, no. 3-4, pp. 153-162, 2019/10/02, 2019.
[36] M. Rossini, S. De Bock, A. van der Have, L. Flynn, D. Rodriguez-Ciancia, K. De Pauw, D. Lefeber, J. Geeroms, and C. Rodriguez-Guerrero, “Design and Evaluation of a Passive Cable-driven Occupational Shoulder Exoskeleton,” *IEEE Transactions on Medical Robotics and Bionics*, 2021.
[37] L. Van Engelhoven, N. Poon, H. Kazerooni, D. Rempel, A. Barr, and C. Harris-Adamson, “Experimental evaluation of a shoulder-support exoskeleton for overhead work: Influences of peak torque amplitude, task, and tool mass,” *IISE Trans. Occup.,* vol. 7, no. 3-4, pp. 250-263, 2019.
[38] I. Pacifico, A. Scano, E. Guanziroli, M. Moise, L. Morelli, A. Chiavenna, D. Romo, S. Spada, G. Colombina, and F. Molteni, “An experimental evaluation of the proto-mate: a novel ergonomic upper-limb exoskeleton to reduce workers' physical strain,” *IEEE Robotics & Automation Magazine,* vol. 27, no. 1, pp. 54-65, 2020.
[39] S. Alabdulkarim, S. Kim, and M. A. Nussbaum, “Effects of exoskeleton design and precision requirements on physical demands and quality in a simulated overhead drilling task,” *Appl. Ergon.,* vol. 80, pp. 136-145, 2019/10/01/, 2019.
[40] P. Yin, L. Yang, S. Qu, and C. Wang, “Effects of a passive upper extremity exoskeleton for overhead tasks,” *Journal of Electromyography and Kinesiology,* vol. 55, pp. 102478, 2020/12/01/, 2020.
[41] C. Gerber, A. G. Schneeberger, M. Beck, and U. Schlegel, “Mechanical strength of repairs of the rotator cuff,” *J. Bone Joint Surg. ,* vol. 76, no. 3, pp. 371-380, 1994.
[42] A. Sunderland, D. Tinson, L. Bradley, and R. L. Hewer, “Arm function after stroke. An evaluation of grip strength as a measure of recovery and a prognostic indicator,” *Journal of Neurology, Neurosurgery & Psychiatry,* vol. 52, no. 11, pp. 1267-1272, 1989.
[43] S. Roderick, M. Liszka, and C. Carignan, "Design of an arm exoskeleton with scapula motion for shoulder rehabilitation." pp. 524-531.

[44] J. L. Herder, N. Vrijlandt, T. Antonides, M. Cloosterman, and P. L. Mastenbroek, “Principle and design of a mobile arm support for people with muscular weakness,” *Journal of rehabilitation research and development,* vol. 43, no. 5, pp. 591, 2006.

[45] A. H. Stienen, E. E. Hekman, G. B. Prange, M. J. Jannink, F. C. van der Helm, and H. van der Kooij, “Freebal: design of a dedicated weight-support system for upper-extremity rehabilitation,” *Journal of medical devices,* vol. 3, no. 4, 2009.

[46] P.-Y. Lin, W.-B. Shieh, and D.-Z. Chen, “A theoretical study of weight-balanced mechanisms for design of spring assistive mobile arm support (MAS),” *Mechanism and Machine Theory,* vol. 61, pp. 156-167, 2013.

[47] Z. Cheng, S. Foong, D. Sun, and U.-X. Tan, "Towards a multi-DOF passive balancing mechanism for upper limbs." pp. 508-513.

[48] J. S. Schroeder, and J. C. Perry, "Development of a series wrapping cam mechanism for energy transfer in wearable arm support applications." pp. 585-590.

[49] J. T. McConville, C. E. Clauser, T. D. Churchill, J. Cuzzi, and I. Kaleps, *Anthropometric relationships of body and body segment moments of inertia*, ANTHROPOLOGY RESEARCH PROJECT INC YELLOW SPRINGS OH, 1980.

[50] K. R. Holzbaur, W. M. Murray, and S. L. Delp, “A model of the upper extremity for simulating musculoskeletal surgery and analyzing neuromuscular control,” *Annals of biomedical engineering,* vol. 33, no. 6, pp. 829-840, 2005.

[51] E. S. Lawrence, C. Coshall, R. Dundas, J. Stewart, A. G. Rudd, R. Howard, and C. D. Wolfe, “Estimates of the prevalence of acute stroke impairments and disability in a multiethnic population,” *Stroke,* vol. 32, no. 6, pp. 1279-1284, 2001.

[52] M. Coscia, V. C. K. Cheung, P. Tropea, A. Koenig, V. Monaco, C. Bennis, S. Micera, and P. Bonato, “The effect of arm weight support on upper limb muscle synergies during reaching movements,” *J. Neuroeng. Rehabil.,* vol. 11, no. 1, pp. 22, 2014/03/04, 2014.

[53] P. T. Hall, and D. L. Crouch, “Effect of continuous, mechanically passive, anti-gravity assistance on kinematics and muscle activity during dynamic shoulder elevation,” *J. Biomech.*, pp. 109685, 2020/02/26/, 2020.

[54] A. Frisoli, F. Rocchi, S. Marcheschi, A. Dettori, F. Salsedo, and M. Bergamasco, "A new force-feedback arm exoskeleton for haptic interaction in virtual environments." pp. 195-201.

[55] H. Park, R. Yupeng, and Z. Li-Qun, "IntelliArm: An exoskeleton for diagnosis and treatment of patients with neurological impairments." pp. 109-114.

[56] Y. Mao, X. Jin, G. G. Dutta, J. P. Scholz, and S. K. Agrawal, “Human movement training with a cable driven arm exoskeleton (CAREX),” *IEEE Trans. Neural Syst. Rehabilitation Eng.,* vol. 23, no. 1, pp. 84-92, 2014.

[57] Z. Li, W. Chen, J. Zhang, and S. Bai, "Design and control of a 4-DOF cable-driven arm rehabilitation robot (CARR-4)." pp. 581-586.

[58] W. James, and J. Orr, “Upper limb weakness in children with Duchenne muscular dystrophy–a neglected problem,” *Prosthet. Orthot. Int.,* vol. 8, no. 2, pp. 111-113, 1984.

[59] J. T. McConville, *Anthropometric relationships of body and body segment moments of inertia*: Air Force Aerospace Medical Research Laboratory, Aerospace Medical Division …, 1981.

[60] D. A. Winter, *Biomechanics and motor control of human movement*: John Wiley & Sons, 2009.

[61] P. W. Hill, E. T. Wolbrecht, and J. C. Perry, "Gravity Compensation of an Exoskeleton Joint Using Constant-Force Springs." pp. 311-316.
[62] T. Rahman, W. Sample, R. Seliktar, M. T. Scavina, A. L. Clark, K. Moran, and M. A. Alexander, “Design and testing of a functional arm orthosis in patients with neuromuscular diseases,” *IEEE Trans. Neural Syst. Rehabilitation Eng.,* vol. 15, no. 2, pp. 244-251, 2007.
[63] J. R. McGuire, and J. A. Yura, “Advances in the analysis and design of constant-torque springs,” 1996.
[64] M. Asgari, P. T. Hall, B. S. Moore, and D. L. Crouch, "Wearable shoulder exoskeleton with spring-cam mechanism for customizable, nonlinear gravity compensation." pp. 4926-4929.
[65] A. J. Nelson, P. T. Hall, K. R. Saul, and D. L. Crouch, “Effect of Mechanically Passive, Wearable Shoulder Exoskeletons on Muscle Output During Dynamic Upper Extremity Movements: A Computational Simulation Study,” *J. Appl. Biomech.,* vol. 36, no. 2, pp. 59-67, 2020.
[66] P. H. Tidwell, N. Bandukwala, S. G. Dhande, C. F. Reinholtz, and G. Webb, “Synthesis of wrapping cams,” 1994.
[67] S. Namdari, G. Yagnik, D. D. Ebaugh, S. Nagda, M. L. Ramsey, G. R. Williams, Jr., and S. Mehta, “Defining functional shoulder range of motion for activities of daily living,” *J Shoulder Elbow Surg,* vol. 21, no. 9, pp. 1177-83, Sep, 2012.
[68] W. J. Hanney, M. J. Kolber, and S. J. Marshall, “The reliability of clinical measurements designed to quantify shoulder mobility,” *Physical Therapy Reviews,* vol. 16, no. 6, pp. 413-422, 2011.
[69] J. N. Hodder, and P. J. Keir, “Obtaining maximum muscle excitation for normalizing shoulder electromyography in dynamic contractions,” *J Electromyogr. Kinesiol.,* vol. 23, no. 5, pp. 1166-1173, 2013.
[70] G. Wu, F. C. Van der Helm, H. D. Veeger, M. Makhsous, P. Van Roy, C. Anglin, J. Nagels, A. R. Karduna, K. McQuade, and X. Wang, “ISB recommendation on definitions of joint coordinate systems of various joints for the reporting of human joint motion—Part II: shoulder, elbow, wrist and hand,” *J. Biomech.,* vol. 38, no. 5, pp. 981-992, 2005.
[71] R. Merletti, and P. Di Torino, “Standards for reporting EMG data,” *J Electromyogr. Kinesiol.,* vol. 9, no. 1, pp. 3-4, 1999.
[72] S. Kim, M. A. Nussbaum, M. I. M. Esfahani, M. M. Alemi, S. Alabdulkarim, and E. Rashedi, “Assessing the influence of a passive, upper extremity exoskeletal vest for tasks requiring arm elevation: Part I–“Expected” effects on discomfort, shoulder muscle activity, and work task performance,” *Appl. Ergon.,* vol. 70, pp. 315-322, 2018.
[73] T. C. Pataky, “Generalized n-dimensional biomechanical field analysis using statistical parametric mapping,” *J. Biomech.,* vol. 43, no. 10, pp. 1976-1982, 2010/07/20/, 2010.
[74] D. Chen, Y. Yun, and A. D. Deshpande, "Experimental characterization of bowden cable friction." pp. 5927-5933.
[75] A. Schiele, P. Letier, R. Van Der Linde, and F. Van Der Helm, "Bowden cable actuator for force-feedback exoskeletons." pp. 3599-3604.
[76] A. M. Halder, E. Itoi, and K.-N. An, “Anatomy and biomechanics of the shoulder,” *Orthop. Clin.,* vol. 31, no. 2, pp. 159-176, 2000.
[77] G. B. Prange, M. Jannink, A. Stienen, H. van der Kooij, M. J. IJzerman, and H. J. Hermens, “Influence of gravity compensation on muscle activation patterns

during different temporal phases of arm movements of stroke patients," *Neurorehabil. Neural Repair,* vol. 23, no. 5, pp. 478-485, 2009.

[78] G. B. Prange, L. Kallenberg, M. Jannink, A. Stienen, H. van der Kooij, M. J. IJzerman, and H. J. Hermens, "Influence of gravity compensation on muscle activity during reach and retrieval in healthy elderly," *J. Electromyogr. Kinesiol.,* vol. 19, no. 2, pp. e40-e49, 2009.

[79] H. Hsieh, D. Chen, L. Chien, and C. Lan, "Design of a Parallel Actuated Exoskeleton for Adaptive and Safe Robotic Shoulder Rehabilitation," *IEEE/ASME Transactions on Mechatronics,* vol. 22, no. 5, pp. 2034-2045, 2017.

[80] K. Kiguchi, M. H. Rahman, M. Sasaki, and K. Teramoto, "Development of a 3DOF mobile exoskeleton robot for human upper-limb motion assist," *Robotics and Autonomous Systems,* vol. 56, no. 8, pp. 678-691, 2008/08/31/, 2008.

[81] J. H. Whittle, S. E. Peters, S. Manzanero, and P. F. Duke, "A systematic review of patient-reported outcome measures used in shoulder instability research," *J Shoulder Elbow Surg,* vol. 29, no. 2, pp. 381-391, Feb, 2020.

[82] M. Asgari, E. A. Phillips, B. M. Dalton, J. L. Rudl, and D. L. Crouch, "Design and Preliminary Evaluation of a Wearable Passive Cam-Based Shoulder Exoskeleton," *Journal of Biomechanical Engineering,* vol. 144, no. 11, 2022.

[83] R. Sanchez, E. Wolbrecht, R. Smith, J. Liu, S. Rao, S. Cramer, T. Rahman, J. E. Bobrow, and D. J. Reinkensmeyer, "A pneumatic robot for re-training arm movement after stroke: Rationale and mechanical design." pp. 500-504.

[84] B. E. Perry, E. K. Evans, and D. S. Stokic, "Weight compensation characteristics of Armeo® Spring exoskeleton: implications for clinical practice and research," *J. Neuroeng. Rehabil.,* vol. 14, no. 1, pp. 1-10, 2017.

[85] A. Frisoli, L. Borelli, A. Montagner, S. Marcheschi, C. Procopio, F. Salsedo, M. Bergamasco, M. C. Carboncini, M. Tolaini, and B. Rossi, "Arm rehabilitation with a robotic exoskeleleton in Virtual Reality." pp. 631-642.

[86] F. Just, Ö. Özen, S. Tortora, R. Riener, and G. Rauter, "Feedforward model based arm weight compensation with the rehabilitation robot ARMin." pp. 72-77.

[87] D. J. Hyun, K. Bae, K. Kim, S. Nam, and D.-h. Lee, "A light-weight passive upper arm assistive exoskeleton based on multi-linkage spring-energy dissipation mechanism for overhead tasks," *Robot. Auton. Syst.,* vol. 122, pp. 103309, 2019.

[88] A. Jackson, P. Culmer, S. Makower, M. Levesley, R. Richardson, A. Cozens, M. M. Williams, and B. Bhakta, "Initial patient testing of iPAM-a robotic system for stroke rehabilitation." pp. 250-256.

[89] A. J. Westerveld, B. J. Aalderink, W. Hagedoorn, M. Buijze, A. C. Schouten, and H. van der Kooij, "A damper driven robotic end-point manipulator for functional rehabilitation exercises after stroke," *IEEE. Trans. Biomed. Eng.,* vol. 61, no. 10, pp. 2646-2654, 2014.

[90] G. Rosati, P. Gallina, A. Rossi, and S. Masiero, "Wire-based robots for upper-limb rehabilitation," *J. Robot. Mechatron. ,* vol. 7, pp. 3-10, 2006.

[91] D. Koo, P. H. Chang, M. K. Sohn, and J.-h. Shin, "Shoulder mechanism design of an exoskeleton robot for stroke patient rehabilitation." pp. 1-6.

[92] H. Soma, Y. Horiuchi, J. Gonzalez, and W. Yu, "Preliminary results of online classification of upper limb motions from around-shoulder muscle activities." pp. 1-6.

[93] T. G. Sugar, J. He, E. J. Koeneman, J. B. Koeneman, R. Herman, H. Huang, R. S. Schultz, D. Herring, J. Wanberg, and S. Balasubramanian, "Design and

control of RUPERT: a device for robotic upper extremity repetitive therapy," *IEEE Trans. Neural Syst. Rehabil. Eng.,* vol. 15, no. 3, pp. 336-346, 2007.
[94] K. Huysamen, T. Bosch, M. de Looze, K. S. Stadler, E. Graf, and L. W. O'Sullivan, "Evaluation of a passive exoskeleton for static upper limb activities," *Appl. Ergon.,* vol. 70, pp. 148-155, 2018.
[95] M. A. Nussbaum, B. D. Lowe, M. de Looze, C. Harris-Adamson, and M. Smets, "An introduction to the special issue on occupational exoskeletons," Taylor & Francis, 2019.
[96] F. Just, Ö. Özen, S. Tortora, V. Klamroth-Marganska, R. Riener, and G. Rauter, "Human arm weight compensation in rehabilitation robotics: efficacy of three distinct methods," *J. Neuroeng. Rehabil.,* vol. 17, no. 1, pp. 1-17, 2020.
[97] M. A. Sharbafi, "The Key Elements in the Design of Passive Assistive Devices." pp. 19-25.
[98] R. Altenburger, D. Scherly, and K. S. Stadler, "Design of a passive, iso-elastic upper limb exoskeleton for gravity compensation," *ROBOMECH J.,* vol. 3, no. 1, pp. 12, 2016/04/29, 2016.
[99] S. Kim, M. A. Nussbaum, M. I. Mokhlespour Esfahani, M. M. Alemi, B. Jia, and E. Rashedi, "Assessing the influence of a passive, upper extremity exoskeletal vest for tasks requiring arm elevation: Part II – "Unexpected" effects on shoulder motion, balance, and spine loading," *Appl. Ergon.,* vol. 70, pp. 323-330, 2018/07/01/, 2018.
[100] S. Kim, S. Madinei, M. M. Alemi, D. Srinivasan, and M. A. Nussbaum, "Assessing the potential for "undesired" effects of passive back-support exoskeleton use during a simulated manual assembly task: Muscle activity, posture, balance, discomfort, and usability," *Appl. Ergon.,* vol. 89, pp. 103194, 2020/11/01/, 2020.
[101] D. W. Franklin, E. Burdet, R. Osu, M. Kawato, and T. E. Milner, "Functional significance of stiffness in adaptation of multijoint arm movements to stable and unstable dynamics," *Exp. Brain Res.,* vol. 151, no. 2, pp. 145-157, 2003.
[102] D. W. Franklin, G. Liaw, T. E. Milner, R. Osu, E. Burdet, and M. Kawato, "Endpoint stiffness of the arm is directionally tuned to instability in the environment," *J. Neurosci. Res.,* vol. 27, no. 29, pp. 7705-7716, 2007.
[103] S. C. F. A. von Werder, and C. Disselhorst-Klug, "The role of biceps brachii and brachioradialis for the control of elbow flexion and extension movements," *J. Electromyogr. Kinesiol.,* vol. 28, pp. 67-75, 2016/06/01/, 2016.
[104] P. Y. Loh, K. Hayashi, N. Nasir, and S. Muraki, "Changes in muscle activity in response to assistive force during isometric elbow flexion," *J. Mot. Behav.,* vol. 52, no. 5, pp. 634-642, 2020.
[105] K. R. Holzbaur, W. M. Murray, and S. L. Delp, "A model of the upper extremity for simulating musculoskeletal surgery and analyzing neuromuscular control," *Ann. Biomed. Eng.,* vol. 33, no. 6, pp. 829-840, 2005.
[106] S. L. Delp, F. C. Anderson, A. S. Arnold, P. Loan, A. Habib, C. T. John, E. Guendelman, and D. G. Thelen, "OpenSim: open-source software to create and analyze dynamic simulations of movement," *IEEE. Trans. Biomed. Eng.,* vol. 54, no. 11, pp. 1940-1950, 2007.
[107] O. Khatib, "A unified approach for motion and force control of robot manipulators: The operational space formulation," *IEEE Robot. Autom.,* vol. 3, no. 1, pp. 43-53, 1987.
[108] V. De Sapio, and O. Khatib, "Operational space control of multibody systems with explicit holonomic constraints." pp. 2950-2956.

[109] L. Sentis, and O. Khatib, "Control of free-floating humanoid robots through task prioritization." pp. 1718-1723.
[110] L. Righetti, J. Buchli, M. Mistry, and S. Schaal, "Inverse dynamics control of floating-base robots with external constraints: A unified view." pp. 1085-1090.
[111] M. Mistry, and L. Righetti, "Operational space control of constrained and underactuated systems." pp. 225-232.
[112] A. Del Prete, F. Nori, G. Metta, and L. Natale, “Prioritized motion–force control of constrained fully-actuated robots: “Task Space Inverse Dynamics”,” *Robot. Auton. Syst.,* vol. 63, pp. 150-157, 2015/01/01/, 2015.
[113] M. Mistry, J. Buchli, and S. Schaal, "Inverse dynamics control of floating base systems using orthogonal decomposition." pp. 3406-3412.
[114] V. De Sapio, J. Warren, O. Khatib, and S. Delp, “Simulating the task-level control of human motion: a methodology and framework for implementation,” *Vis. Comput.,* vol. 21, no. 5, pp. 289-302, 2005.
[115] D. Stanev, and K. Moustakas, “Simulation of Constrained Musculoskeletal Systems in Task Space,” *IEEE. Trans. Biomed. Eng.,* vol. 65, no. 2, pp. 307-318, 2018.
[116] F. Aghili, "Inverse and direct dynamics of constrained multibody systems based on orthogonal decomposition of generalized force." pp. 4035-4041 vol.3.
[117] F. Aghili, “A unified approach for inverse and direct dynamics of constrained multibody systems based on linear projection operator: applications to control and simulation,” *IEEE Trans. Robot.,* vol. 21, no. 5, pp. 834-849, 2005.
[118] H. Sadeghian, L. Villani, M. Keshmiri, and B. Siciliano, “Task-space control of robot manipulators with null-space compliance,” *IEEE Trans. Robot.,* vol. 30, no. 2, pp. 493-506, 2013.
[119] F. De Groote, A. L. Kinney, A. V. Rao, and B. J. Fregly, “Evaluation of Direct Collocation Optimal Control Problem Formulations for Solving the Muscle Redundancy Problem,” *Ann. Biomed. Eng.,* vol. 44, no. 10, pp. 2922-2936, 2016/10/01, 2016.
[120] F. De Groote, I. Jonkers, and J. Duysens, “Task constraints and minimization of muscle effort result in a small number of muscle synergies during gait,” *Front. Comput. Neurosci.,* vol. 8, 2014-September-18, 2014.
[121] R. Postacchini, M. Paoloni, S. Carbone, M. Fini, V. Santilli, F. Postacchini, and M. Mangone, “Kinematic analysis of reaching movements of the upper limb after total or reverse shoulder arthroplasty,” *J. Biomech.,* vol. 48, no. 12, pp. 3192-3198, 2015.
[122] S. Namdari, G. Yagnik, D. D. Ebaugh, S. Nagda, M. L. Ramsey, G. R. Williams Jr, and S. Mehta, “Defining functional shoulder range of motion for activities of daily living,” *J. Shoulder Elb. Surg.,* vol. 21, no. 9, pp. 1177-1183, 2012.
[123] T. Flash, and N. Hogan, “The coordination of arm movements: an experimentally confirmed mathematical model,” *J. Neurosci. Res.,* vol. 5, no. 7, pp. 1688-1703, 1985.
[124] K. Stollenmaier, W. Ilg, and D. F. B. Haeufle, “Predicting Perturbed Human Arm Movements in a Neuro-Musculoskeletal Model to Investigate the Muscular Force Response,” *Frontiers in Bioengineering and Biotechnology,* vol. 8, no. 308, 2020-April-21, 2020.
[125] J. A. Reinbolt, A. Seth, and S. L. Delp, “Simulation of human movement: applications using OpenSim,” *Procedia Iutam,* vol. 2, pp. 186-198, 2011.

[126] A. Seth, J. L. Hicks, T. K. Uchida, A. Habib, C. L. Dembia, J. J. Dunne, C. F. Ong, M. S. DeMers, A. Rajagopal, and M. Millard, “OpenSim: Simulating musculoskeletal dynamics and neuromuscular control to study human and animal movement,” *PLoS Comput. Biol.,* vol. 14, no. 7, pp. e1006223, 2018.

[127] C. Klemt, J. A. Prinold, S. Morgans, S. H. L. Smith, D. Nolte, P. Reilly, and A. M. J. Bull, “Analysis of shoulder compressive and shear forces during functional activities of daily life,” *Clin. Biomech.,* vol. 54, pp. 34-41, 2018/05/01/, 2018.

[128] M. E. Vidt, A. C. Santago, A. P. Marsh, E. J. Hegedus, C. J. Tuohy, G. G. Poehling, M. T. Freehill, M. E. Miller, and K. R. Saul, “Modeling a rotator cuff tear: Individualized shoulder muscle forces influence glenohumeral joint contact force predictions,” *Clin. Biomech.,* vol. 60, pp. 20-29, 2018/12/01/, 2018.

[129] Runa, and R. Sharma, "A Lyapunov theory based adaptive fuzzy learning control for robotic manipulator." pp. 247-252.

[130] O. Khatib, E. Demircan, V. De Sapio, L. Sentis, T. Besier, and S. Delp, “Robotics-based synthesis of human motion,” *J. Physiol. Paris,* vol. 103, no. 3-5, pp. 211-219, 2009.

[131] V. De Sapio, “An approach for goal-oriented neuromuscular control of digital humans in physics-based simulations,” *Int. J. Model. Simul.,* vol. 4, no. 2, pp. 121-144, 2014.

[132] D. Stanev, and K. Moustakas, “Modeling musculoskeletal kinematic and dynamic redundancy using null space projection,” *PloS one,* vol. 14, no. 1, pp. e0209171, 2019.

[133] S. Madinei, S. Kim, M. M. Alemi, D. Srinivasan, and M. A. Nussbaum, "Assessment of two passive back-support exoskeletons in a simulated precision manual assembly task." pp. 1078-1079.

[134] V. Novakovic, and V. Sanguineti, “Adaptation to constant-magnitude assistive forces: kinematic and neural correlates,” *Exp. Brain Res.,* vol. 209, pp. 425-436, 2011.

[135] V. De Sapio, J. Warren, and O. Khatib, "Predicting reaching postures using a kinematically constrained shoulder model." pp. 209-218.

[136] S. H. Collins, M. B. Wiggin, and G. S. Sawicki, “Reducing the energy cost of human walking using an unpowered exoskeleton,” *Nature,* vol. 522, no. 7555, pp. 212-215, 2015.

[137] M. W. Holmes, and P. J. Keir, “Posture and hand load alter muscular response to sudden elbow perturbations,” *J. Electromyogr. Kinesiol.,* vol. 22, no. 2, pp. 191-198, 2012.

[138] T. E. Milner, “Adaptation to destabilizing dynamics by means of muscle cocontraction,” *Exp. Brain Res.,* vol. 143, pp. 406-416, 2002.

[139] Y. Ishihara, T. Mihata, M. Tamboli, L. Nguyen, K. J. Park, M. H. McGarry, S. Takai, and T. Q. Lee, “Role of the superior shoulder capsule in passive stability of the glenohumeral joint,” *J. Shoulder Elb. Surg.,* vol. 23, no. 5, pp. 642-648, 2014.

[140] N. Wuelker, M. Korell, and K. Thren, “Dynamic glenohumeral joint stability,” *J. Shoulder Elb. Surg.,* vol. 7, no. 1, pp. 43-52, 1998/01/01/, 1998.

[141] R. Lugo, P. Kung, and C. B. Ma, “Shoulder biomechanics,” *Eur. J. Radiol.,* vol. 68, no. 1, pp. 16-24, 2008.

[142] P. Goetti, P. J. Denard, P. Collin, M. Ibrahim, P. Hoffmeyer, and A. Lädermann, “Shoulder biomechanics in normal and selected pathological conditions,” *EFORT Open. Rev.,* vol. 5, no. 8, pp. 508-518, 2020.

[143] J. E. Labriola, T. Q. Lee, R. E. Debski, and P. J. McMahon, "Stability and instability of the glenohumeral joint: The role of shoulder muscles," *J. Shoulder Elb. Surg.,* vol. 14, no. 1, Supplement, pp. S32-S38, 2005/01/01/, 2005.
[144] Y. Blache, M. Begon, B. Michaud, L. Desmoulins, P. Allard, and F. Dal Maso, "Muscle function in glenohumeral joint stability during lifting task," *PLoS One,* vol. 12, no. 12, pp. e0189406, 2017.
[145] C. R. Dickerson, D. B. Chaffin, and R. E. Hughes, "A mathematical musculoskeletal shoulder model for proactive ergonomic analysis," *Comput. Methods Biomech. Biomed. Eng.,* vol. 10, no. 6, pp. 389-400, 2007.
[146] S. Lippitt, and F. Matsen, "Mechanisms of glenohumeral joint stability," *Clin. Orthop. Relat. Res.*, no. 291, pp. 20-28, 1993.
[147] R. W. Nuckols, *Effects of elastic ankle exoskeleton stiffness and walking speed on human locomotor performance from whole-body energetics to individual muscle neuromechanics*: North Carolina State University, 2017.
[148] F. A. Mussa-Ivaldi, N. Hogan, and E. Bizzi, "Neural, mechanical, and geometric factors subserving arm posture in humans," *Journal of neuroscience,* vol. 5, no. 10, pp. 2732-2743, 1985.
[149] J. M. Dolan, M. B. Friedman, and M. L. Nagurka, "Dynamic and loaded impedance components in the maintenance of human arm posture," *IEEE transactions on systems, man, and cybernetics,* vol. 23, no. 3, pp. 698-709, 1993.
[150] N. Hogan, "The mechanics of multi-joint posture and movement control," *Biological cybernetics,* vol. 52, no. 5, pp. 315-331, 1985.
[151] E. J. Hegedus, A. P. Goode, C. E. Cook, L. Michener, C. A. Myer, D. M. Myer, and A. A. Wright, "Which physical examination tests provide clinicians with the most value when examining the shoulder? Update of a systematic review with meta-analysis of individual tests," *British journal of sports medicine,* vol. 46, no. 14, pp. 964-978, 2012.
[152] D. B. Lipps, E. M. Baillargeon, D. Ludvig, and E. J. Perreault, "Quantifying the Multidimensional Impedance of the Shoulder During Volitional Contractions," *Annals of Biomedical Engineering*, pp. 1-16, 2020.
[153] T. Tsuji, P. G. Morasso, K. Goto, and K. Ito, "Human hand impedance characteristics during maintained posture," *Biological cybernetics,* vol. 72, no. 6, pp. 475-485, 1995.
[154] E. J. Perreault, R. F. Kirsch, and P. E. Crago, "Multijoint dynamics and postural stability of the human arm," *Experimental brain research,* vol. 157, no. 4, pp. 507-517, 2004.
[155] S. Stroeve, "Impedance characteristics of a neuromusculoskeletal model of the human arm I. Posture control," *Biological cybernetics,* vol. 81, no. 5, pp. 475-494, 1999.
[156] X. Hu, W. M. Murray, and E. J. Perreault, "Muscle short-range stiffness can be used to estimate the endpoint stiffness of the human arm," *Journal of neurophysiology,* vol. 105, no. 4, pp. 1633-1641, 2011.
[157] K. R. S. Holzbaur, W. M. Murray, G. E. Gold, and S. L. Delp, "Upper limb muscle volumes in adult subjects," *Journal of Biomechanics,* vol. 40, pp. 742-749, 2007.
[158] A. V. Savescu, M. L. Latash, and V. M. Zatsiorsky, "A technique to determine friction at the fingertips," *Journal of applied biomechanics,* vol. 24, no. 1, pp. 43-50, 2008.

[159] E. Burdet, K. P. Tee, I. Mareels, T. E. Milner, C.-M. Chew, D. W. Franklin, R. Osu, and M. Kawato, “Stability and motor adaptation in human arm movements,” *Biological cybernetics,* vol. 94, no. 1, pp. 20-32, 2006.

[160] H. Gomi, and M. Kawato, “Human arm stiffness and equilibrium-point trajectory during multi-joint movement,” *Biological cybernetics,* vol. 76, no. 3, pp. 163-171, 1997.

[161] L. P. Selen, D. W. Franklin, and D. M. Wolpert, “Impedance control reduces instability that arises from motor noise,” *Journal of neuroscience,* vol. 29, no. 40, pp. 12606-12616, 2009.

[162] D. W. Franklin, R. Osu, E. Burdet, M. Kawato, and T. E. Milner, “Adaptation to stable and unstable dynamics achieved by combined impedance control and inverse dynamics model,” *Journal of neurophysiology,* vol. 90, no. 5, pp. 3270-3282, 2003.

[163] K. P. Tee, E. Burdet, C.-M. Chew, and T. E. Milner, “A model of force and impedance in human arm movements,” *Biological cybernetics,* vol. 90, no. 5, pp. 368-375, 2004.

[164] D. W. Franklin, E. Burdet, K. P. Tee, R. Osu, C.-M. Chew, T. E. Milner, and M. Kawato, “CNS learns stable, accurate, and efficient movements using a simple algorithm,” *Journal of neuroscience,* vol. 28, no. 44, pp. 11165-11173, 2008.

[165] E. J. Perreault, R. F. Kirsch, and P. E. Crago, “Voluntary control of static endpoint stiffness during force regulation tasks,” *Journal of neurophysiology,* vol. 87, no. 6, pp. 2808-2816, 2002.

[166] E. J. Perreault, R. F. Kirsch, and P. E. Crago, “Effects of voluntary force generation on the elastic components of endpoint stiffness,” *Experimental brain research,* vol. 141, no. 3, pp. 312-323, 2001.

[167] H. Gomi, and R. Osu, “Task-dependent viscoelasticity of human multijoint arm and its spatial characteristics for interaction with environments,” *Journal of neuroscience,* vol. 18, no. 21, pp. 8965-8978, 1998.

[168] M. A. Krutky, R. D. Trumbower, and E. J. Perreault, “Influence of environmental stability on the regulation of end-point impedance during the maintenance of arm posture,” *Journal of neurophysiology,* vol. 109, no. 4, pp. 1045-1054, 2013.

[169] D. W. Franklin, and T. E. Milner, “Adaptive control of stiffness to stabilize hand position with large loads,” *Experimental Brain Research,* vol. 152, no. 2, pp. 211-220, 2003.

[170] X. Hu, W. M. Murray, and E. J. Perreault, “Biomechanical constraints on the feedforward regulation of endpoint stiffness,” *Journal of neurophysiology,* vol. 108, no. 8, pp. 2083-2091, 2012.

[171] A. Naceri, T. Schumacher, Q. Li, S. Calinon, and H. Ritter, “Learning Optimal Impedance Control During Complex 3D Arm Movements,” *IEEE Robotics and Automation Letters,* vol. 6, no. 2, pp. 1248-1255, 2021.

[172] K. P. Tee, D. W. Franklin, M. Kawato, T. E. Milner, and E. Burdet, “Concurrent adaptation of force and impedance in the redundant muscle system,” *Biological cybernetics,* vol. 102, no. 1, pp. 31-44, 2010.

[173] D. Stanev, and K. Moustakas, “Stiffness modulation of redundant musculoskeletal systems,” *Journal of biomechanics,* vol. 85, pp. 101-107, 2019.

[174] C. P. Cop, G. Cavallo, R. C. van’t Veld, B. F. Koopman, J. Lataire, A. C. Schouten, and M. Sartori, “Unifying system identification and biomechanical formulations for the estimation of muscle, tendon and joint stiffness during human movement,” *Progress in Biomedical Engineering,* vol. 3, no. 3, pp. 033002, 2021.

[175] B. Berret, and F. Jean, “Stochastic optimal open-loop control as a theory of force and impedance planning via muscle co-contraction,” *PLoS computational biology,* vol. 16, no. 2, pp. e1007414, 2020.

[176] D. Mitrovic, S. Klanke, R. Osu, M. Kawato, and S. Vijayakumar, “A computational model of limb impedance control based on principles of internal model uncertainty,” *PloS one,* vol. 5, no. 10, pp. e13601, 2010.

[177] A. Dietrich, C. Ott, and A. Albu-Schäffer, “An overview of null space projections for redundant, torque-controlled robots,” *The International Journal of Robotics Research,* vol. 34, no. 11, pp. 1385-1400, 2015.

[178] S. Kim, S. Yun, and D. Shin, “Numerical Quantification of Controllability in the Null Space for Redundant Manipulators,” *Applied Sciences,* vol. 11, no. 13, pp. 6190, 2021.

[179] V. De Sapio, O. Khatib, and S. Delp, “Task-level approaches for the control of constrained multibody systems,” *Multibody System Dynamics,* vol. 16, no. 1, pp. 73-102, 2006.

[180] Y. Lai, S. Sutjipto, M. G. Carmichael, and G. Paul, "Preliminary Validation of Upper Limb Musculoskeletal Model using Static Optimization." pp. 4509-4512.

[181] A. Kian, C. Pizzolato, M. Halaki, K. Ginn, D. Lloyd, D. Reed, and D. Ackland, “Static optimization underestimates antagonist muscle activity at the glenohumeral joint: A musculoskeletal modeling study,” *Journal of biomechanics,* vol. 97, pp. 109348, 2019.

[182] M. Shabani, and I. Stavness, “Simulating the effect of muscle stiffness and co-contraction on postural stability,” *Computer Methods in Biomechanics and Biomedical Engineering: Imaging & Visualization,* vol. 6, no. 5, pp. 508-519, 2018.

[183] A. Kadiallah, G. Liaw, M. Kawato, D. W. Franklin, and E. Burdet, “Impedance control is selectively tuned to multiple directions of movement,” *Journal of neurophysiology,* vol. 106, no. 5, pp. 2737-2748, 2011.

[184] F. Bailly, A. Ceglia, B. Michaud, D. M. Rouleau, and M. Begon, “Real-Time and Dynamically Consistent Estimation of Muscle Forces Using a Moving Horizon EMG-Marker Tracking Algorithm—Application to Upper Limb Biomechanics,” *Frontiers in Bioengineering and Biotechnology,* vol. 9, 2021-February-17, 2021.

[185] A. Zonnino, and F. Sergi, “Model-based analysis of the stiffness of the wrist joint in active and passive conditions,” *Journal of Biomechanical Engineering,* vol. 141, no. 4, pp. 041006, 2019.

VITA

Morteza Asgari is from Shahr-e-kord, a small city in mid-west of Iran. Born to Parvaneh and Hojjat Asgari, he holds the position of the fourth child among five siblings. From his early days of school, he showed aptitude for math and physics. Showing an aptitude for math and physics, he started a journey in mechanical engineering following his high school graduation in 2006. He completed his bachelor's degree at Iran University of Science & Technology in 2010. He, then, did his master’s in the same field at Sharif University of Technology in Tehran, Iran. It was there he first developed a passion for applying engineering principles to the field of medical technology and healthcare.

While working as a research scientist at Pars General Hospital in Tehran, he met his wife Mahshid and married her a year after. He then came over to United States in 2018 to start a PhD program in Mechanical Engineering with Dr. Dustin Crouch as his mentor. In his fourth year of the PhD program, Morteza transitioned to a full-time role as a Robotics Research Scientist at Azure Medical Innovation Corp., which he held for a year. Eventually, he returned to complete his PhD in Mechanical Engineering, and was awarded his degree in August 2023. Morteza's current aspiration involves seeking a role as a robotics software engineer within the healthcare industry, particularly in the field of medical robotics systems.